The Propagation and Amplification of Surface Waves

Thesis by

Daniel C. Bowden

In Partial Fulfillment of the Requirements for

the degree of

Doctor of Philosophy

CALIFORNIA INSTITUTE OF TECHNOLOGY

Pasadena, California

2018

(Defended April 4th, 2018)

© 2018

Daniel C. Bowden
ORCID: 0000-0003-3332-5146

ACKNOWLEDGEMENTS

I must first acknowledge and thank my advisor, Victor Tsai. His guidance, support and patience over the years have been instrumental in shaping both this work and my own development as a researcher. More than anything, he has helped me understand the scientific process and my role as a rigorous and creative researcher, and this will continue to benefit me long after the actual work in this thesis is read.

I also thank the other members of my committee, and all those I have learned from in my time at Caltech. Rob Clayton's insights and curiosity for data-driven solutions have provided a solid sounding board over the years, and I have enjoyed attending his group meetings over the years despite no obligation on his part to have me. Tom Heaton's sharp questions and challenges have shown me that I should never simply accept the status-quo. Joann Stock has already been a warm and friendly face for academic guidance and advice. Most of the work in this thesis would not have been possible without building on the foundation, advice and computational guidance of Fan-Chi Lin, both when he was here as a postdoc and in the several years since. Monica Kohler's dedication, organization and guidance on work with the ALBACORE ocean-bottom seismic array were extremely helpful. Finally, discussions over coffee with Hiroo Kanamori, Pablo Ampuero, Mark Simons, postdocs and fellow students (both older and younger) have certainly sharpened my academic perspective.

I have also benefitted from numerous people not at Caltech. My current research trajectory would not have been possible without the Long Beach dataset provided by Dan Hollis and Nodal Seismic. Through the deployment of seismometers in the Homestake Mine, I have enjoyed the collaboration with, and perspective of physicist Vuk Mandic and others in his group, and have learned a phenomenal amount about instrumentation from Gary Pavlis.

Finally, I certainly would not have completed any of this without the love and support of my wife, Scarlett Eisenhauer. Her influence on my life has been immeasurable. Her support, encouragement, resolve, levity and warmth have been an essential part of my time here.

ABSTRACT

The observation of surface waves from cross-correlations of ambient noise has proven to be an invaluable tool for the recovery of seismic travel times. Such techniques allow the construction of 3D velocity models and subsequent geologic interpretations in regions where tomography would otherwise be difficult due to the paucity of seismicity and short seismic array deployment times. One such model is developed here for offshore southern California using an array of Ocean Bottom Seismometers to better understand the tectonic history of the region.

However, for accurate hazard evaluation, characterizations of the spatial variability of ground motion amplitudes are also desired. Unfortunately, the amplitudes from noise cross-correlations are systematically biased by the spatial-, frequency- and temporal variability of noise sources. We demonstrate in this thesis that an ambient-noise based wavefront tracking technique using an array of stations can recover site-amplification and attenuation estimates successfully and robustly. This is applied on two different scales: to a very dense array of more than 5,000 geophones in the city of Long Beach, CA, and in a broader, continental scale to instruments from the USArray.

Finally, we discuss the propagation of surface waves in relation to seismic hazard and site characterization. We point out that the amplitude response and peak frequency of ground motion will be different for a given site, depending on the type of wave being considered. This work should be considered by any future seismic hazard evaluation where surface waves may cause damage.

PUBLISHED CONTENT AND CONTRIBUTIONS

Bowden, D. C., Kohler, M. D., Tsai, V. C., & Weeraratne, D. S. (2016). Offshore Southern California lithospheric velocity structure from noise cross-correlation functions. *Journal of Geophysical Research: Solid Earth*. https://doi.org/10.1002/2016JB012919

D.C.B. processed and analyzed the ambient noise data, performed the velocity inversions, produced all figures and wrote most of the manuscript.

Bowden, D. C., Tsai, V. C., & Lin, F. C. (2015). Site amplification, attenuation, and scattering from noise correlation amplitudes across a dense array in Long Beach, CA. *Geophysical Research Letters*, *42*. https://doi.org/10.1002/2014GL062662

D.C.B. performed all data analysis presented, although often using scripts and tools designed by F.C.L. Also, D.C.B. produced all figures except Fig. 3.4D-F and wrote most of the manuscript.

Bowden, D. C., Tsai, V. C., & Lin, F.-C. (2017). Amplification and Attenuation across USArray using Ambient Noise Wavefront Tracking. *Journal of Geophysical Research: Solid Earth, 122*, 1–16. https://doi.org/10.1002/2017JB014804

D.C.B. performed all data analysis presented, although often using scripts and tools designed by F.C.L. Also, D.C.B. produced all figures except Fig. 4.8B and 4.8E, and wrote most of the manuscript.

Bowden, D. C., & Tsai, V. C. (2017). Earthquake ground motion amplification for surface waves. *Geophys. Res. Lett.*, *43*, 1–8. https://doi.org/10.1002/2016GL071885

D.C.B. participated in the conception of the project, performed all data analyses, produced all figures and wrote most of the manuscript.

TABLE OF CONTENTS

LIST OF FIGURES

Chapter 1

INTRODUCTION

This thesis considers the observation of surface waves in the Earth's crust. Chapters 2, 3 and 4 deal with observational techniques exploiting the ambient noise field at various scales and periods, while Chapter 5 considers the implications of surface wave propagation for seismic hazard. Content from each of these chapters has been previously published as individual papers, and the full reference for each is listed in the appropriate chapter.

1.1 On Surface Wave Observations in Ambient Noise

In recent years, the Earth's ambient noise field has been increasingly exploited to infer useful properties of the Earth's crust and mantle [e.g., *Shapiro*, 2004]. Continuous seismic signals propagating between and around any two seismic stations, data which was once considered useless background noise, can be cross-correlated to isolate vibrations common to both stations (see Figure 1.1). Developed cross-correlation techniques have predominantly focused on the recovery of robust seismic travel times [e.g., *Bensen et al.*, 2007], which can be used to infer and understand geologic structure. Chapter 2 of this thesis is an example of this, where ambient noise cross-correlations are used to construct a 3D velocity model of the Continental Borderland offshore southern California. Chapter 2 shows how ambient noise is now standardly being used to supplement traditional earthquake source tomography, though some additional signal processing steps were necessitated by the use of ocean-bottom instruments. The resulting velocity model sheds light on the tectonic history of this region and allows us to compare different descriptions of how continental lithosphere was thinned during the transition from subduction tectonics to modern-day extension.

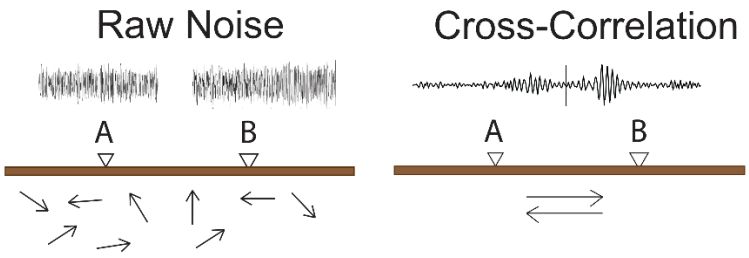

Figure 1.1: The effect of measuring the cross-correlation or coherence between two noise traces is to extract signals common to both. This is usually interpreted as signals traveling directly between the two stations, and is usually dominated by surface waves.

Aside from standard travel-time tomography, there are numerous opportunities to be exploited through the observations of a seismic wave's amplitude. Accurate amplitude observations are needed to measure crustal properties such as attenuation and scattering, and also provide independent constraints on 3D crustal structure to further supplement traditional tomography. There are also civil-engineering applications that can benefit from direct observation of site-amplification and attenuation, without the need to rely on complex inversions for 3D structure.

Unfortunately, directly measuring amplitudes from ambient noise is problematic. It has been shown theoretically [e.g., *Tsai*, 2011], empirically [e.g., *Ermert, Villaseñor, & Fichtner,* 2016] and numerically [e.g., *Cupillard & Capdeville,* 2010] that the observed amplitude of a given phase in a noise correlation function (NCF) depends on the exact distribution of noise sources, which are themselves usually unknown and quite variable. If the noise sources were evenly and consistently distributed across time, space, frequency and mode of propagation then the resulting impulse response or Green's Function would be directly interpretable (see Fig 1.2A). Given that that noise sources in the real Earth are almost always biased in some way, the resulting NCF may appear stronger in one direction and the amplitude directly observed is harder to interpret (Fig. 1.2B) [*Weaver,* 2011].

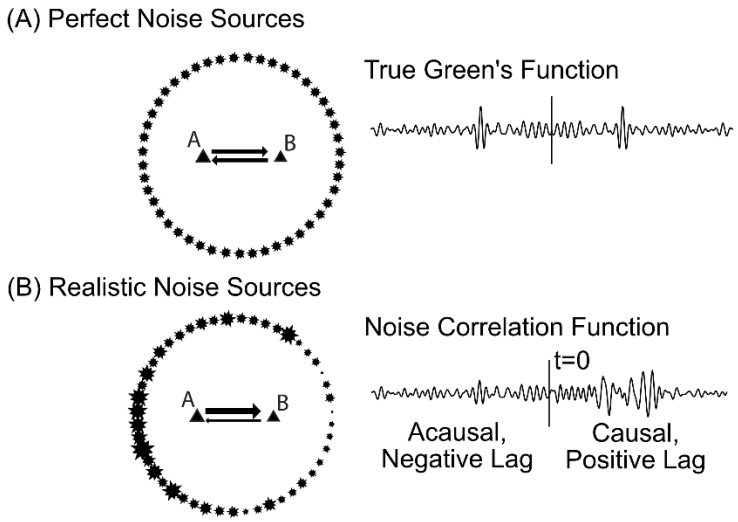

Figure 1.2: An even distribution of noise sources will result in a true Green's function after signals are cross-correlated (A), but any uneven and realistic distribution will bias the amplitudes of the resulting Noise Correlation Function (B). The noise sources in both cases are shown as a ring of stars, though this is only a schematic to illustrate noise sources throughout the region in any direction and at all possible distances.

Given this constraint, Chapters 3 and 4 discuss the application of a wavefront tracking technique across an array of stations. The method collects all available NCFs using one station as a virtual source, from which it can be shown that the recovered wavefield itself satisfies the wave equation. While any one NCF cannot be trusted to reliably give information regarding the strength of ground motions, the observation of a wavefront and its subsequent growth or decay can be used to directly infer the amplitude properties we are interested in. The application of a wavefront tracking method for surface wave amplitudes was first described by *Lin et al.* [2012], but it had remained to be shown that the approach could be extended to use the ambient noise field. The method is described in Chapters 3 and 4, the equations used are fully derived in Supplementary Materials section S3 and additional notes regarding differences between causal and acausal noise signals in included in Supplementary Materials section S4.

Specifically, Chapter 3 applies the wavefront tracking technique to a dense array of more than 5,000 geophones in Long Beach, CA, recovering observations of site amplification, attenuation and scattering at periods 0.5 to 1 second. Chapter 4 applies the same approach to stations on a continental scale using the USArray for periods from 8 to 32 seconds. This provides new constraints for lithospheric properties independent of seismic travel times, and it also demonstrates the method's validity, since numerous other works have studied the crust on this scale. We can therefore compare the results of several different approaches.

1.2 On the Site Amplification of Surface Waves

Observations of a surface wave's amplitude as it propagates through the Earth's crust have additional implications for seismic hazard and earthquake engineering. As described in Chapter 5, if surface waves are present in the strong ground motion during an earthquake, a different prediction of site response in regards to both shaking strength and peak frequency should be considered. This is in contrast to the standard definition underlying almost all other studies.

This standard model of site response assumes a vertically-travelling shear wave, amplified and resonating in shallow sedimentary layers [e.g., *Borcherdt and Gibbs,* 1976]. For many possible future earthquakes, and particularly for higher-frequency ground motions, this model is a perfectly suitable approximation. However, for a region like southern California, should long-period surface waves propagate into the deep Los Angeles sedimentary basin from a rupture on the San Andreas fault, the appropriate definition of conservation of energy [i.e., *Tromp and Dahlen,* 1992] suggests a very different site amplification effect. Chapter 5 discusses how a relatively simple transfer function for surface waves can be used to supplement the traditional definition of site amplification, as well as the implications for previous studies and statistical regressions. The approach is specifically devised to fit the pre-existing 1D models and workflow used for seismic hazard, and can therefore be incorporated to enhance public safety.

1.3 References

Bensen, G. D., M. H. Ritzwoller, M. P. Barmin, a. L. Levshin, F. Lin, M. P. Moschetti, N. M. Shapiro, and Y. Yang (2007), Processing seismic ambient noise data to obtain reliable broad-band surface wave dispersion measurements, *Geophys. J. Int., 169(3),* 1239–1260, doi:10.1111/j.1365-246X.2007.03374.x.

Borcherdt, R. D., and J. F. Gibbs (1976), Effects of local geological conditions in the San Francisco bay region on ground motions and the intensities of the 1906 earthquake, *Bull. Seism. Soc. Am., 66(2),* 467–500.

Cupillard, P., and Y. Capdeville (2010), On the amplitude of surface waves obtained by noise correlation and the capability to recover the attenuation: A numerical approach, *Geophys. J. Int., 181(3),* 1687–1700, doi:10.1111/j.1365-246X.2010.04586.x.

Ermert, L., A. Villaseñor, and A. Fichtner (2016), Cross-correlation imaging of ambient noise sources, *Geophys. J. Int., 204(1),* 347–364, doi:10.1093/gji/ggv460.

Lin, F.-C., V. C. Tsai, and M. H. Ritzwoller (2012), The local amplification of surface waves: A new observable to constrain elastic velocities, density, and anelastic attenuation, *J. Geophys. Res., 117(B6),* B06302, doi:10.1029/2012JB009208.

Shapiro, N. M. (2004), Emergence of broadband Rayleigh waves from correlations of the ambient seismic noise, *Geophys. Res. Lett., 31(7),* L07614, doi:10.1029/2004GL019491.

Tromp, J., and F. a. Dahlen (1992), Variational principles for surface wave propagation on a laterally heterogeneous Earth -- I. Time-domain JWKB theory, *Geophys. J. Int., 109(3),* 581–598, doi:10.1111/j.1365-246X.1992.tb00119.x.

Tsai, V. C. (2011), Understanding the amplitudes of noise correlation measurements, *J. Geophys. Res., 116(B9),* B09311, doi:10.1029/2011JB008483.

Weaver, R. L. (2011). On the amplitudes of correlations and the inference of attenuations, specific intensities and site factors from ambient noise. *Comptes Rendus - Geoscience*, *343*(8–9), 615–622. https://doi.org/10.1016/j.crte.2011.07.001

Chapter 2

OFFSHORE SOUTHERN CALIFORNIA LITHOSPHERIC VELOCITY STRUCTURE FROM NOISE CROSS CORRELATION FUNCTIONS

Bowden, D. C., Kohler, M. D., Tsai, V. C., & Weeraratne, D. S. (2016). Offshore Southern California lithospheric velocity structure from noise cross-correlation functions. *Journal of Geophysical Research: Solid Earth. https://doi.org/10.1002/*2016JB012919

2.1 Abstract

A new shear-wave velocity model offshore southern California is presented that images plate boundary deformation including both thickening and thinning of the crustal and mantle lithosphere at the westernmost edge of the North American continent. The ALBACORE ocean bottom seismometer array, together with 65 stations of the onshore Southern California Seismic Network, are used to measure ambient noise correlation functions and Rayleigh-wave dispersion curves which are inverted for 3D shear-wave velocities. The resulting velocity model defines the transition from continental lithosphere to oceanic, illuminating the complex history and deformation in the region. A transition to the present-day strike-slip regime between the Pacific and North American Plates resulted in broad deformation and capture of the now >200-km-wide continental shelf. Our velocity model suggests the persistence of uppermost mantle volcanic processes associated with East Pacific Rise spreading adjacent to the Patton Escarpment, which marks the former subduction of Farallon Plate underneath North America. The most prominent of these seismic structures is a low-velocity anomaly underlying San Juan Seamount, suggesting ponding of magma at the base of the crust, resulting in thickening and ongoing adjustment of the lithosphere due to the localized loading. The velocity model also provides a robust framework for future earthquake location determinations and ground shaking simulations for risk estimates.

2.2 Introduction

The tectonically active region of southern California and the Pacific-North American Plate boundary extends far west of the coastline, but seismic velocity models of the lithosphere and upper mantle in this offshore region are not well developed (from the Continental Borderland to west of the Patton Escarpment, Fig. 2.1), especially at subcrustal depths. This 200 km-wide offshore region represents the transition from continental lithosphere to oceanic, but is much wider than typical continental shelves and has experienced a significant amount of previous and ongoing deformation as a result of its complex history. Ancient subduction of the Farallon Plate under the North American Plate, and the subsequent transition to the current transpressional environment between the Pacific and North American plates, has left a wide region with a history of rotation, extension, strike-slip motion, and compression [*Crowell,* 1968; *Atwater,* 1970; *Atwater,* 1989; *Dokka,* 1989; *Stock and Hodges,* 1989; *Tennyson,* 1989; *Luyendyk,* 1991; *Wright,* 1991; *Crouch and Suppe,* 1993; *Feigl et al.* 1993; *Shen et al.* 1996; *Walls et al.* 1998].

An array of 34 ocean bottom seismometers (OBSs) was deployed in 2010 to better understand the Pacific-North American Plate boundary deformational history and to image the region's deeper lithospheric structure. This array was part of the ALBACORE (Asthenospheric and Lithospheric Broadband Architecture from the California Offshore Region Experiment) project [*Kohler et al.*, 2010, 2011]. The OBSs were purposely deployed far west of the coastline and the Patton Escarpment to fully capture the seismic structure transition between continental and oceanic tectonic environments. Local seismicity, as well as multibeam bathymetry data collected during the cruise, were used by *Legg et al.* [2015] to image transpressional fault zones in the Borderland to better constrain seismic risk from offshore faults.

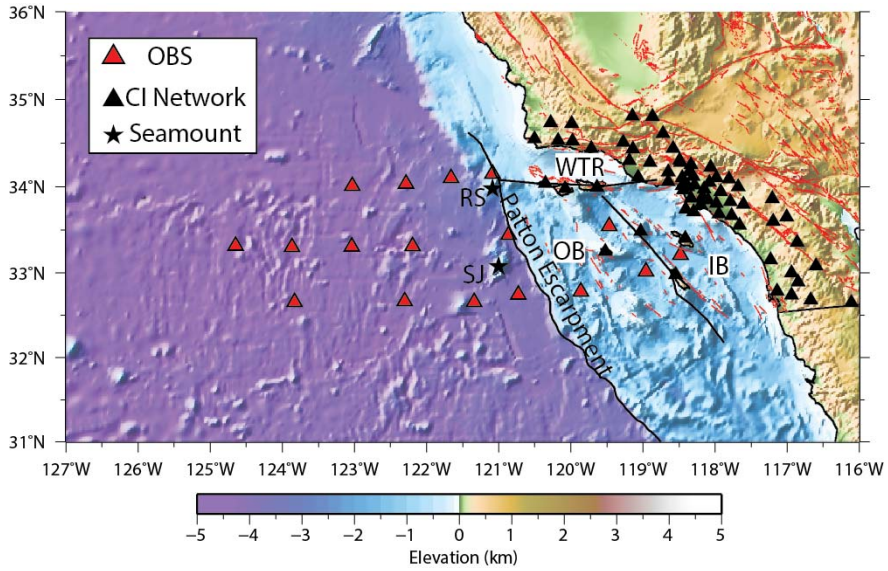

Figure 2.1: Map of the southern California offshore region. Triangles indicate broadband seismometers used in the study. The original ALBACORE dataset included more stations than indicated (and was roughly on a regular grid), but some stations were not recovered or had technical problems. Tectonic domains indicated include: OB: Outer Borderland, IB: Inner Borderland, WTR: Western Transverse Ranges. Seamounts indicated include: RS: Rodriguez Seamount; SJ: San Juan Seamount. Black lines separating these regions are inferred from geological structures (*Legg et al.* [2015]).

In addition to understanding the tectonic history of the offshore region, there is also a need for accurate seismic velocity models due to its proximity to the San Andreas Fault system. *Legg et al.* [2015] and others observe a number of seismogenic fault zones in the area, as slip on the Pacific-North American Plate boundary is broadly distributed across southern California. The Southern California Earthquake Center (SCEC) has compiled Community Velocity Models (CVMs) (e.g., [*Shaw et al.*, 2015]), with the purpose of providing a reliable base for ground motion simulations, earthquake location studies and deeper tomography. The models are well developed on land and in the populated regions of Los Angeles, but they either end abruptly just off the coastline or they consist of an overly smooth 1D velocity profile in the offshore region.

This study uses ambient noise tomography to develop a full 3D velocity model of the region. Based on the array aperture and station spacing, we image the crust and uppermost mantle, from the oceanic lithosphere far west of the Patton Escarpment through the Inner and Outer Borderland and through continental southern California. A number of studies have demonstrated the efficacy of ambient noise studies to recover velocity models in ocean environments, including *Lin et al.* [2006] across the Pacific Ocean, *Harmon et al.* [2007] and *Yao et al.* [2011] on different arrays near the East Pacific Rise, and *Gao et al.* [2015] over the Cascadia Subduction Zone. In nearly all cases, such studies have filled a much needed gap between the near-surface resolution provided by active-source seismic reflection surveys and deeper earthquake based body-wave and surface-wave tomography. Ocean environments tend to be noisy due to interactions between the solid earth and the water column, but ambient noise signals are recoverable at shorter periods (i.e., 5-10 s) compared to earthquake surface waves.

2.3 Tectonic Background

The history and near-surface geology of the California Borderland region has been well documented. *Atwater and Stock* [1998], for example, provide plate motion reconstructions based on paleomagnetic data, fault structures and drill core dates, and describe how the Western Transverse Ranges block in the northern part of the region was captured by the Pacific Plate and rotated clockwise more than 90 degrees to its current location. This rotation and subsequent strike-slip tectonics of the remaining Borderland has left a series of NW-striking faults and basins [*Legg,* 1991, *Crouch and Suppe,* 1993], with significant lithospheric thinning under the inner (eastern) part, and westward translation of the outer region [*Nicholson et al.,* 1994]. The boundary between the Inner and Outer Borderland is marked by the East Santa Cruz Basin Fault, and represents a geologic shift from exhumed Catalina Schist Belt to sediments of the Patton Accretionary Complex [*Vedder et al.,* 1974].

Gravity and seismic profiles provide constraints on upper crustal and sedimentary structure, such as those collected during the Los Angeles Region Seismic Experiment (LARSE) in

1994 [*Fuis et al.,* 2003; 2012], and several lines collected by the USGS in 1978, 1979 and 1990. Inversions of gravity profiles [*Miller,* 2002; *Romanyuk et al.,* 2007] suggest thinning in the region during periods of extension, and subsequent infiltration of mafic melt in the crust. Similarly, *Weigand* [1994] and *ten Brink* [2000] use petrological and seismic reflection data to propose that very little mantle lithosphere exists below the Inner Borderland.

Despite the extension and thinning however, it is not until west of the Patton Escarpment, which is at least 200 km west of the coastline, that the geology, bathymetry and gravity are indicative of normal oceanic lithosphere. The Patton Escarpment is delineated by a cessation of magnetic anomalies typical of oceanic environments [*Atwater,* 1989], as well as an abrupt change of bathymetry from ~4 km to the west to ~2 km to the east. However, the subsurface structure of the transition is not well imaged, even though it represents the now-extinct subduction zone where the Farallon Plate subducted under the North American Plate [*Atwater,* 1989; *Lonsdale,* 1991].

Teleseismic earthquakes have been investigated by *Reeves et al.* [2015], from both the ALBACORE array and the permanent Southern California Seismic Network (SCSN), to measure receiver functions in order to image velocity transitions in the region. Their observations provide some of the first direct constraints on depths of the Moho and lithosphere-asthenosphere boundary below the Borderland, as well as general lithospheric structure west of the Patton Escarpment. In agreement with previous studies, they find substantial thinning in the Inner Borderland consistent with extension to accommodate rotation of the Western Transverse Ranges, and that the effect of this thinning on deeper lithospheric structure may be even more severe than previously speculated.

2.4 Data and Methods

Approximately one year of continuous data are used to measure ambient noise cross correlations, using data from 17 broadband ALBACORE OBS stations and 65 on-land SCSN

stations (Fig. 2.1). Several of the deployed OBS stations were either not recovered or contained incomplete data. Of the 34 OBSs deployed, 24 of those were broadband and 17 of those were recovered with useful data [*Kohler et al.,* 2011]. All OBS stations used provided three components of seismic data, as well as a differential water pressure gauge (DPG) channel. In this study, only vertical component data are used for the Rayleigh wave observations. The DPG and horizontal components are used only to improve the vertical-component signals, as described below. This section describes our signal preprocessing and dispersion curve measurement approach, the linear inversion for slowness at each period, and finally 1D depth inversions beneath each grid point to construct the full 3D tomographic model.

2.4.1 Signal Preprocessing and Cross Correlation

Underwater environments are generally very noisy due to the action of interfering swells at the surface and ocean currents at depth [*Webb,* 1998], and such data usually warrant additional preprocessing for ambient noise studies. While the actions of water waves and subsequent pressure perturbations on the seafloor are understood to be the dominant source of ambient noise energy in the primary microseism band [*Longuet-Higgins,* 1950; *Gimbert and Tsai,* 2015]**,** these sources are relatively well distributed in space and time across the Earth's oceans. The effect of these forces acting directly on a single OBS, however, creates an incoherent (inelastic) signal detrimental to recovering noise correlations. Fortunately, these forces from the water column are also measured by the co-located ALBACORE DPGs (pressure gauge), so a transfer function between the two components can be used to remove the unwanted signals [*Webb and Crawford,* 1999]. Similarly, ocean currents moving past the OBS tilt the seismometer, causing low-frequency noise on the vertical channels that is incoherent with other seismometers in the array. Determining a transfer function with the horizontal components can similarly be used to remove undesired tilt signals [*Crawford and Webb,* 2000].

We follow the procedure of *Webb and Crawford* [1999] and *Crawford and Webb* [2000] to perform tilt corrections and DPG corrections, and note that a more thorough study of such techniques is described by *Bell et al.* [2015]. These types of corrections are traditionally applied to longer-period signals (i.e., greater than 50 s) than those of this study, but we find that they improve some of our measurements nonetheless. For a given non-vertical component (either horizontal or the DPG), a transfer function to the vertical component is determined from a 12-hour period of time known to be quiet and free of earthquakes. This transfer function describes the frequencies and associated phases at which signals are coherent, and can be used to predict the effect that a given pressure signal or tilt event will contribute to the vertical-component OBS channel (Fig. 2.2). The coherencies vary strongly with location and water depth, so we taper the transfer function to zero outside the period range of 5 to 15 s where the signals are most coherent. We apply all corrections in sequential steps. We first determine and apply a transfer function from one horizontal component to all other components before proceeding. Next, transfer functions from the second horizontal component are applied to both the pressure gauge and vertical component, and finally we apply the transfer function from the pressure gauge to the vertical. This sequential processing (i.e., also correcting one horizontal based on the other) ensures that any effect of the water column which affects both components coherently will not be mistakenly corrected twice. We also note that the transfer function is independent of units, so we do not apply the vertical instrument response until after the entire process is complete.

The effects of the wave loading and tilt corrections are often dramatic and potentially useful for event detection (Fig. 2.2). In contrast, we find that for the 5-9 s period range of noise cross correlations, the application of the corrections reduces the strength of the fundamental surface mode observation relative to the first overtone. Indeed, this is likely why the original work of Webb and Crawford only uses the technique at longer periods. It is likely that at the shorter periods our fundamental mode measurements are so sensitive to the water layer that removing signals coherent with the DPG and tilt also removes much of the useful signal. The first overtone, however, is sensitive to deeper structure and is relatively easier to measure

with the correction. Thus, we consider both the uncorrected and corrected sets of noise correlations when measuring dispersion curves (Figs. 2.3 and 2.4), using whichever set shows a stronger signal at a given period.

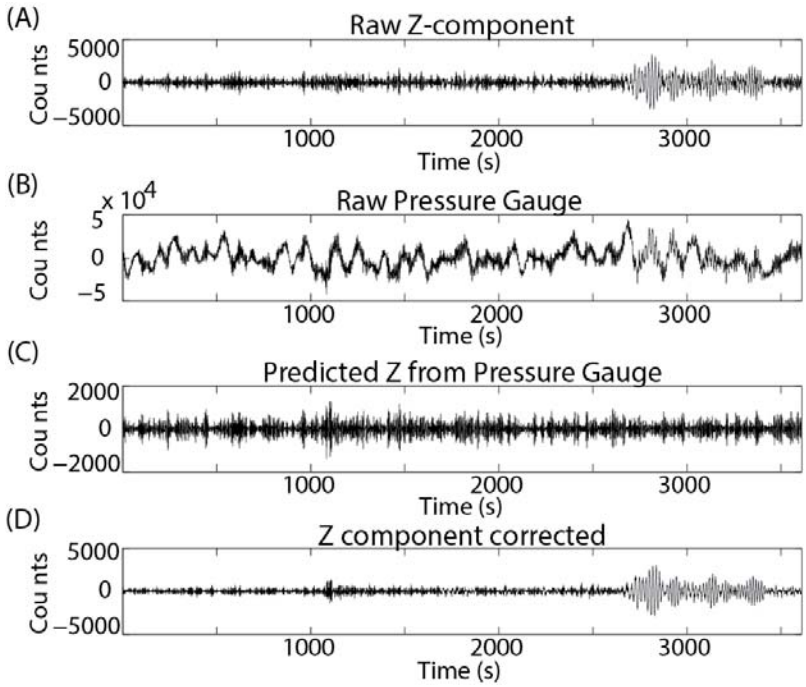

Figure 2.2: Steps for processing tilt and DPG corrections. An hour of uncorrected vertical-component data is presented in (A). The pressure gauge component (B) is used to predict an effect on the vertical component (C) which is subtracted from the raw vertical (A) to produce a cleaned time series (D).

Before performing the ambient noise cross correlations, we also apply standard time-domain normalization and spectral whitening as described by *Bensen et al.* [2007]. These techniques help suppress the effects of earthquakes and other non-stationary sources of energy which may bias the noise correlation function (NCF). We take the symmetric component of the NCF by summing the data from positive and negative correlation time lags. We stack the entire year of data to help ensure that we have averaged out any azimuthal bias by seasonal weather patterns, even though we find that the NCFs are generally stable with 3-5 months of stacking.

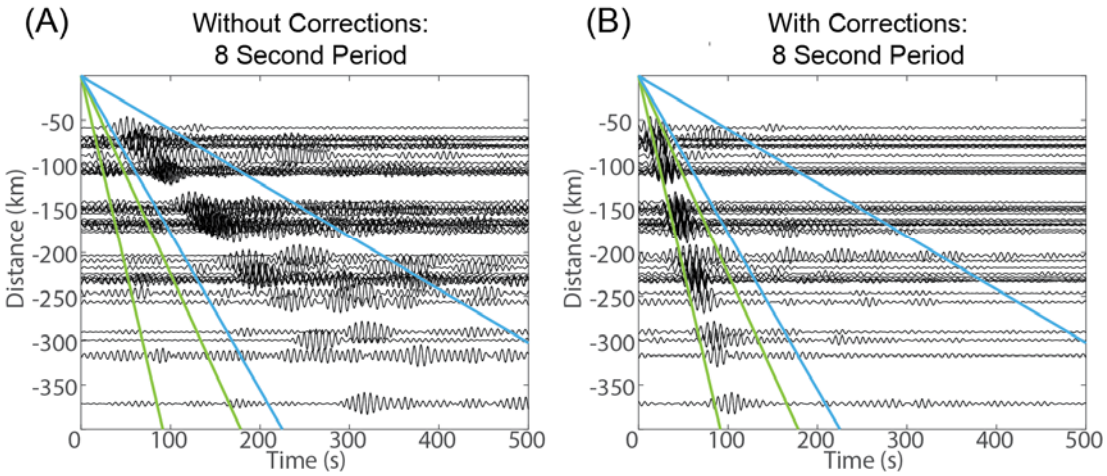

Figure 2.3: Record section of station pairs in the deep ocean. (A) uses raw data, (B) uses data corrected for tilt and pressure loading. We observe a significant difference in our ability to observe the fundamental mode and first overtone, with expected ranges of velocities for both modes windowed in blue and green, respectively.

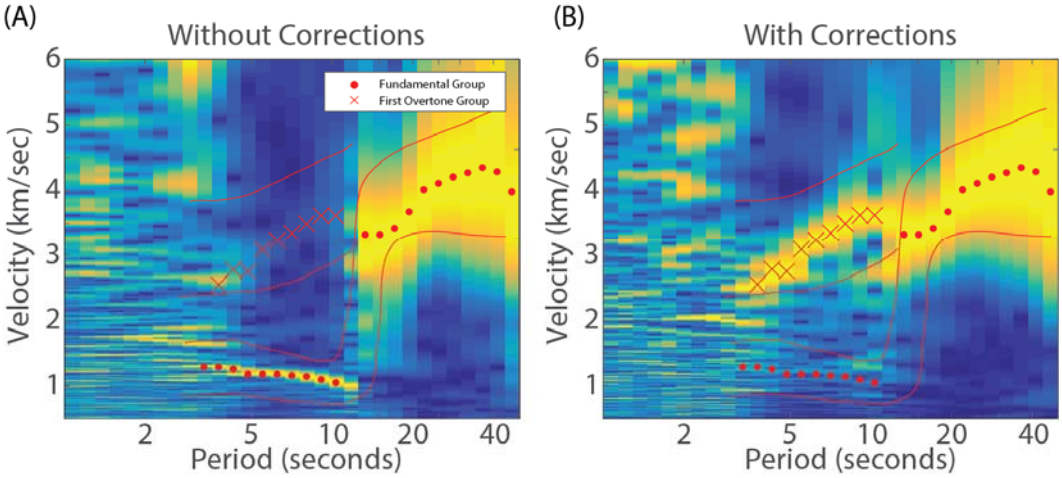

Figure 2.4: An example of extracting dispersion data from a single NCF. Each column represents a narrow bandpass filter, where the color represents a normalized amplitude of the signal envelope. Red lines bound the expected range of measurements for the oceanic region, for both the fundamental mode (lower set of curves) and first overtone (higher set). Red dots and X's indicate selected group velocity measurements, again from both corrected and uncorrected data.

Measuring dispersion from the NCFs proved challenging, however, as the extremely varied tectonic nature of the region and varying water depths meant that often the arrival of a given mode could not be cleanly identified with a purely automated script. Velocity changes created spurious reflections and scatterers in the NCFs, especially in the coastline transition. Approximately half the dispersion curves were manually picked prior to application of an automated frequency-time analysis procedure, based on the FTAN script of *Levshin and Ritzwoller* [2001]. While the original script allowed for setting a single maximum and minimum velocity, our modification considers a predetermined reference dispersion curve (determined from manual observation of a subset of the NCFs) and searches for the maximum within given bounds, effectively guiding the automated search more precisely as a function of period (red lines in Fig 2.4). Four additional quality control checks are employed: a signal-to-noise ratio (SNR) test, removal of data more than two standard deviations from the average at each period, removal of rays with distances less than 2 times the expected wavelength and lastly a manual examination of all dispersion curves with manual removal of any curves which appear biased by some other reflection or complication. The signal-to-noise ratio is defined as the peak group amplitude divided by the root-mean-square of signals outside the expected arrival window, where measurements with SNR < 3 were rejected (and the SNR was later used again to weight raypaths in the inversion). Table 1 describes the number of raypaths retained out of the possible 3,321 station pairs, and examples of their spatial distributions are shown later when the inversion process is described.

Period (s)	5	7.5	10	15	20	30	40	50
# of Raypaths (Fundamental Mode)	934	1257	1357	1263	1114	996	839	49
# of Raypaths (First Overtone)	43	53	8	-	-	-	-	-

Table 2.1: Number of raypaths retained out of possible station pairs.

Figs. 2.5a-c show samples of resulting dispersion measurements, grouped by pairs within distinct geologic regions. The station pairs in deeper water (Fig. 2.5a) are in approximately constant 4-km water depth, and are located on the relatively homogeneous abyssal plain; thus they are clean enough to distinguish the first overtone. This is particularly useful since the fundamental mode in the period range 5-10 s is dominated by the water layer (with phase velocities close to 1 km/s), while the higher modes have sensitivity primarily to crustal structure. Also, there is a gap in measurements around 10 s (Fig. 2.5a), which represents a transition from sensitivity predominantly to the water layer, to sensitivity to the uppermost crust. Our bandpass filters are Gaussian functions with finite width; thus, at a period of around 10 s, signals are dominated by both sensitivities' velocity and period. Figs. 2.5b and 5c represent raypaths in the Borderland and on-land, and show significantly more scatter due to tectonic heterogeneity.

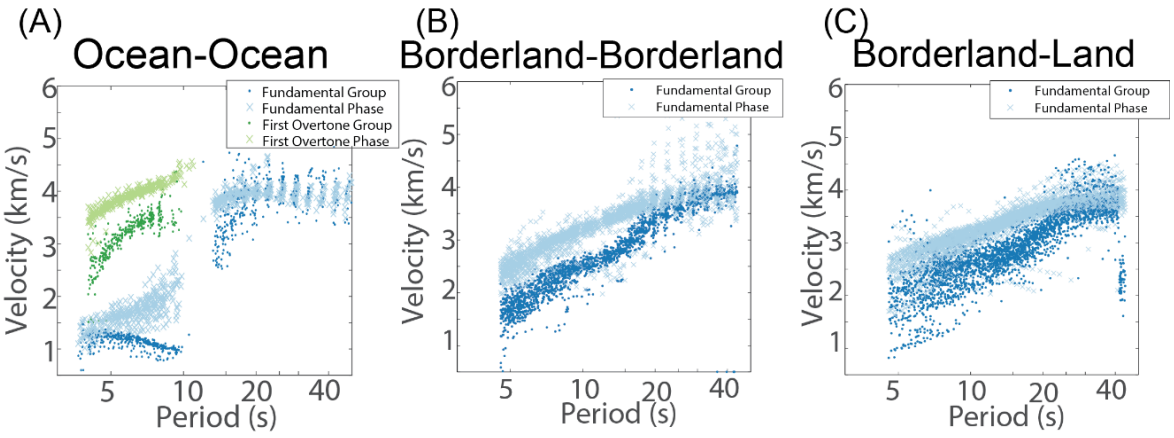

Figure 2.5: Sample dispersion curves grouped by dominant structural features. Raypaths not included in these figures span multiple geologic domains, such as from the deep ocean to inland, and such raypaths show more variability than those presented here.

2.4.2 Inversion for 2D Maps at each Period

The first step towards constructing a 3D shear-wave velocity model consisted of inverting the raypaths at 20 different periods for a 2D grid of phase and group velocity measurements, following the least-squares approach of *Barmin et al.* [2001] and *Ma et al.* [2014]. Group

and phase measurements are determined at each period for both fundamental and first overtone data (e.g., Fig. 2.5). Velocities are described by a deviation in slowness from the average, providing a linearized inverse problem:

$$\Delta t_i = \int \frac{m_i}{c_o} ds, \leftrightarrow d = Gm \qquad \text{Eq. 2.1}$$

where $m_i = (c_0 - c)/\, c$, phase velocity is c, and a baseline average phase velocity is c_0.

$$m = (G'WG + \beta\, L1'L1 + \alpha F'F)^{-1} GWd \qquad \text{Eq. 2.2}$$

F describes a small amount of Gaussian smoothing applied to each ray such that it sufficiently approximates the true finite-frequency kernel given the relatively course grid-spacing [*Barmin et al.,* 2001]. L1 describes a Tikhonov regularization [*Loris et al.,* 2007], which reduces the first derivative across the inverted grid and stabilizes grid points that are outside our region of densest rays. W is a diagonal matrix of SNR used to weight better station pairs; specifically, the diagonal elements are the normalized log of 1/SNR to prevent overweighting. The amount of regularization is manually tuned to provide images which are smooth on the length scale of our station spacing, but with as little smoothing as possible so that the dynamic range of velocities is optimally maximized. While the conversion to slowness and the formulation of the inverse problem are linear, regularization and smoothing do not have a linear effect on the recovered velocities; however, checkerboard tests indicate this effect is minimal for our range of velocities. Fig. 2.6 shows an example of input rays and resulting 2D model at a 5 second period, and additional periods (12 s, 20 s and 40 s) can be found in Supplementary Figures S1.1-S1.3.

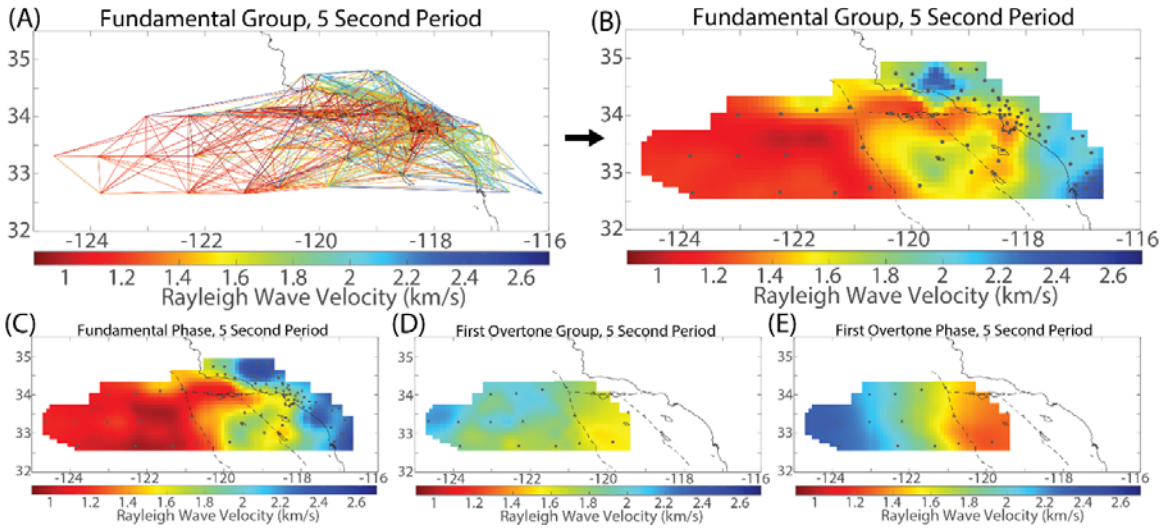

Figure 2.6: Examples of 2D grid inversions for a given period. Input rays shown in (A) are inverted on a regular grid, (B). The same procedure is applied to raypath measurements of fundamental phase (C), first overtone group (D), and first overtone phase (E). The grid used for first overtone measurements is smaller to respect the region for which measurements were made. The same procedure is applied for 20 logarithmically spaced periods from 5 – 50 s.

Fig. 2.7 shows a checkerboard test with the resulting inversion results using the raypath dataset corresponding to 8.5 s period. Fig. 2.7B shows that we successfully recover the majority of features on the length scale of our station spacing. Additional checkerboard tests are presented in Supplementary Figures S1.1-S1.3. An additional recovery test designed with a single strong boundary along the Patton Escarpment is shown in the Supplementary Material text S1. The results from this second test (Fig. S1.4B) indicate that we can resolve features along the Patton Escarpment, specifically, to a lateral length scale of 50 km. Our results are limited to the resolution of our grid spacing, but we find that the presence of a strong boundary does not bias or degrade the slowness inversion accuracy or resolution.

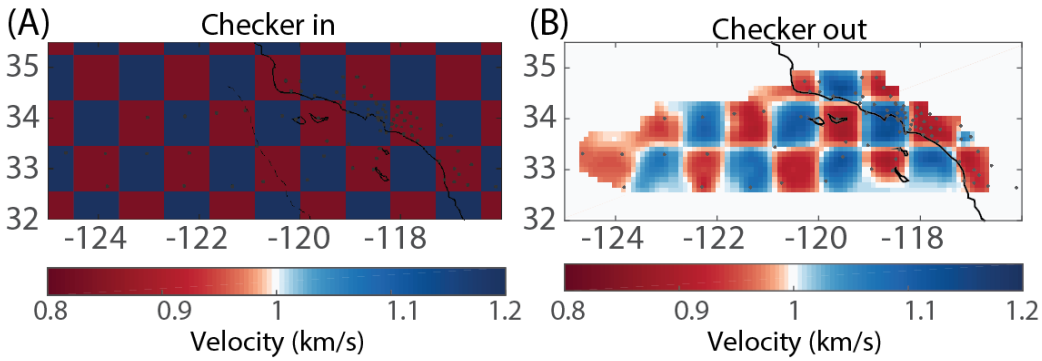

Figure 2.7: Checkerboard test using raypaths available for fundamental group measurements corresponding to 8.5 s period. We trim all later maps to the region well covered by raypath density, and well recovered in such checkerboard tests.

2.4.3 Inversion for Shear Wave Velocity with Depth

With velocities represented on a set of 2D grids, the next step towards constructing the shear-wave velocity model is to invert the dispersion curves at each grid point for 1D structure. We use a modal summation technique to compute synthetic dispersion curves and compare to data (using the software package Computer Programs in Seismology [*Herrmann,* 2013]). The inversion is allowed to iterate for each grid point, improving each 1D profile to minimize the misfit between the dispersion curve data and the synthetic dispersion curves, until the profiles converge. The 1D shear velocity profiles are defined at 1-km intervals, though a lack of resolution and uniqueness at depth limits the scale of features we can interpret to 5-10 km, described later. We uniquely solve only for shear wave velocities; any relation to compressional wave velocities or density used in the CPS package relies on standard empirical relationships (i.e., Vp/Vs ratio can be approximated as 1.7). To minimize the bias from a chosen starting model, we use a range of 41 input starting models. All of these are linear ramps of increasing velocity or otherwise constant in velocity and linearly stepping between end-member expectations of velocities between 2 km/s and 5 km/s, and whose only constraint is a water layer of fixed thickness appropriate for each grid point. We choose to use only simple starting models, as the deeper geologic structure of the region is still relatively unknown and we did not want to incorrectly bias the final model. We average the results from these starting models, though we find that the resulting velocity model is fairly

independent of starting model (starting models and example 1D profiles are shown in Supplement Figure S1.5). This final model predicts dispersion data with an average misfit of 0.18 km/s, which is approximately twice as accurate as would be predicted by the synthetic, simple model produced from standard reference profiles described in Supplementary Text S1.

Fig. 2.8 shows the sensitivity kernels for an average, smooth 1D profile underneath a 4-km-thick water layer, and shows that the first overtone is considerably more sensitive to shallow crustal structure in this environment. The kernels are calculated by perturbing each layer sequentially by a 1% increase in shear-wave speed. The water layer has a shear-wave speed of zero, so the kernels' low sensitivity in the water layer is a result of no perturbation in that layer; the extremely low fundamental group and phase measurements in the short-period range are further evidence of the water sensitivity on the kernel (pure water should have a phase velocity of around 1.4 km/s). The stronger sensitivity of the first overtone highlights the importance of including it (where available) in an oceanic environment.

As with any inversion of this type, we resolve shallow features better than deeper features. The sensitivity kernels (Fig. 2.8) and final iteration resolution matrices indicate a vertical resolution of 5 km in shallow regions (1-30 km depth), with vertical resolution degrading to ~10 km by 50 km depth. Some of the cross sections presented later include model features down to 70 km depth, though we limit our interpretations of such deeper structures. Using a range of input starting models (described above, and in Supplement Fig. S1.5) does not explicitly indicate resolution of features, but a relatively small standard deviation in output models does provide confidence that the inversion process is stable in converging to the presented model, even at depths of 50 km and greater.

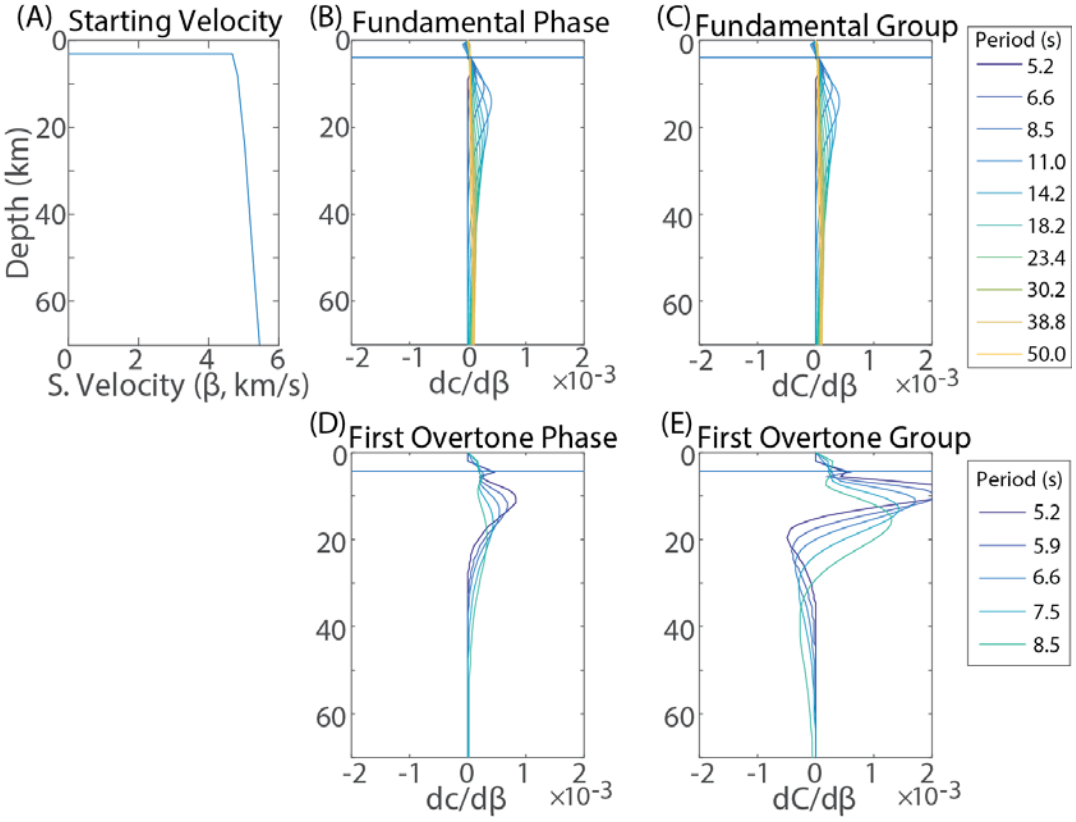

Figure 2.8: Depth sensitivity kernels using a 4-km-thick water layer and an average of our deep water 1D velocity profiles. (A) shows the starting model used, with a 4-km water depth being the predominant feature. (B) and (C) show group and phase sensitivities for the fundamental mode, while (D) and (E) show group and phase sensitivities for the first overtone.

2.5 Results and Discussion

Final shear-wave velocity model results are shown in Figs. 2.9 (plan views at different depths) and 2.10 (vertical cross sections). We observe that the Borderland region more closely resembles continental crust, with a distinct transition to oceanic structure moving west across the Patton Escarpment. Again, our model resolves lateral variations of roughly 50 km, and the vertical resolution is 5-10 km depending on depth. Our interpretation of the model is focused on a few specific structures, including the depth and shape of the Moho, defined here as the transition from about 3.7 km/s to 4.0 km/s. We also compare the Inner and Outer Borderland regions, consider the existence (or lack thereof) of a remnant

subducted slab, and hypothesize about the relatively diffuse, deeper structure underneath the Patton Escarpment and nearby seamounts.

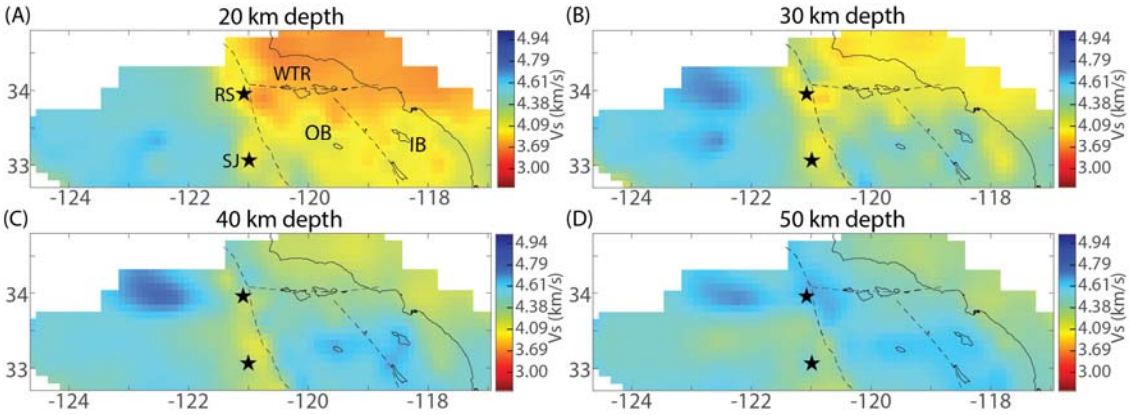

Figure 2.9: Plan views showing the final shear-wave velocity model at depths of 20 km (A), 30 km (B), 40 km (C) and 50 km (D). Stars indicate the location of the Rodriguez seamount (RS) and San Juan seamount (SJ). Tectonic provinces indicated include the Western Transverse Ranges (WTR), Outer Borderland (OB) and Inner Borderland (IB).

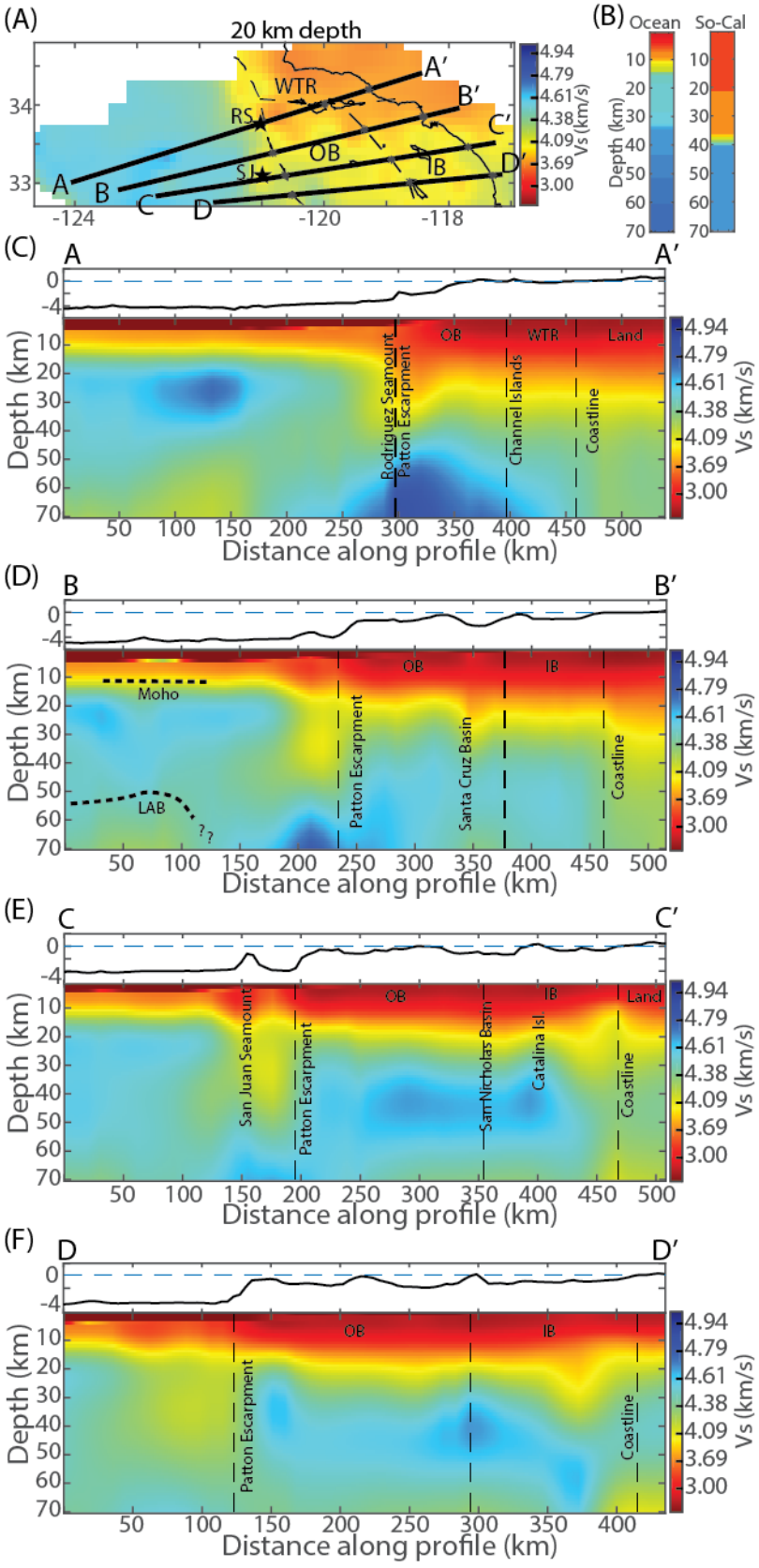
(A)
20 km depth
WTR
RS
SJ
OB
IB
A
A′
B
B′
C
C′
D
D′
34
33
-124
-120
-118
4.94
4.79
4.61
4.38
4.09
3.69
3.00
Vs (km/s)
(B)
Ocean
So-Cal
Depth (km)
(C)
Rodriguez Seamount
Patton Escarpment
Channel Islands
Coastline
Land
(D)
Moho
LAB
Santa Cruz Basin
(E)
San Juan Seamount
San Nicholas Basin
Catalina Isl.
(F)
Distance along profile (km)

Figure 2.10: Profiles of the final shear-wave velocity model. Dashed lines in the profiles indicate transitions between tectonic domains indicated on the map in panel (A). Two standard 1-D velocity profiles are provided for reference in panel (B): a standard oceanic average and a southern California average [*Kohler et al.,* 2003]. We note that because the ocean model is averaged over all oceanic lithosphere, any lithosphere-asthenosphere boundary is likely averaged out. Panels C-F show four cross sections through the 3D model.

We interpret a deeper Moho (~25 km) under the Western Transverse Ranges (Fig. 2.10A: profile A-A'), and crustal thinning in the Outer and Inner Borderland south of the Western Transverse Ranges (Fig. 2.10: B-B', C-C', D-D'). This is consistent with Western Transverse Ranges capture by the Pacific Plate and subsequent rotation (i.e., [*Nicholson et al.,* 1994]). We do not observe a crustal root as thick or wide as is observed beneath other continental lithosphere in the region (i.e., the on-land extent of the Transverse Ranges [*Hadley and Kanamori,* 1977; *Raikes,* 1980; *Walck and Minster,* 1982; *Humphreys and Clayton,* 1990; *Kohler,* 1999]), suggesting at least some deeper Borderland lithosphere was sheared away in the process of rotation. We observe a small concentration of anomalously thicker shallow crust, approximately 30 km thick by 30 km wide, just east of the Patton Escarpment in A-A' (roughly 310 km along profile), and interpret this to be the result of pinching between the westernmost endpoint of the rotating Western Transverse Ranges block and the northward-shifting Outer Borderland. We may be seeing the velocity signature of additional thickening or shearing at the edges of a block which has been rotated more than 90 degrees. The fast anomaly at depths greater than 50 km beneath the Outer Borderland in A-A' (325 km along profile) likely relates to the same processes, as mantle lithosphere is depleted or missing compared to other regions. This fast anomaly would likely be seen underneath other regions if our methodology allowed for deeper observations.

Comparing the Inner and Outer Borderland, we do not observe a significant difference in velocity structure. *Nicholson et al.* [1994] suggest that the Outer Borderland was laterally translated, with the bulk of extension and rotation occurring in the Inner Borderland. While our model does indicate small regions of slightly thinner crust in the Inner Borderland

(profile C-C'), the difference is minimal, and we suggest that deeper crust may have subsequently flowed eastward into the Inner Borderland to equilibrate the depths of these structures, analogous to observations from the Basin and Range [*Parsons,* 1995], where the Moho is observed to be flatter than might be expected underneath the extensional regime [*Klemperer et al.,* 1986].

The seismic velocity model is generally consistent with gravity inversions of the USGS and LARSE lines of *Miller* [2002] and *Romanyuk et al.* [2007], both of which incorporate near-surface seismic reflection data, borehole measurements, and magnetic anomalies. For example, the depth of the Moho, and the sloping increase in this depth across the coastline are evident in both models (Fig 2.10, profile C-C', between horizontal distances of 400 and 450 km). We observe a fast anomaly in the Santa Cruz Basin (Fig. 2.10, profile B-B', at a horizontal distance of 350 km) with a depth of 2-10 km, which *Miller* [2002] interprets as an outcrop of volcanic rocks, consistent with borehole measurements from *Bohannon and Geist* [1998]. Unlike the gravity inversions however, we observe a lower-velocity structure beneath the Santa Cruz Basin to a depth of 50 km, which we interpret as isostatic compensation for the denser shallow material above.

The existence of a remnant, thin, Farallon slab underplating either part of or the entire region is a subject of much debate [e.g., *Bohannon and Parsons*, 1995; *Fuis,* 1998; ten *Brink et al.,* 2000; *Nazareth and Clayton,* 2003; *Romanyuk et al.,* 2007]. We do not observe evidence for such a layer. A remnant slab would be observable as a thin, high-velocity layer at somewhere between 10-20 km depths. Even though our method lacks sharp resolution at this depth range, an underplated slab with a strong velocity contrast should still be evident, even if smoothed or blurred in our results. We also generally observe highly variable Moho depths under the Borderland. If any underplated slab exists, it must have been subject to the same deformation, thinning and isostatic compensation as the rest of the adjacent lithosphere, making it potentially difficult to image by this or any other technique.

The western side of our study region is characterized by fossil spreading center segments, volcanism and fracture zones associated with the East Pacific Rise (EPR), which stopped spreading approximately 18-20 Ma [*Atwater,* 1989; *Lonsdale,* 1991]. Two seamounts that resulted from EPR volcanic activity lie within the study region: the San Juan Seamount on the Pacific Plate and the Rodriguez Seamount lying on the continental slope (shown in Figs. 2.1, 2.9 and 2.10). Our velocity model suggests the persistence of uppermost mantle volcanic processes associated with EPR spreading and fracture zones. The most prominent of these seismic structures is a low-velocity anomaly underlying San Juan Seamount that can be traced throughout each cross section (e.g., Fig. 2.10 C-C' between horizontal distances 150 and 180 km). The low-velocity anomaly is about 30 km wide and has a depth extent of 50 km, well within good resolution limits. Similarly, a low-velocity seismic structure is observed below the Rodriguez Seamount (Fig. 2.10A), but the depth and lateral extent are complicated by the seamount's location at the endpoint of the rotating Transverse Ranges tectonic block [*Nicholson et al.,* 1994]. The San Juan Seamount is part of a chain of nine seamounts with NE-SW orientation off the coast of central and southern California. The seamounts were once islands that were the product of small-volume volcanic eruptions due to decompression melting of suboceanic mantle melts rising along zones of weakness in the oceanic crust [*Paduan et al.,* 2009; *Davis et al.,* 2010]. On the San Juan Seamount there is geochemical evidence for eruptions as recent as 2.8 Ma [*Paduan et al.,* 2009; *Davis et al.,* 2010]; thus our images may be showing thermal or chemical signatures of mantle upwelling of this age. The low-velocity anomaly is located laterally where mantle lithosphere is expected to thin between the Outer Borderland and Pacific oceanic plate to the west. Our images suggest a mantle lithosphere thickness, inferred from the seismic wave speeds, of at least 70 km below the region adjacent to and west of the Patton Escarpment as well as below the Outer Borderland, and 60 km below the Pacific Plate. The presence of small-scale mantle flow may be producing heterogeneous crustal and mantle lithospheric thicknesses below both oceanic and continental tectonic regimes.

We propose that the ~50-km-wide (laterally) region west of the fossil subduction zone (Patton Escarpment) can be described as a thickened lithospheric bulge of slower material, related to the same remnant upwelling asthenosphere responsible for the seamounts described above. While near-surface geology, magnetic anomalies and bathymetry indicate that the relatively sharp Patton Escarpment relates to ancient subduction, the deeper structure currently present does not directly resemble a subduction zone. For example, this is not part of the accretionary prism lying adjacent to the bulge since the prism's western boundary is marked by the Patton Escarpment. Upwelling magma may be ponding at the base of the crust, resulting in thickening and ongoing adjustment of the lithosphere due to the localized loading. Ongoing cooling and accretion to the underside of the crust could explain an environment enabling the occurrence of deeper earthquakes (>30km) south of the study area but within a similarly narrow band west of the fossil subduction zone [*Hauksson et al.,* 2013]. Anomalously thick oceanic crust and mantle lithosphere has also been observed in a receiver function study using the same OBS dataset [*Reeves et al.,* 2015]. From the spatial correlation of this thicker crust with the seamounts and Patton Escarpment (low-velocity anomaly west of the Patton Escarpment in cross sections C-C' and D-D'), we believe the deeper structure of this transition from oceanic lithosphere to the continental borderland is defined by such upwelling, rather than ancient subduction.

The new velocity model presented here provides the first complete view of the deeper seismic structure offshore southern California. It provides a basis for future inversions and modeling with joint datasets, as well as a framework for earthquake locations and ground shaking simulations for assessing risk associated with offshore faults. It suggests a number of implications regarding the region's tectonic history: The region marking the transition from continental to oceanic crust across the Patton Escarpment is surprisingly diffuse over small length scales, and marked by upwelling associated with spreading center volcanism. It also suggests that lithospheric scale structure under the thinned Inner Borderland has equilibrated since the time of rotation of the Western Transverse Ranges.

2.6 Acknowledgments and Data

The authors thank Fan-Chi Lin for assistance with the initial signal processing, tilt and DPG corrections, and dispersion measurements, Yiran Ma for assistance with the 2D inversions, and Rob Clayton, Asaf Inbal, Joann Stock, Simon Klemperer and Sampath Rathnayaka for helpful discussions. The final model is available by contacting the corresponding author at dbowden@caltech.edu. SCSN data were provided by the Caltech/USGS Southern California Seismic Network at http://scedc.caltech.edu/ [Caltech, 1926]. The OBS and DPG waveform data from the ALBACORE array are available from the IRIS Data Management Center at http://www.iris.edu/hq/. The IRIS Data Management System is funded through the National Science Foundation and specifically the GEO Directorate through the Instrumentation and Facilities Program of the National Science Foundation under Cooperative Agreement EAR-1063471. The OBS deployment was made possible with instruments and logistical support of the U.S. National Ocean Bottom Seismic Instrumentation Pool (OBSIP) at Scripps Institute of Oceanography; in particular, thanks go to Jeff Babcock, Ernie Aaron, Phil Thai, and Mark Gibaud. The OBS deployment and recovery cruises were made possible with the equipment and logistical support of the University-National Oceanographic Laboratory System (UNOLS) vessel fleet and staff support at Scripps with particular thanks to Jon Meyer, Brian Rowe, and Meghan Donohue. Kohler and Weeraratne thank Captain Curl and the crew of R/V Melville for assistance during the 2010 OBS deployment cruise, and Captain Vullo and the crew of R/V New Horizon during the 2011 OBS recovery cruise. This work was supported by the National Science Foundation (grant # OCE-0825254) and by USGS grant G14AP00074.

2.7 References

Atwater, T. (1970), Implications of plate tectonics for the Cenozoic tectonic evolution of Western North America, *Geol. Soc. Am. Bull., 81*, 3513-3536.

Atwater, T. (1989), Plate tectonic history of the northeast Pacific and western North America, *The Eastern Pacific ocean and Hawaii, Geological Society of America, The Geology of North America. v. N*, 21–72.

Atwater, T., and J. Stock (1998), Pacific-North America Plate Tectonics of the Neogene Southwestern United States: An Update, *Int. Geol. Rev.*, *40*(5), 375–402, doi:10.1080/00206819809465216.

Barmin, M. P., M. H. Ritzwoller, A. L. Levshin, (2001), A fast and reliable method for surface wave tomography, *Pure Appl. Geophys.*, *158*(8), 1351–1375, doi:http://dx.doi.org/10.1007/PL00001225.

Bell, S. W., D. W. Forsyth, and Y. Ruan (2015), Removing Noise from the Vertical Component Records of Ocean-Bottom Seismometers: Results from Year One of the Cascadia Initiative, *Bull. Seismol. Soc. Am.*, *105*(1), 300–313, doi:10.1785/0120140054.

Bensen, G. D., M. H. Ritzwoller, M. P. Barmin, A. L. Levshin, F. Lin, M. P. Moschetti, N. M. Shapiro, and Y. Yang (2007), Processing seismic ambient noise data to obtain reliable broad-band surface wave dispersion measurements, *Geophys. J. Int.*, *169*(3), 1239–1260, doi:10.1111/j.1365-246X.2007.03374.x.

Bohannon, R. G., and E. Geist (1998), Upper crustal structure and Neogene tectonic development of the California continental borderland, *Geol. Soc. Am. Bull.*, *110* (6), 779–800, doi:10.1130/0016-7606(1998)110<0779:UCSANT>2.3.CO;2 .

Bohannon, R. G., and T. Parsons (1995), Tectonic implications of post-30 Ma Pacific and North American relative plate motions, *Geol. Soc. Am. Bull.*, *107* (8), 937–959, doi:10.1130/0016-7606(1995)107<0937:TIOPMP>2.3.CO;2.

California Institute of Technology (Caltech) (1926): Southern California Seismic Network. International Federation of Digital Seismograph Networks. Other/Seismic Network. doi:10.7914/SN/CI

Crawford, W. C., and S. C. Webb (2000), Identifying and Removing TiltNoise from Low Frequency LT0.1Hz Seafloor Vertical Seismic Data, *Bull. Seismol. Soc. Am.*, *90*(4), 952–963.

Crouch, J. K., and J. Suppe (1993), Late Cenozoic Tectonic Evolution of the Los-Angeles Basin and Inner California Borderland - a Model for Core Complex Like Crustal Extension, *Geol. Soc. Am. Bull.*, *105*(11), 1415–1434, doi:10.1130/0016-7606(1993)105<1415:LCTEOT>2.3.CO;2.

Crowell, J. C. (1968), Movement histories of faults in the Transverse ranges and speculations on the tectonic history of California, in *Proceedings of the Conference on Geologic Problems of the San Andreas Fault System*, edited by W. R. Dickinson and A. Grantz, *Stanford Univ. Publ. Geol. Sci., 11*, 323-341.

Davis, A. S., D. A. Clague, J. B. Paduan, B. L. Cousens, and J. Huard (2010), Origin of volcanic seamounts at the continental margin of California related to changes in plate margins, *Geochem. Geophys. Geosyst.*, *11*(5), Q05006, doi:10.1029/2010gc003064.

Dokka, R. K. (1989), The Mojave extensional belt of Southern California, *Tectonics, 8*, 363-390.

Dziewonski, A. M., & Anderson, D. L. (1981). Preliminary reference Earth model. *Phys. Earth Planet. Inter., 25*(4), 297-356.

Dziewonski, A. M., A. L. Hales, and E. R. Lapwood (1975), Parametrically simple earth models consistent with geophysical data, *Phys. Earth Planet. Inter.*, *10*(1), 12–48, doi:10.1016/0031-9201(75)90017-5.

Feigl, K. L. et al. (1993), Space geodetic measurement of crustal deformation in central and southern California, 1984–1992, *J. Geophys. Res.*, *98* (B12), 21677, doi:10.1029/93JB02405.

Fuis, G. S. (1998), West margin of North America — a synthesis of recent seismic transects, *Tectonophysics*, *288*(1-4), 265–292, doi:10.1016/S0040-1951(97)00300-4.

Fuis, G. S. et al. (2003), Fault systems of the 1971 San Fernando and 1994 Northridge earthquakes, southern California: Relocated aftershocks and seismic images from LARSE II, *Geology*, *31* (2), 171–174, doi:10.1130/0091-7613(2003)031<0171:FSOTSF>2.0.CO;2.

Fuis, G. S., D. S. Scheirer, V. E. Langenheim, and M. D. Kohler (2012), A new perspective on the Geometry of the San Andreas fault in southern California and its relationship to Lithospheric structure, *Bull. Seismol. Soc. Am.*, *102* (1), 236–251, doi:10.1785/0120110041.

Gao, H., and Y. Shen (2015), A Preliminary Full-Wave Ambient-Noise Tomography Model Spanning from the Juan de Fuca and Gorda Spreading Centers to the Cascadia Volcanic Arc, *Seismol. Res. Lett.*, *86*(5), 1253–1260, doi:10.1785/0220150103.

Gimbert, F., and V. C. Tsai (2015), Predicting short-period, wind-wave-generated seismic noise in coastal regions, *Earth Planet. Sci. Lett.*, *426*, 280–292, doi:10.1016/j.epsl.2015.06.017.

Hadley, D., and H. Kanamori (1977), Seismic structure of the Transverse Ranges, California, *Geol. Soc. Am. Bull.*, *88* (10), 1469–1478, doi:10.1130/0016-7606(1977)88<1469:SSOTTR>2.0.CO;2.

Harmon, N., D. Forsyth, and S. Webb (2007), Using ambient seismic noise to determine short-period phase velocities and shallow shear velocities in young oceanic lithosphere, *Bull. Seismol. Soc. Am.*, *97*(6), 2009–2023, doi:10.1785/0120070050.

Hauksson, E., H. Kanamori, J. Stock, M.-H. Cormier, and M. Legg (2013), Fracturing the eastern edge of the Pacific Ocean lithosphere as evidenced by seismicity in the abyssal plain off Baja California, Mexico *Geophys. J. Int*., doi:10.1093/gji/gg1467

Herrmann, R. B. (2013), Computer Programs in Seismology: An Evolving Tool for Instruction and Research, *Seismol. Res. Lett.*, *84*(6), 1081–1088, doi:10.1785/0220110096.

Humphreys, E., and R. Clayton (1990), Tomographic Image of the Southern California Mantle, *J. Geophys. Res.*, *95*(B12), 19725–19746.

Klemperer, S. L., Hauge, T. A., Hauser, E. C., Oliver, J. E., & Potter, C. J. (1986). The Moho in the northern Basin and Range province, Nevada, along the COCORP 40 N seismic-reflection transect. *Geological Society of America Bulletin*, *97*(5), 603-618.

Kohler, M. D. (1999), Lithospheric deformation beneath the San Gabriel Mountains in the southern California Transverse Ranges, *J. Geophys. Res.*, *104*(B7), 15025, doi:10.1029/1999JB900141.

Kohler, M. D., H. Magistrale, and R. W. Clayton (2003), Mantle Heterogeneities and the SCEC Reference Three-Dimensional Seismic Velocity Model Version 3, *Bull. Seismol. Soc. Am.*, *93*(2), 757–774, doi:10.1785/0120020017.

Kohler, M., K. Booth, C. Sun, C. Curl, C. Finnell, P. Shute, W. B. Prine, J. Ramos, and W. Brown (2011), ALBACORE OBS Deployment Cruise Report, *R/V Melville* Cruise MV1010, 27 pp., 14-27 Aug. 2010

Kohler, M., K. Brunner, M. Donohue, D. Weaver, T. Chi, and M. Breen (2012), ALBACORE OBS Recovery Cruise Report, *R/V New Horizons* Cruise NH1111, 35 pp., 7-16 Sept. 2011

Legg, M. R. (1991), Developments in understanding the tectonic evolution of the California Continental Borderland, in *From Shoreline to Abyss,* vol 46, edited by R. H. Osborne, pp. 291-312, SEPM Shepard Commemorative., Tulsa, Okla.

Legg, M. R., M. D. Kohler, N. Shintaku, and D. S. Weeraratne (2015), High-resoolution mapping of two large-scale transpressional fault zones in the California Continental Borderland: Santa Cruz-Catalina Ridge and Ferrelo faults, *J. Geophys. Res. Earth Surf.*, *120*, 915–942, doi:10.1002/2014JF003322.

Levshin, A. L., and M. H. Ritzwoller (2001), Automated Detection, Extraction, and Measurement of Regional Surface Waves, *Pure Appl. Geophys.*, *158*(8), 1531–1545, doi:10.1007/978-3-0348-8264-4_11.

Lin, F. C., M. H. Ritzwoller, and N. M. Shapiro (2006), Is ambient noise tomography across ocean basins possible?, *Geophys. Res. Lett.*, *33*(14), 1–5, doi:10.1029/2006GL026610.

Longuet-Higgins, M. S. (1950), A Theory of the Origin of Microseisms, *Philos. Trans. R. Soc. London A Math. Phys. Eng. Sci.*, *243*(857), 1–35, doi:10.1098/rsta.1979.0079.

Lonsdale, P. (1991), Structural patterns of the Pacific floor offshore of Peninsular California, in: "The Gulf and Peninsular Province of the Californias," (chapter 7), Edited by J. P. Dauphin and B. R. T. Simoneit, AAPG Memoir, 47, 87-125.

Loris, I., Nolet, G., Daubechies, I., & Dahlen, F. A. (2007). Tomographic inversion using ℓ1-norm regularization of wavelet coefficients. *Geophysical Journal International*, *170*(1), 359-370.

Luyendyk, B. P. (1991), A model for Neogene crustal rotations, transtension, and transpression in southern California, *Geol. Soc. Am. Bull., 103*, 1528-1536.

Ma, Y., and R. W. Clayton (2014), The crust and uppermost mantle structure of Southern Peru from ambient noise and earthquake surface wave analysis, *Earth Planet. Sci. Lett.*, *395*, 61–70, doi:10.1016/j.epsl.2014.03.013.

Miller, K. (2002), Geophysical evidence for Miocene extension and mafic magmatic addition in the California Continental Borderland, *Geol. Soc. Am. Bull.*, *114*(4), 497–512, doi:10.1130/0016-7606(2002)114<0497:GEFMEA>2.0.CO;2.

Nazareth, J. J., and R. W. Clayton (2003), Crustal structure of the Borderland-Continent transition zone of southern California adjacent to Los Angeles, *J. Geophys*., 108, B8, 2404 doi:10.1029/2001JB000223.

Nicholson, C., C. C. Sorlien, T. Atwater, J. C. Crowell, and B. P. Luyendyk (1994), Microplate capture, rotation of the western Transverse Ranges, and initiation of the San Andreas transform as a low-angle fault system, *Geology*, *22*(6), 491–495, doi:10.1130/0091-7613(1994)022<0491:MCROTW>2.3.CO;2.

Paduan, J. B., D. A. Clague, and A. S. Davis (2009), Evidence that three seamounts off southern California were ancient islands, *Mar. Geol.*, *265*(3-4), 146–156, doi:10.1016/j.margeo.2009.07.003.

Parsons, T. (1995). The basin and range province. *Continental Rifts: Evolution, Structure, Tectonics*, *25*, 277-324.

Raikes, S. A. (1980), Regional variations in upper mantle structure beneath Southern California, *Geophys. J. R. astr. Soc*., *63*, 187-216.

Reeves, Z., V. Lekić, N. Schmerr, M. Kohler, D. Weeraratne (2015), Lithospheric structure across the California Continental Borderland from receiver functions, *Geochemistry, Geophys. Geosystems*, *16*(1), 246–266, doi:10.1002/2014GC005617.

Romanyuk, T., W. D. Mooney, and S. Detweiler (2007), Two lithospheric profiles across southern California derived from gravity and seismic data, *J. Geodyn.*, *43*(2), 274–307, doi:10.1016/j.jog.2006.09.011.

Shaw, J. H., A. Plesch, C. Tape, M. P. Suess, T. H. Jordan, G. Ely, E. Hauksson, J. Tromp, T. Tanimoto, R. Graves and K. Olsen (2015), Unified Structural

Representation of the southern California crust and upper mantle, *Earth Planet. Sci. Lett.*, *415*, 1–15, doi:10.1016/j.epsl.2015.01.016.

Shen, Z., D. D. Jackson, and B. X. Ge (1996), Crustal deformation across and beyond the Los Angeles basin from geodetic measurements, *J. Geophys. Res., 101*, 27, 957-27, 980.

Stock, J. M., and K. V. Hodges (1989), Pre-Pliocene extension around the Gulf of California and the transfer of Baja California to the Pacific plate, *Tectonics, 8*, 99-115.

ten Brink, U. S., J. Zhang, T. M. Brocher, D. A. Okaya, K. D. Klitgord, and G. S. Fuis (2000), Geophysical evidence for the evolution of the California Inner Continental Borderland as a metamorphic core complex, *J. Geophys. Res.*, *105* B3, 5835–5857, doi:10.1029/1999JB900318

Tennyson, M. E. (1989), Pre-transform early Miocene extension in western California, *Geology, 17*, 792-796.

Vedder, J. G., L. A. Beyer, A. Junger, G. W. Moore, A. E. Roberts, J. C. Taylor, and H. C. Wagner (1974), *Preliminary report on the geology of the continental borderland of Southern California*. No. 264

Walck, M. C., and J. B. Minster (1982), Relative array analysis of upper mantle lateral velocity variations in Southern California, *J. Geophys. Res.*, *87*, 1757-1772.

Walls, C., T. Rockwell, K. Mueller, Y. Bock, S. Williams, J. Pfanner, J. Dolan, and P. Fang (1998), Escape tectonics in the Los Angeles metropolitan region and implications for seismic risk, *Nature, 394*, 356-360.

Webb, S. C. (1998), Broadband seismology and noise under the ocean, *Rev. Geophys.*, *36*(1), 105–142, doi:10.1029/97RG02287.

Webb, S. C., and W. C. Crawford (1999), Long-period seafloor seismology and deformation under ocean waves, *Bull. Seismol. Soc. Am.*, *89*(6), 1535–1542.

Weigand, P. W. (1994), Petrology and geochemistry of Miocene volcanic rocks from Santa Catalina and San Clemente Islands, California, in *Proceedings of the Fourth California Island Symposium,* edited by W. L. Halvorson and G. J. Maender, pp. 267-280, Santa Barbara Museum of Natural History, Santa Barbara, Calif.

Wright, T. L. (1991), Structural geology and tectonic evolution of the Los Angeles basin, California, in *Active Margin Basins*, edited by K. T. Biddle, *AAPG Mem. 52*, 35-134.

Yao, H., P. Gouédard, J. A. Collins, J. J. McGuire, and R. D. van der Hilst (2011), Structure of young East Pacific Rise lithosphere from ambient noise correlation analysis of fundamental- and higher-mode Scholte-Rayleigh waves, *Comptes Rendus - Geosci.*, *343*(8-9), 571–583, doi:10.1016/j.crte.2011.04.004.

Chapter 3

SITE AMPLIFICATION, ATTENUATION AND SCATTERING FROM NOISE CORRELATION AMPLITUDES ACROSS A DENSE ARRAY IN LONG BEACH, CA

Bowden, D. C., Tsai, V. C., & Lin, F. C. (2015). Site amplification, attenuation, and scattering from noise correlation amplitudes across a dense array in Long Beach, CA. *Geophysical Research Letters*, *42*. https://doi.org/10.1002/2014GL062662

3.1 Abstract

For accurate seismic hazard evaluation, both the spatial and frequency-dependent variabilities in the amplitudes of earthquake ground motions are needed. While this information is rarely fully available due to the paucity of relevant seismic data, dense arrays like the 5200-geophone array in Long Beach, California provide the opportunity to study this amplitude variability. Here we show that ambient noise correlation amplitudes from the Long Beach array can be used to directly determine frequency-dependent site amplification factors. We analyze Rayleigh-wavefield amplitude gradients from ambient noise correlations that are processed so that relative amplitudes satisfy the wave equation and are therefore meaningful. Ultimately, we construct maps of site amplification across Long Beach at frequencies of 0.67, 1.0, and 2.0 Hz. These maps correlate well with local structure, notably the Newport-Inglewood Fault, and also to known velocity structure. Through this process, we also obtain constraints on average attenuation structure and local scattering.

3.2 Introduction

Traditional seismic hazard studies have primarily focused on describing the expected shaking from potential future earthquakes based on empirical observations of previous earthquakes [e.g., *Abrahamson and Shedlock*, 1997; *Cua and Heaton*, 2012]. These observations have shown that the amplitudes of seismic waves can be strongly affected by shallow crustal heterogeneities. For example, ground motions in sedimentary basins have historically shown

significantly higher amplitudes of ground motion compared to hard-rock sites a few kilometers away. Despite attempts to spatially map these variations, the sparsity of available data from historic events usually necessitates reliance on averaged characterizations for a given region or material type (i.e., sediments versus hard rock). Unfortunately, such averages do not describe the complex and frequency-dependent patterns of wave propagation and so often fail to provide realistic estimates of the lateral variability of ground motion amplitudes [*Graves et al.*, 2010].

Effects of shallow crustal heterogeneities on ground motion amplitudes can be observed more robustly and systematically with arrays of seismometers that are dense relative to the features of interest, which have only recently become technologically feasible or affordable. For example, *Lin et al.* [2012] was able to track the Rayleigh wavefronts of distant earthquakes across the USArray to infer site amplification and attenuation, which showed strong agreement with known geologic structure. However, the observations were only available in the lower frequency range of 0.01 to 0.04 Hz (with higher frequencies being too highly attenuated), while engineers studying seismic hazard are often most concerned with building resonances at higher frequencies (i.e., in the range of 0.5–2.0 Hz) [*Kohler et al.*, 2005].

Ambient noise cross correlations provide a signal rich in these higher frequencies and offer the flexibility of making observations in the absence of earthquakes [*Shapiro*, 2004]. A particularly dense array of more than 5200 geophones in Long Beach, CA, with an average station spacing of only 100 m, allowed *Lin et al.* [2013] to track phase traveltimes across the array, and the shallow velocity structure resolved shows strong correlations with the Newport-Inglewood Fault running through the array. Other studies have focused on directly observing amplitudes from ambient noise cross-correlation functions [e.g., *Prieto and Beroza*, 2008; *Denolle et al.*, 2014; *Lin et al.*, 2011; *Zhang and Yang*, 2013], and such methods show promising similarity to observed earthquake amplifications. Careful treatment is required, however, as a heterogeneous distribution of noise sources can bias the noise

correlation amplitudes if not properly accounted for [*Weaver*, 2011; *Tsai*, 2011]. In this paper, we use ambient noise cross correlations of the Long Beach array with the Helmholtz wavefront tracking approach of *Lin et al.* [2012] to recover the spatial variability of site amplifications and demonstrate that tracking amplitudes across an array is insensitive to the initial distribution of those amplitudes. We compare our site amplification results with the phase velocity observations of *Lin et al.* [2013] as well as earthquake and nuclear testing observations.

3.3 Theoretical Background

The wavefront tracking approach of *Lin et al.* [2012] (derived in Supplementary Materials S3) considers the observed amplitudes $A(x, y)$ and traveltimes $\tau(x, y)$ of a 2-D Rayleigh wavefield (the spatial wavefield corresponding to the Rayleigh wave arrival) across an array and uses the following relation derived from the 2-D Helmholtz wave equation:

$$\frac{2\nabla\beta \cdot \nabla\tau}{\beta} - \frac{2\alpha}{c} + S = \frac{2\nabla A \cdot \nabla\tau}{A} + \nabla^2\tau \qquad \text{Eq. 3.1}$$

where β is a local site amplification factor for Rayleigh waves, α is an attenuation constant, and c is phase velocity [*Lin et al.*, 2012]. The term α refers to intrinsic attenuation and relates to the more commonly used Q factor by $\alpha = \pi f/CQ$, where f is frequency and C is group velocity. Here we consider the more general solution of the inhomogeneous Helmholtz equation where a source term, S, (which is explained later) is added to the result of *Lin et al.* [2012]. Based on equation 3.1, the observed amplitude variation corrected by wavefront focusing and defocusing (i.e., by the $\nabla^2\tau$ term) can be related to the local amplification variation, attenuation, and internal sources (terms on the left-hand side of equation 3.1). These terms can be further decoupled, as the effect of both attenuation and internal sources is to consistently and statically decrease or increase amplitudes, respectively, while the site amplification term (quantified by the scalar β) will show different effects depending on the direction of wave propagation and observation (i.e., propagation into or out of a sedimentary basin) [*Lin et al.*, 2012]. The advantage of the wavefront tracking method can be seen in that we are concerned with only local wavefield variations and not the initial conditions of the

wave excitation. To use the wavefront tracking approach on ambient noise cross correlations, we must be able to construct a 2-D wavefield that satisfies the wave equation. Since cross correlation is a linear operator that acts on the background noise wavefield regardless of where that source originates, observations from noise cross correlation between one center station (the virtual source) and all other stations across the array still satisfy the wave equation [*Lin et al.*, 2013]. We can observe both an incoming wavefield from the negative lag times of the cross correlations and an outgoing wavefield from the positive lag times. Importantly, we do not force a symmetric form of the noise correlation function (NCF) in our analysis, as is often done in other noise processing applications [i.e., *Lin et al.*, 2013], because this effectively reverses time for the inward traveling signals and consequently reverses the effect of intrinsic attenuation.

Analyzing the two components separately allows us to determine the effects and strengths of internal, local sources as compared to attenuation. These sources may be any repeated, impulsive source of energy such as highway or factory noise. Similarly, elastic scatters may be viewed as point sources of energy and, in very geologically heterogeneous regions, this scattering may be the dominant contribution. In either case, when a local source is present, the positive or negative lag cross-correlated signal will increase when the local source is within the corresponding stationary-phase hyperbola of a given station pair [*Snieder*, 2004]. Thus, the incoming noise cross-correlation wavefield (negative lag) will increase in amplitude when passing through the source location, as the focus of the stationary-phase hyperbola is moving with the wavefield. On the other hand, the focus of the stationary-phase hyperbola is fixed at the center station location for the outgoing wavefield (positive lag), and hence the wavefield amplitude is not going to be affected by the source. Thus, by studying both directionally dependent incoming and outgoing amplitude variations, the spatial variability of all three terms can, in theory, be resolved. This is explained in further detail in Supplementary Materials section S4.

3.4 Data and Methods

In order to make use of ambient noise correlation amplitudes from the Long Beach array (or any array), special care must be taken to preserve relative amplitudes and ensure the cross correlations satisfy the wave equation. One way to ensure this is to use raw waveforms in the cross correlation [*Prieto and Beroza*, 2008], but the noisy urban environment and short time span of our data (about 3 weeks) resulted in raw NCFs for which clear group arrivals could not be determined. Unfortunately, many of the commonly accepted signal processing techniques such as time domain normalization or spectral prewhitening [*Bensen et al.*, 2007] act on a signal by smoothing, normalizing, or otherwise altering that specific signal. Such individual modifications to a waveform nonlinearly affect the relative signal amplitudes and our assumptions about the wave equation would no longer hold. To maintain linearity, any processing must be applied equally across all signals for the same time period. To accomplish this, we whiten all of the spectra for a given hour using a single spectral envelope that represents the 95th percentile of the entire 5200-station array. Similarly, once the noise cross correlations have been computed for a given hour, we consider the 95^{th} percentile of all NCF peak amplitudes for the hour and inversely weight each record by this number before including them in the final stack. These whole-array techniques are not as effective at cleaning up the group arrivals as single station treatments, but they do accomplish the same goal of increasing the NCFs signal to noise ratio by reducing the effect of noise sources that are impulsive in time, space, or frequency [*Weaver*, 2010], while maintaining linearity.

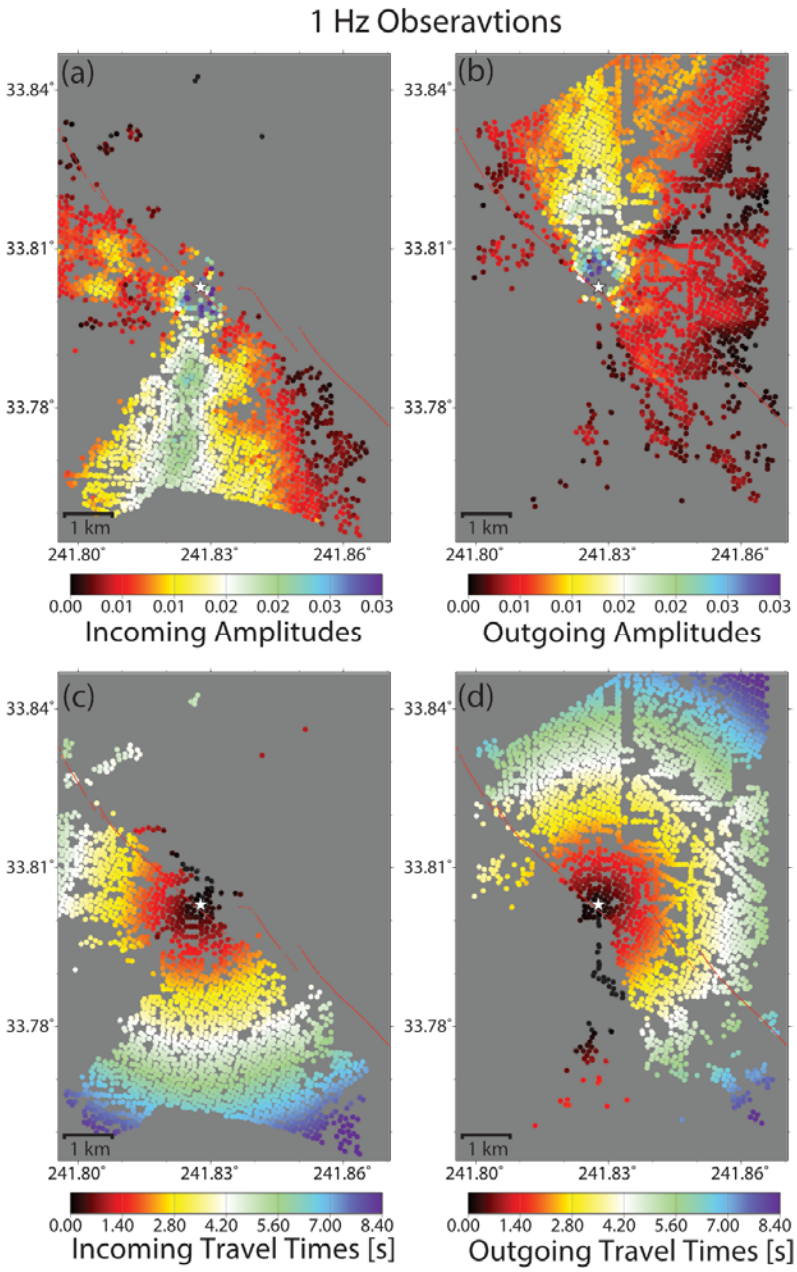

Figure 3.1: Example observations from NCFs at 1 Hz. Maps of (A) amplitude, *A*, and (C) phase traveltime, τ, of the incoming wavefronts, and maps of (B) amplitude, *A*, and (D) phase traveltime, τ, of the outgoing wavefronts. We observe a strong south-to-north trend in the amplitudes, as signal energy is strongest from near the coastline to the south (with stations with low SNR removed). Note that the amplitudes are treated such that the relative magnitudes are preserved but are normalized and effectively unitless. The white star in each map is the station that was used as a virtual source for this example.

Using all possible stations as virtual sources, maps describing phase traveltimes, τ, and the associated amplitudes, A, were collected at narrow band-pass windows of 0.67 Hz, 1.0 Hz, and 2.0 Hz (e.g., as in Figure 3.1). Measurements are only selected for which the signal-to-noise ratio (SNR, defined as peak amplitude divided by the root-mean-square of the trace) is above a cutoff: SNR > 8 at 0.67 Hz and 1 Hz, and SNR > 4 at 2 Hz. We note that while an identical selection criterion of SNR > 4 can be used for the three frequencies, pushing this threshold higher where possible allows us to suppress spurious measurements and reduce overall uncertainties. The actual results are minimally affected by SNR since our method is theoretically not affected by correlation noise level, unlike with coherency methods. A strong northward "cone" of energy is apparent in the amplitude maps for both the inward and outward propagation directions and is associated with a stronger source of noise energy from the coastline along the southern border of the array. Weak directions are also apparent, including large areas for which the data have been suppressed by the SNR cutoff. Although urban sources of noise should be strong in the region, northward traveling energy dominates the raw waveforms at these frequencies and so the cross correlations are sensitive predominantly to that presumably ocean-generated energy. This biased distribution of amplitudes is part of the reason that noise correlation functions should not typically be interpreted as pure Green's Functions and why we favor the wavefront tracking method (i.e., a method that compares relative measurements along each azimuth).

3.5 Results

With observations of amplitude variability as wavefronts cross some point in the array, calculated from the right-hand side of equation (1), we can solve for the effect of amplification, attenuation, and internal source terms on the left-hand side. For each location, the observations from both incoming and outgoing wavefields are plotted against the wave propagation azimuth (e.g., Figure 3.2), and a sine curve with 360◦ periodicity and some static offset is fit ("1ψ", from *Lin et al.* [2012]). This sine curve describes the direction and magnitude of highest amplification, as well as the overall static loss or addition of energy from attenuation and internal sources, respectively. Note that the observed amplitude

variations are generally higher for incoming observations compared to outgoing, which is consistent with the expectation that internal sources should only add energy to the incoming wavefield. We also note that any elastic effect such as anisotropy should already be removed with the focusing/defocusing term and should not affect our amplitude observations.

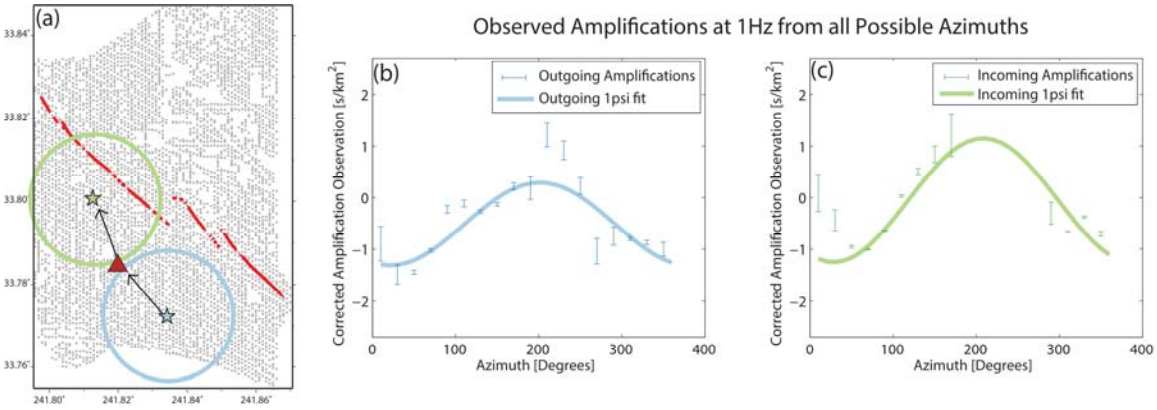

Figure 3.2: (A) Example of how observed amplifications (both outgoing in blue and incoming in green) provide multiple directions of measurement for a given point, shown with a red triangle. These observations and corresponding 1ψ fits for (B) outgoing and (C) incoming waves treated independently. Error bars represent 1 sigma confidence intervals and are omitted where no observations were present. Differences in the vertical offsets of the 1ψ fits can be explained by the fact that sources are only seen on the incoming wavefronts, while the difference in magnitude may result from numerical uncertainties.

While the effect of all three terms on the left-hand side of equation 3.1 can in theory be distinguished for all locations within the array, in practice we are limited by the inhomogeneous source distribution that is dominated by coastal energy (the northward bias in Figure 3.1). The incomplete range of azimuthal observations prevents us from confidently determining a 1ψ fit and the spatial pattern of attenuation structure. To quantify the effect of attenuation in general, we estimate the averaged loss of energy across the whole array by averaging all of the amplitude variation measurements of outgoing wavefields, assuming that the directional effects of local amplifications will cancel out. This loss of energy, which we attribute to the intrinsic attenuation term $2\alpha/c$, is 0.22 s/km^2 averaged for all 3 frequencies

(which corresponds to a Q value of roughly 140). For comparison, we can consider the averaged difference in static offset between the outgoing and incoming observations where both are available, which relates to the intensity of local sources or scatterers, and these are 0.31 s/km^2. Enough observations of both incoming and outgoing measurements are only possible in the center regions of our array, and an example is shown in Figure 3.3 for our observed source terms at 0.67 Hz. This map correlates with regions of low phase velocity from *Lin et al.* [2013], presented later for reference, which may suggest we are seeing predominantly scattered wavefronts off of damaged materials or loose sediments, rather than new sources of impulsive energy. One might have expected to see stronger scattering along strong velocity contrasts, but this is not observed.

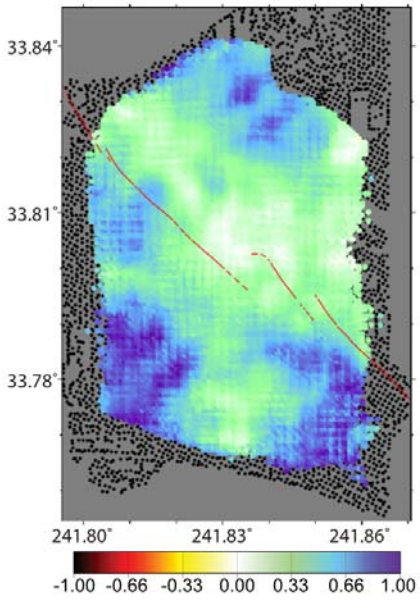

Figure 3.3: Strength of sources or scattering measured by comparing the incoming and outgoing signals at 0.67 Hz, where enough measurements for both directions are present. Specifically, we subtract the outgoing measurements from the right-hand side of equation (3.1), for a given azimuth, from the incoming measurements, and average over available azimuths. Incoming signals are sensitive to sources/scatterers, while outgoing signals are not.

Based on the observations above, the attenuation and source terms are relatively small compared to the magnitude of actual variation caused by site amplification. Thus, these small static offsets should not strongly affect the measurement of amplification magnitude and direction, and so we treat the incoming and outgoing signals as approximately equal in order to collect a more complete azimuthal dependence and more robustly fit sine curves. With the directions and magnitudes of maximum amplification for each site, we invert for a single multiplicative factor, β, that best represents site response following the convention of *Lin et al.* [2012]. Maps of β are shown in Figure 3.4 for 0.67 Hz, 1.0 Hz, and 2.0 Hz, and for comparison, we also show the phase velocity measurements from *Lin et al.* [2013] at the appropriate frequency below each amplification map. The frequencies of the phase velocity maps displayed are different because the depth sensitivity kernels for site amplification and phase velocity vary, and the frequencies are chosen to probe crustal structure of roughly the same depth (see Figure 3.5). These sensitivity kernels are calculated as in *Lin et al.* [2012] by numerically perturbing shear wave velocities at each depth. We also note that despite site amplification likely having smaller-scale heterogeneity, our final maps have resolution on the order 500 m, which is limited by both station spacing (about 100 m) and the wavelengths involved [*Lin et al.*, 2013].

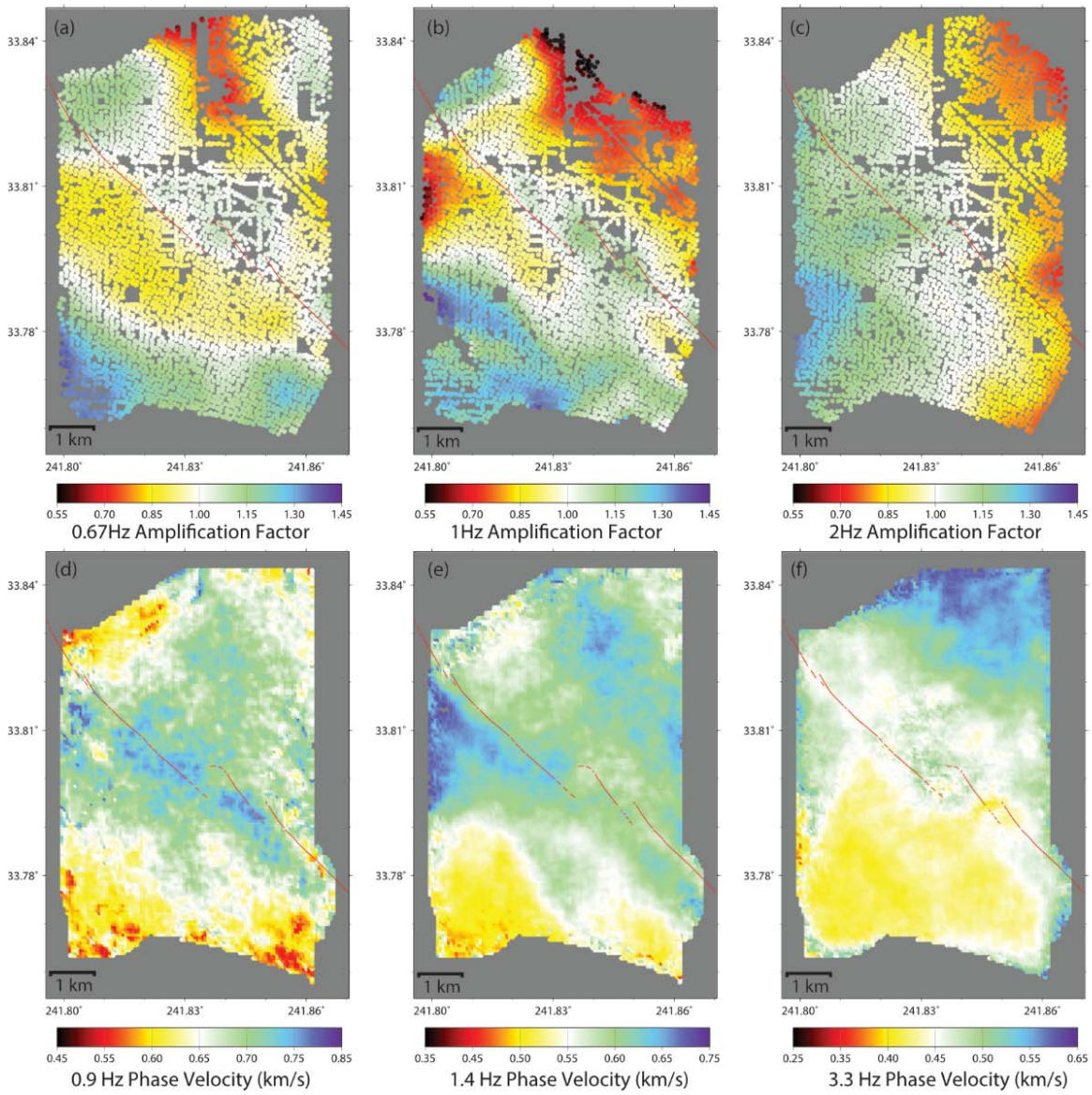

Figure 3.4: Relative site amplification factors at (A) 0.67 Hz, (B) 1.0 Hz and (C) 2.0 Hz. Shown below each amplification map is the (D-F) phase velocity map from *Lin et al.* [2013] which has the closest matching sensitivity kernel for the amplification map above it.

These new, high-resolution maps of site amplification show how ground motions are amplified as waves propagate across the array. They suggest that amplitudes in areas to the southwest will be significantly higher than areas to the northeast. These maps also correlate inversely with phase velocities, as might be expected (e.g., decreases in shear wave velocity

cause both decreases in phase velocities and increases in amplitude as shown in Figure 3.5), but the geometry of the geologic structure and topography act to amplify signals beyond what is prescribed by velocity variations. For example, a sharper contrast of amplitudes across the Newport-Inglewood Fault at 0.67 Hz and 1.0 Hz suggests that the depth and shape of the structure both play a role. Both the 0.67 Hz and 1 Hz maps also show amplification correlating with local topography, notably Signal Hill at the center of the array, where the surface expression of the fault trace is broken. A stronger east-west trend of amplifications observed in the 2.0 Hz map suggest that the short-period, shallow waves are less sensitive to deeper fault structure and instead are more sensitive to surface properties of the sedimentary alluvium, such as compaction, cohesive strength, or water content, all of which relate to the shear modulus of the material. In fact, because velocity and site amplification are two independent observables, they can potentially also be used to constrain other properties such as density structure [*Lin et al.*, 2012].

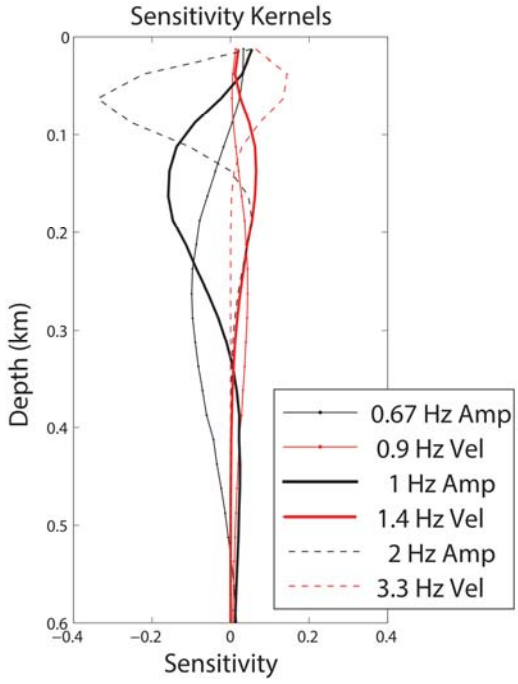

Figure 3.5: Depth sensitivity kernels for each of the three relative site amplification factors and the three phase velocity maps shown in Figure 4. Note that while the frequencies are different between the site amplification and phase velocity maps compared in Figure 3.1 (e.g., 1 Hz site amplification and 1.4 Hz phase velocity), they are selected such that they probe similar shear wave velocity structure with depth.

Variations in site amplification of this magnitude are expected from earthquake and nuclear testing event observations, such as those by *Rogers et al.* [1979], where peak ground velocity ratios as large as 7 in the Long Beach area are observed. The observed pattern of lower amplifications to the northeast are also observed by *Hauksson et al.* [2008] from the 2008 Chino Hills earthquake. Borehole measurements indicate that our region of low amplifications to the northeast are also characterized by higher clay-silt ratios, thicker Quaternary sediments, and a deeper water table [*Rogers et al.*, 1979]. Modeling by *Saikia et al.* [1994] of seismic data suggest that the variations in sediment thickness act as waveguides which dominate site amplification terms. Also, both observations and theoretical work [e.g., *Sánchez-Sesma and Campillo*, 1991; *Bouchon et al.*, 1996; *Hestholm et al.*, 2006] point out the strong effect of local topography on the amplification and trapping of surface waves. All of these studies illustrate the fact that complex wave propagation interactions are needed to explain observed site amplifications; simple comparisons to velocities or rock types may not be sufficient. High-resolution observations such as provided in this study, which require no assumptions about the structure at depth, are critical for further understanding and modeling of these effects.

We have demonstrated that ambient noise tomography can be used to map site amplification at high frequencies in the range 0.67 to 2.0 Hz. Dense arrays, like in Long Beach, CA, open a new opportunity for array processing techniques such as wavefront tracking, but special care is required to preserve relative information across the array. Ambient noise cross correlations in this Long Beach array have a very uneven distribution of noise sources, and their amplitudes would be misinterpreted if used as direct Green's Functions for ground motions. The wavefront tracking approach overcomes this issue by measuring wavefield gradients across the array, regardless of incoming amplitude distributions, and successfully recovers patterns of amplification that are expected from local geology and previous phase velocity observations. Specifically, we find a sharp contrast across the Newport-Inglewood Fault, and generally higher amplitudes to the Southwest of the city. The wavefront tracking approach also yields new information on attenuation and scattering, and offers the potential

of spatially resolving these terms if the ambient noise field is omnidirectional enough. These terms are derived from direct observations and are well suited to validate the simulations or modeling that might traditionally be used to estimate such amplifications. Complex interactions of waves moving through the very heterogeneous shallow crust will undoubtedly amplify seismic amplitudes, and direct observations of these effects are the first step toward improving future seismic hazard estimates.

3.6 Acknowledgments and Data

The authors gratefully acknowledge Dan Hollis at NodalSeismic LLC, and Signal Hill Petroleum, Inc., for permitting us to use the Long Beach data. We thank Dunzhu Li for scrips and advice in handling the larg quantity of cross correlations, and Rob Clayton and Asaf Inbal for helpful discussion. We are also thankful for the constructive and helpful comments from Jesse Lawrence and an anonymous reviewer. This project is supported by NSF grants EAR-1252191, EAR-1214912, and CyberSEES-1442665. Fan-Chi Lin also acknowledges the financial support from Signal Hill Petroleum for this research.

3.7 References

Abrahamson, N. A., and K. M. Shedlock (1997), Overview, *Seismol. Res. Lett.*, *68*(1), 9–23, doi:10.1785/gssrl.68.1.9

Bensen, G. D., M. H. Ritzwoller, M. P. Barmin, A. L. Levshin, F.-C. Lin, M. P. Moschetti, N. M. Shapiro, and Y. Yang (2007), Processing seismic ambient noise data to obtain reliable broad-band surface wave dispersion measurements, *Geophys. J. Int.*, *169*(3), 1239–1260, doi:10.1111/j.1365-246X.2007.03374.x.

Bouchon, M., C. A. Schultz, and M. N. Toksöz (1996), Effect of three-dimensional topography on seismic motion, *J. Geophys. Res.*, *101*(B3), 5835–5846, doi:10.1029/95JB02629.

Cua, G., and T. Heaton (2012), Characterizing average properties of southern California ground motion amplitudes and envelopes, *Bull. Seismol. Soc. Am.*, 1–67.

Denolle, M. A., E. M. Dunham, G. A. Prieto, and G. C. Beroza (2014), Strong ground motion prediction using virtual earthquakes, *Science*, *343*(6169), 399–403, doi:10.1126/science.1245678.

Graves, R., et al. (2010), CyberShake: A physics-based seismic hazard model for Southern California, *Pure Appl. Geophys.*, *168*(3–4), 367–381, doi:10.1007/s00024-010-0161-6.

Hauksson, E., K. Felzer, D. Given, M. Giveon, S. Hough, K. Hutton, H. Kanamori, V. Sevilgen, S. Wei, and A. Yong (2008), Preliminary report on the 29 July 2008 Mw 5.4 Chino Hills, eastern Los Angeles basin, California, earthquake sequence, *Seismol. Res. Lett.*, *79*(6), 855–866.

Hestholm, S., M. Moran, S. Ketcham, T. Anderson, M. Dillen, and G. McMechan (2006), Effects of free-surface topography on moving-seismic-source modeling, *Geophysics*, *71*(6), T159–T166.

Kohler, M. D., P. M. Davis, and E. Safak (2005), Earthquake and ambient vibration monitoring of the steel-frame UCLA factor building, *Earthquake Spectra*, *21*(3), 715–736, doi:10.1193/1.1946707.

Lin, F.-C., M. H. Ritzwoller, and W. Shen (2011), On the reliability of attenuation measurements from ambient noise cross-correlations, *Geophys. Res. Lett.*, *38*, L11303, doi:10.1029/2011GL047366.

Lin, F.-C., V. C. Tsai, and M. H. Ritzwoller (2012), The local amplification of surface waves: A new observable to constrain elastic velocities, density, and anelastic attenuation, *J. Geophys. Res.*, *117*, B06302, doi:10.1029/2012JB009208.

Lin, F.-C., D. Li, R. W. Clayton, and D. Hollis (2013), High-resolution 3D shallow crustal structure in Long Beach, California: Application of ambient noise tomography on a dense seismic array, *Geophysics*, *78*(4), Q45–Q56, doi:10.1190/geo2012-0453.1.

Prieto, G. A., and G. C. Beroza (2008), Earthquake ground motion prediction using the ambient seismic field, *Geophys. Res. Lett.*, *35*, L14304, doi:10.1029/2008GL034428.

Rogers, A. M., J. C. Tinsley, W. W. Hays, and K. W. King (1979), Evaluation of the relation between near-surface geological units and ground response in the vicinity of Long Beach, California, *Bull. Seismol. Soc. Am.*, *69*(5), 1603–1622.

Saikia, C. K., D. S. Dreger, and D. V. Helmberger (1994), Modeling of energy amplification recorded within greater Los Angeles using irregular structure, *Bull. Seismol. Soc. Am.*, *84*(1), 47–61.

Sánchez-Sesma, F. J., and M. Campillo (1991), Diffraction of P, SV, and Rayleigh waves by topographic features: A boundary integral formulation, *Bull. Seismol. Soc. Am.*, *81*(6), 2234–2253.

Shapiro, N. M. (2004), Emergence of broadband Rayleigh waves from correlations of the ambient seismic noise, *Geophys. Res. Lett.*, *31*, L07614, doi:10.1029/2004GL019491.

Snieder, R. (2004), Extracting the Green's function from the correlation of coda waves: A derivation based on stationary phase, *Phys. Rev. E: Stat. Nonlinear Soft Matter Phys.*, *69*(4), 046610, doi:10.1103/PhysRevE.69.046610.

Tsai, V. C. (2011), Understanding the amplitudes of noise correlation measurements, *J. Geophys. Res*, *116*, B09311, doi:10.1029/2011JB008483.

Weaver, R. L. (2010), Equipartition and retrieval of Green's function, *Earthquake Sci.*, *23*(5), 397–402, doi:10.1007/s11589-010-0738-2.

Weaver, R. L. (2011), On the retrieval of attenuation from the azimuthally averaged coherency of a diffuse field, *Comptes Rendus - Geosci.*, *343*, 615–622.

Zhang, J., and X. Yang (2013), Extracting surface wave attenuation from seismic noise using correlation of the coda of correlation, *J. Geophys. Res. Solid Earth*, *118*, 2191–2205, doi:10.1002/jgrb.50186.

Chapter 4

AMPLIFICATION AND ATTENUATION ACROSS USARRAY USING AMBIENT NOISE WAVEFRONT TRACKING

Bowden, D. C., Tsai, V. C., & Lin, F.-C. (2017). Amplification and Attenuation across USArray using Ambient Noise Wavefront Tracking. *Journal of Geophysical Research: Solid Earth*, (2012), 1–16. https://doi.org/10.1002/2017JB014804

4.1 Abstract

As seismic travel-time tomography continues to be refined using data from the vast USArray dataset, it is advantageous to also exploit the amplitude information carried by seismic waves. We use ambient noise cross correlation to make observations of surface-wave amplification and attenuation at shorter periods (8 – 32 seconds) than can be observed with only traditional teleseismic earthquake sources. We show that the wavefront tracking approach of [*F.-C. Lin, Tsai, & Ritzwoller,* 2012]can be successfully applied to ambient noise correlations, yielding results quite similar to those from earthquake observations at periods of overlap. This consistency indicates that the wavefront tracking approach is viable for use with ambient noise correlations, despite concerns regarding the inhomogeneous and unknown distribution of noise sources. The resulting amplification and attenuation maps correlate well with known tectonic and crustal structure; at the shortest periods, our amplification and attenuation maps correlate well with surface geology and known sedimentary basins, while our longest period amplitudes are controlled by crustal thickness and begin to probe upper mantle materials. These amplification and attenuation observations are sensitive to crustal materials in different ways than travel-time observations and may be used to better constrain temperature or density variations. We also value them as an independent means of describing the lateral variability of observed Rayleigh-wave amplitudes without the need for 3D tomographic inversions.

4.2 Introduction

Since the introduction of the Earthscope USArray, a network of more than 1700 stations spanning the continental U.S., numerous studies have imaged seismic velocities in the crust and upper mantle [e.g., *Shen et al.*, 2013; *Ekström*, 2014; *Porritt et al.*, 2014]. This has provided an unprecedented and cohesive view of tectonic structures within the continental US, ranging from broad patterns such as the transition from the recently tectonically active western US to stable continental craton in the east, down to the description of smaller scale provinces and features such as the Snake River Plain, Colorado Plateau, Reelfoot Rift and others. The seismic models have been constructed (and are continuing to be constructed) through a range of seismic methods including surface wave tomography (one-station, two-station and array-based methods [e.g., *Liang*, 2013; *Jin and Gaherty*, 2015]), body-wave tomography [e.g., *Schmandt and Lin*, 2014], receiver functions [e.g., *Kumar et al.*, 2012], and more, allowing for characterization of the shallowest crust down to the upper mantle.

While most of the above mentioned studies have focused on travel times and velocity modeling, there remains a wealth of information carried by the amplitudes of seismic waves [e.g., *Dalton and Ekström*, 2006a; *Ferreira and Woodhouse*, 2007; *Prieto et al.*, 2011; *Weaver*, 2011a]. Notably, *Lin et al.* [2012a] and later *Bao et al.* [2016] successfully developed and applied a wavefront tracking method by which the effects of attenuation or amplification can be measured as Rayleigh waves from distant earthquakes propagate across the array. This approach considers how local geological structure can affect a passing wave's amplitudes in a manner both observable and different than what can be described purely by velocities. For example, material properties such as temperature or fluid content may be distinguishable using the complementary information of both seismic velocity and attenuation [e.g., *Karato*, 1993; *Dalton and Ekström*, 2006; *Priestley and McKenzie*, 2006]. Additionally, different seismic observables will be sensitive to geologic structure at different depths; the sensitivity kernels of Rayleigh-wave amplification, horizontal-to-vertical (H/V) amplitude ratios, and group and phase velocity can all be used to probe different depths within the Earth [*Lin et al.*, 2012a, 2012b, 2014].

The wavefront tracking approach used by *Lin et al.* [2012a] and *Bao et al.* [2016] extracts amplitude and phase travel-time observations of Rayleigh waves from distant earthquakes. *Eddy and Ekström* [2014] used a somewhat different method based on amplitude differences between nearby stations to constrain amplifications, but this work also used earthquake data from USArray. In this paper, we use a wavefront tracking approach applied instead to ambient noise cross correlations. Ambient noise tomography has been increasingly used to recover velocity models, in part due to its flexibility in deployment (signals can be extracted anywhere two stations are present) and due to the fact that it can recover shorter wavelength surface waves than are observed with distant earthquakes. While the earthquake-based work of *Lin et al.* [2012a] recovered signals at periods in the range 24 to 100 seconds, the ambient noise signals extracted in this paper are in the range of 8 to 32 seconds, allowing crustal properties to be probed at both shallower ranges and higher resolution.

We favor the wavefront tracking method for two reasons. The first reason is that it properly accounts for energy focusing and defocusing, which may be a significant contribution to differences in observed amplitudes. Secondly, and important uniquely for the ambient noise data used in this paper, we prefer the method because the interpretation and use of raw amplitude information from the ambient noise wavefield has been a topic of some debate. Analytic work [e.g., *Tsai*, 2011; *Weaver*, 2011a], numerical simulations [e.g., *Cupillard and Capdeville*, 2010] and observations [e.g., *Ermert et al.*, 2016] all point to the fact that the amplitudes of noise correlation functions (NCFs) are highly dependent on the distribution of noise sources. As *Snieder* [2004], *Tsai* [2010] and others show, the waveform recovered by noise correlation will be a true and accurate Green's function between the two stations if and only if the background noise field is equally partitioned in time, space, frequency and mode. This constraint is obviously not met in the real earth, where dominant noise sources are strongly related to water-wave interactions in the oceans [i.e., *Longuet-Higgins*, 1950].

Various signal processing techniques may be employed to mitigate these non-stationary biases [e.g., *Bensen et al.*, 2007] but many such techniques unfortunately leave an NCF signal arbitrarily normalized, hindering the ability to make relative amplitude measurements. Further, such processing affects the sensitivity kernels of an NCF [i.e., *Fichtner et al.*, 2016], making it difficult to properly attribute the effect of such processing without complete knowledge of the background noise field. The full-waveform interferometry described by *Fichtner et al.* [2016] may offer an approach which can simultaneously describe both sources and structures, but this is difficult to apply in practice since solving for the full 3D ambient noise source distribution is a highly underdetermined inverse problem. By all accounts of ambient noise theory, the raw amplitude of an NCF should not be trusted to give reliable measures of structure alone.

Despite these theoretical problems with amplitude measurements, other studies have advocated that use of raw NCF waveforms is acceptable in some cases. *Prieto et al.* [2009] and *Lawrence and Prieto* [2011] were able to recover reasonable attenuation measurements from the western US by measuring waveform coherency, and in separate work argue that any directional source biases are negligible [i.e., *Lawrence et al.*, 2013], especially for a method where measurements can be averaged over a wide range of station-station azimuths. Additionally, scattering from crustal heterogeneities is expected to redistribute energy and mitigate some of these biases, especially at shorter wavelengths [e.g., *Campillo and Paul*, 2003; *Prieto et al.*, 2011]. However, we reemphasize that the validity of all of these arguments is debated by *Tsai* [2011], *Weaver* [2011b], and *Menon et al.* [2014].

As a separate example, amplitudes of NCFs are used by *Denolle et al.* [2014] and *Viens et al.* [2016] to recover realistic basin amplification effects and are well validated with actual earthquake events. In such virtual source reconstructions, the authors are careful to only consider station-station paths over a narrow range of azimuths and are careful to stack all NCFs over a consistent time period, thus mitigating potential biases from inhomogeneous noise source distributions. *Viens et al.* [2017] also demonstrates that while temporal and

azimuthal variations in noise source may contribute to variability in NCF amplitudes, such errors are small compared to the large effect of sedimentary-basin amplifications they observe, indicating that direct observation can still be useful in some contexts.

In contrast to the above mentioned approaches, the wavefront tracking method is only concerned with how a wavefield evolves across an array; the initial distribution of seismic energy is not important. This approach has been successfully used with eikonal, Helmholtz and amplification tomography [i.e., *Lin et al.*, 2009, 2012a; *Lin and Ritzwoller*, 2011]. If one considers all NCF pairs with a given station in common and all treated with identical and linear preprocessing, the resulting wavefield will evolve with time obeying the linear wave equation [*Lin et al.,* 2013]. This wavefield need not be composed of true Green's functions, and although we often refer to the single common station as a "virtual source," wave energy does not and need not originate from this point. Rather, the cross-correlation operation supplies a means to collect and observe wavefronts which can be used in the wavefront-tracking approach. This was the basis of similar work using ambient noise signals from a very dense array in Long Beach, CA to recover surface-wave site amplification effects at frequencies up to 1-2 Hz [i.e., *Bowden et al.*, 2015].

This paper explores the extent to which noise amplitude information can be recovered in a wavefront tracking scheme from USArray with the strictest possible processing. Steps are taken (explained below) to ensure a relatively high signal-to-noise ratio (SNR), while treating all stations equally and making measurements only when stations can be stacked for an identical period of time. We note that the resulting surface-wave amplification and attenuation maps have implications for tectonic structure and may be used in future tomographic efforts that include joint inversion of multiple datasets, though we also consider it an advantage that these properties may be directly observed without the need for complex 3D inversions or other assumptions.

4.3 Methods

4.3.1. Ambient Noise Cross Correlations

In processing the ambient noise cross correlations, we use vertical component data from 1,901 stations between 2007 and 2014 from USArray and supplemented by ANSS and regional networks, shown in Figure 4.1. We divide data into day-long segments of time, with the same preprocessing approach as in *Bowden et al.* [2015]. This uses a modification of traditional spectral whitening [i.e., *Bensen et al.*, 2007] that weights the spectra of all stations for a given day by a single, representative spectrum constructed by taking the 95th percentile at each frequency for all station spectra on that day, and this single spectrum is subsequently smoothed. Similarly, a version of time-domain weighting is used that scales the amplitudes of all resulting NCFs from a single day by a single, common factor before including each in a cumulative monthly stack, determined by taking the 95th percentile of the peak amplitudes of all NCFs. In this way, a set of spurious measurements from a day biased by earthquakes would not be more strongly weighted than any other day. These "whole-array" processing steps are not as effective as traditional pre-processing techniques at producing clear arrivals [i.e., *Bensen et al.*, 2007], but they do ensure that relative amplitude information is preserved and the wave equation still holds [e.g., *Lin et al.*, 2013]. The more traditional versions of spectral whitening or time-domain normalization act on each station individually, resulting in waveforms which are arbitrarily normalized relative to one another, and should not be applied when amplitudes are of interest. An alternative approach would simply be to not use any pre-processing whatsoever, but we find the SNR of our measurements are too poor in this case (such that the NCFs do not converge fast enough).

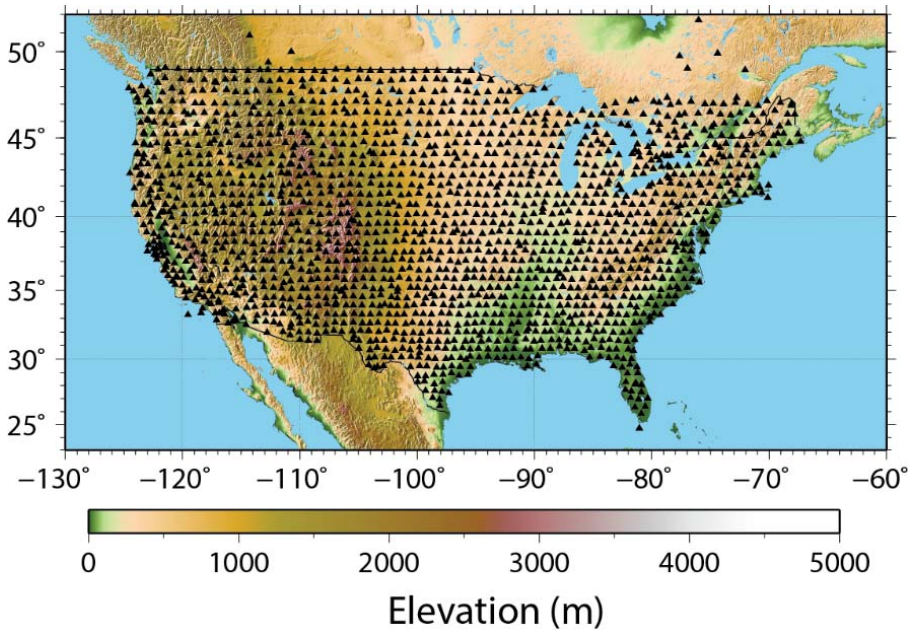

Figure 4.1: Stations used for ambient noise cross-correlation.

Stations in USArray were rolled across the U.S. from west to east between 2004 and 2014. At any given time, a smaller number of stations were concurrently recording (each station was in the ground for roughly 18 months), and most of these were focused over a narrow range of longitudes. This poses an additional difficulty in preserving relative amplitude information: we are only able to directly compare amplitudes of station pairs that were stacked over an identical time window. To account for this, we divide the continental U.S. into 1,115 sub-regions of roughly 600 km by 600 km in size, evenly distributed with significant overlap (up to 85% of a subregion overlaps with neighbors for the interior of the US). This size is somewhat arbitrary, but we find that a 600 km wide subregion from USArray generally has stations in the ground simultaneously for a reasonable period of time. A wavefield across each subregion is constructed using cross-correlations from all stations within a given subregion against any possible virtual source (i.e., any station), with the NCFs stacked for an identical number of months. Stations within the subregion are also counted as possible virtual sources. An example of one such subregion is shown in Figs. 4.2a and 4.2b, and we note that while the time period of months used for the NCFs in Fig. 4.2a are different

than those in Fig. 4.2b, within each set of observations the months used for stacking remains consistent.

Also, because stations are occasionally missing short periods of data, we do allow a station which was online for 90% of a given month to still be considered complete in regards to this stacking (though each station is properly weighted by the number of days it was present). On average, we are able to stack each station-to-subregion set for 3 months, though in some cases the stations were arranged such that more than a year's worth of data could be collected and consistently stacked. This difference in stacking durations makes for vastly different signal-to-noise ratios (SNR) in the recovered NCF waveforms, but we are careful to reject any NCF with an SNR less than 6, defined as the peak amplitude within the expected surface-wave arrival window to the RMS of the trace outside of the expected arrival window.

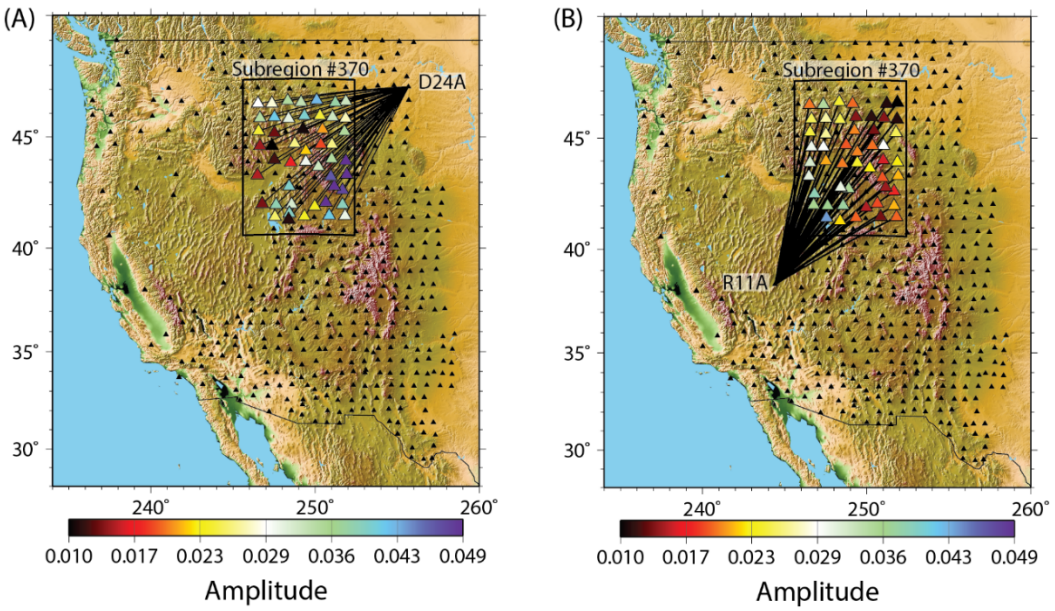

Figure 4.2: One example subregion or subset of stations. A given external virtual noise source must be stacked over an identical period of time, though this time period may be different for each external virtual noise source (black triangles). Panel (A) uses D24A as the virtual source whereas panel (B) uses R11A as the virtual source.

This process of subdividing the array into many subregions could, in theory, introduce some amount of spatial bias or aliasing due to the overlapping nature of subregions. However, if a given location in the area is sampled by multiple overlapping regions, this simply means that more observations of the wavefront are available (as explained in more detail below). In our final measurements, we observe no bias or pattern resembling the initial distribution of subregions, and so are confident that this is not an issue. Unfortunately, much of the potential data is discarded in this strict stacking procedure, but this is preferable to dealing with the unknown effects of stacking over uneven time windows.

4.3.2 Wavefront Tracking Across a Given Subarray

Once noise correlations are complete, we can proceed with the wavefront tracking approach of *Lin et al.* [2012a], in a manner which is (nearly) independent of the wavefield source or type. The method considers the amplitude, $A(x, y)$, and phase travel time, $\tau(x, y)$, of an assumed 2D surface wavefield at a given period -- in this case the vertical component of Rayleigh waves at numerous locations throughout a given sub-array, extracted from waveforms with standard frequency-time analysis (FTAN) [i.e., *Levshin and Ritzwoller*, 2001]. Fundamental-mode Rayleigh waves are isolated by the analysis' requirement that a clear dispersion branch is observed, and by requiring a signal-to-noise ratio of the arrival compared to other signals of at least 6. It is assumed that there is only one observed wavefront originating at the virtual source station. The amplitudes (for example from Figs. 4.2a and 4.2b) and travel times are used to construct maps of $A(x, y)$ and $\tau(x, y)$ by fitting a surface onto a fine, regularly spaced grid with spacing of 0.2 degrees latitude and longitude. This surface-fitting procedure is done using the minimum-curvature surface subroutine of GMT [*Wessel et al.*, 2013], and is usually quite successful at describing the evolution of a wavefield as long as the wavelength used is not shorter than the average station spacing. Automated quality control checks are used to correct for a 2π ambiguity in measuring phase velocity.

As described by *Lin et al.* [2012a], surface waves in 3D can be described at the Earth's surface by 2D surface-wave potentials as long as lateral velocity variations are relatively smooth. The potential $\chi_{2D}(x, y, t)$, in this case for the vertical component of Rayleigh waves, is related to observed amplitudes of the wavefield, $A(x, y)$, by

$$A(x,y)e^{i\omega(t-\tau(x,y))} = \beta(x,y)\chi_{2D}(x,y,t) \qquad \text{Eq. 4.1}$$

where $\beta(x, y)$ is a local, relative amplification term for surface-wave potentials (discussed more below). This potential satisfies the 2D wave equation [e.g., *Tromp and Dahlen*, 1992], which leads to the following equation, also sometimes referred to as the transport equation,

$$\frac{2\nabla\beta \cdot \nabla\tau}{\beta} - \frac{2\alpha}{c} + S = \frac{2\nabla A \cdot \nabla\tau}{A} + \nabla^2\tau \qquad \text{Eq. 4.2}$$

where α relates to attenuation and c is phase velocity. All variables in Eq. 4.2 have a spatial dependence on (x, y), but this is omitted in Eq. 4.2 (and most of the paper) for brevity. The term α refers to intrinsic attenuation and relates to the more commonly used Q factor by $\alpha = \pi f/(UQ)$ where f is frequency and U is group velocity [e.g., *Mitchell*, 1995; *Yang and Forsyth*, 2008], and attenuation is assumed weak enough to not affect phase travel time. Compared to the derivation of *Lin et al.* [2012a] and following *Bowden et al.* [2015], we use a more general solution in which a generic source term, $S(x, y)$, is included and described later.

Equation 2 tracks changes in amplitude as the Rayleigh wave propagates from one region to another. It is arranged in such a way that the right-hand side consists entirely of observables A and τ. Qualitatively, Eq. 4.2 can be described in the following way: observations of spatial amplitude changes in the direction of wave propagation ($\nabla A \cdot \nabla\tau$) are corrected by the amplitude changes associated with the wavefront's changing shape and velocity, including geometric spreading, wavefront focusing, and a shift in wavelength from one medium to another (all captured by the $\nabla^2\tau$ term). Following *Lin et al.* [2012a], this sum on the right hand side is referred to as "corrected amplitude decay," and such maps are collected for each

virtual source available to each subregion at a range of discrete periods, from 8 to 32 seconds. The sum of these two terms on the right-hand side would be zero in the absence of geologic variations causing amplification, attenuation or additional seismic sources (all pieces of the left-hand side). These three terms can be further decoupled by noting that the amplification caused by underlying geologic structure will depend on the direction of propagation ($\nabla\beta \cdot \nabla\tau$), while attenuation or simple sources will act on a wavefront isotropically.

Here, we use observations of A and τ that are specifically for a single period of the vertical component of fundamental-mode Rayleigh waves. This fundamental mode was selected and isolated in the frequency-time analysis used, but we note that the method could be applied to higher modes if these were well observed. To use horizontal-component Rayleigh or Love observations, an additional gradient or curl term, respectively, is needed to relate observed amplitude to the conserved surface-wave potential [*Tromp & Dahlen,* 1992]. This is feasible under the framework of this method, but it is not the focus of this paper.

For the amplification term, there are two possible ways to define and interpret this, and the difference is not well described in the literature. In Eq. 4.2, β refers to a surface-wave potential amplification factor that results from the wavefront tracking observations. This can be expressed as a ratio of measurements between a reference site (indicated by superscript R) and any other site of interest as

$$\beta = \left(\frac{\boldsymbol{cUI_0}}{\boldsymbol{c^R U^R {I_0}^R}} \right)^{-\frac{1}{2}} \qquad \text{Eq. 4.3}$$

where $\boldsymbol{c}$ is phase velocity, $\boldsymbol{U}$ is group velocity and $\boldsymbol{I_0}$ is an integral over the surface wave eigenfunctions [e.g., *Tromp and Dahlen*, 1992 and *Lin et al.*, 2012a]. For Rayleigh waves the I_0 integral is defined as

$$I_0 = \int_0^\infty \boldsymbol{\rho(z)(u_1(z)^2 + u_2(z)^2)dz} \qquad \text{Eq. 4.4}$$

where $\boldsymbol{\rho(z)}$ is the density as a function of depth, and $\boldsymbol{u_1(z)}$ and $\boldsymbol{u_2(z)}$ describe the normalized horizontal and vertical eigenfunctions, respectively. The ratio of phase velocities (c/c_R) in Eq. 4.3, specifically, is important because the $\nabla^2\tau$ term in Eq. 4.2 corrects for shifts in wavelength in addition to geometric spreading, focusing and defocusing of a wavefront. In this wavefront tracking approach, the $\nabla^2\tau$ term from Eq. 4.2 is necessary to account for 2D geometric effects in a proper finite-frequency theory. Presenting observations of β defined this way is the most natural for this work, and β is referred to as "observed amplification" throughout this paper.

However, since the amplification β is relative to the surface-wave potential, and the potential is not directly observable, it is not the appropriate amplification factor to directly describe observed surface-wave amplitudes. To properly describe changes in a surface wave's amplitude that will be observed due to site effects related to the local 1D geological structure, a different site-amplification factor [i.e., *De Noyer*, 1961; *Bowden and Tsai*, 2017; *Tsai et al.*, 2017] can be defined as

$$\frac{\boldsymbol{A_n}}{\boldsymbol{A_n}^{\boldsymbol{R}}} = \left(\frac{\boldsymbol{UI_0}}{\boldsymbol{U^R I_0}^{\boldsymbol{R}}}\right)^{-\frac{\mathbf{1}}{\mathbf{2}}} \qquad \text{Eq. 4.5}$$

where $\boldsymbol{A_n}$ and $\boldsymbol{A_n}^{\boldsymbol{R}}$ describe the amplitudes of a surface wave at a given site and reference site as a function of frequency, respectively. (Note that the difference between Eq. 4.5 and Eq. 4.3 is that Eq. 4.3 contains an extra phase velocity term.) This version of site amplification applies directly to the amplification of observed displacement amplitudes as a surface wave travels from one 1D profile to another, and therefore may be most useful for descriptions of site response for hazard purposes. This definition is also the more appropriate version of site amplification to use for methods such as that of *Eddy and Ekström* [2014] which rely on more direct observations of amplitude ratios without accounting for geometric focusing and defocusing of the wavefront. Again, we refer to β as defined in Eq. 4.3 as observed amplification for the wavefront tracking method [i.e., *Lin et al.*, 2012a; *Bao et al.*, 2016 and this work], but this difference should be kept in mind when interpreting the results.

Once the spatial gradients on the right-hand side of Eq. 4.2 have been measured, the corrected amplitude decay depends only on the direction of wave propagation and geologic structure, rather than any time-varying properties of the far-field ambient noise field. Thus, different azimuths of wave propagation may be compared even though the time range of data used may be different. Additionally, measurements from different subregions may now be collected for regions of overlap; all observations of corrected amplitude are treated equally, regardless of virtual source or subregion. Collecting observations in regions of overlap may lead to some redundancy of any given source-station pair, but we believe this has little effect on the resulting analysis. As in *Lin et al.* [2012a] and *Bao et al.* [2016], the corrected amplitude decay measurements are plotted as a function of azimuth and a sinusoidal curve is fit with 1-psi anisotropy (that is, exactly 360 degree periodicity but arbitrary phase, amplitude and static offset), as in Fig. 4.3. Once a 1-psi curve is fit, the magnitude and direction of peak amplification is attributed to the term $(2\nabla\beta \cdot \nabla\tau)/\beta$, while the static offset is attributed to the isotropic attenuation and source terms. This curve-fitting approach is also discussed and preferred by *Bao et al.* [2016] over an approach that measures attenuation and amplification through separate approaches. One example from near the Yellowstone Hotspot below (Fig. 4.3a) exhibits a high amount of directionally dependent amplification, while the other example from the Basin-and-Range Province (Fig. 4.3b) does not.

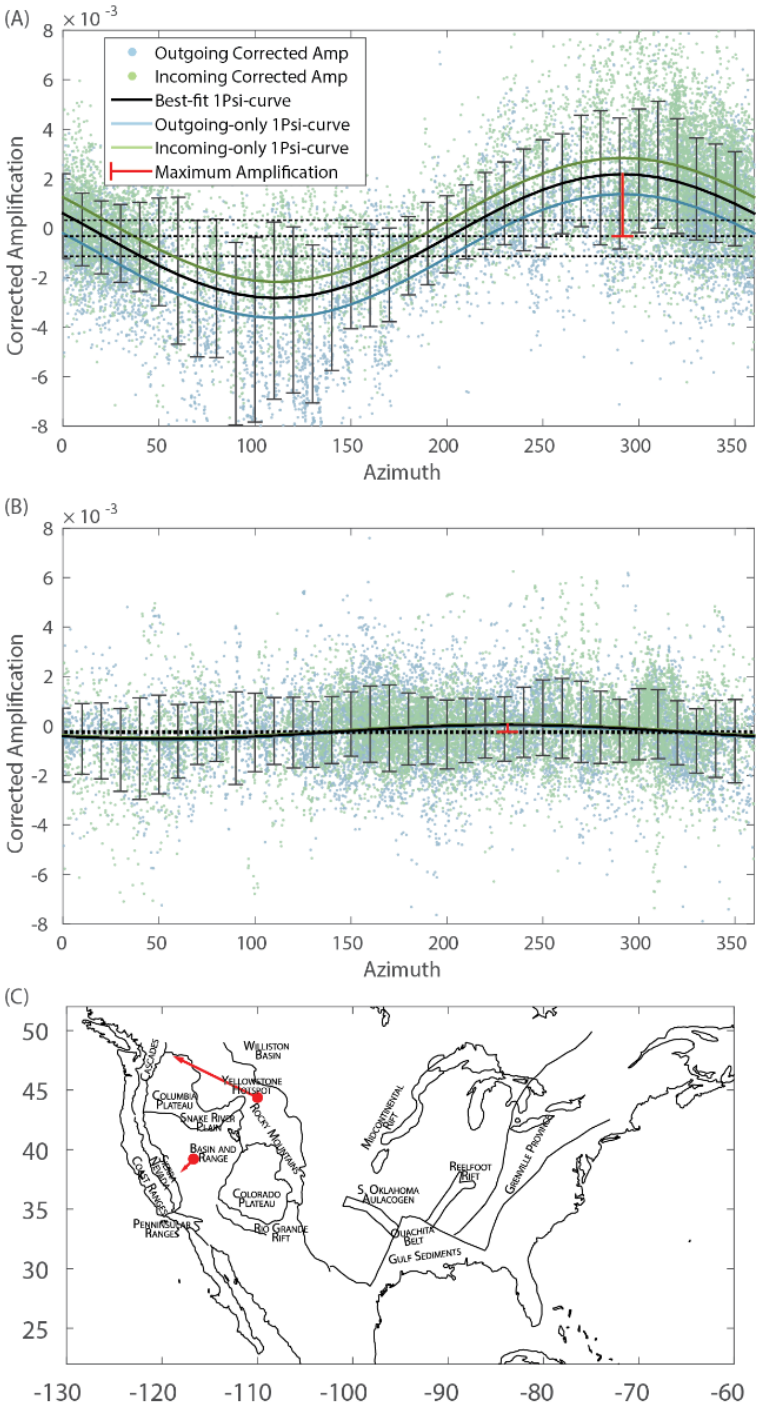

Figure 4.3: Example corrected amplification measurements as a function of propagation azimuth at 24 seconds period. Each green or blue dot represents the incoming or outgoing observation from a virtual source. One point exhibits strong amplitude effects and is near the Yellowstone Hotspot (A), and the other example point (B) in the relatively homogenous Basin-and-Range Province does not. For both

measurements, the location, magnitude and direction of the 1-psi curve is represented as a vector in the map view (C). Geologic and tectonic provinces referred to throughout the paper are labeled in the map (C).

We note that we keep the acausal (negative time-lag, inwardly propagating) and causal (positive time-lag, outwardly propagating) sides of the NCF separate to distinguish between the effect of attenuation and sources. New energy contributed to the system within a given subregion (referred to as S in Eq. 4.2), either from new ambient noise sources or energy scattered away from heterogeneities that act as new isotropically radiating sources [i.e., *Ma and Clayton*, 2014], will primarily only affect the acausal incoming wavefront [*Bowden et al.*, 2015; *Liu, Ben-zion, & Zigone,* 2015]. This is because the region of noise sources which most strongly contributes to the NCF is changing along with the incoming wavefront, while for the outgoing wavefront the influential noise sources are relatively fixed somewhere at or behind the virtual source. Because the positive-lag, outwardly propagating wavefront is assumed to be affected by attenuation only (and not sources), we extract our observations of attenuation from these measurements only. Comparing the incoming and outgoing wavefronts may yield constraints on sources and scatterers, but because we cannot distinguish between sources and scatterers we do not interpret these results here.

Because of this difference in causal and acausal time lags, we perform the 1-psi fits in three successive steps. For a first pass, both the causal and acausal corrected amplifications are considered together, and the best-fitting 1-psi amplitudes and directions are determined, allowing for variable amplification magnitude, direction and static offset (the black curves in Fig. 4.3a and 4.3b). Combining causal and acausal measurements is advantageous because some regions of the US exhibit very few measurements of one or the other (e.g., near the edges or coastlines), but using both allows for a more complete range of azimuthal observations and a more robust fit. With the amplification directions and magnitudes constrained and fixed, a second iteration is then performed to find the best-fitting static offsets separately for the causal and acausal waves. As described in the previous paragraph, our measurements of attenuation are derived only from the outgoing, causal wavefield.

Finally, these static offsets (dashed lines in Figs. 4.3A and 4.3B) are subtracted from each individual corrected amplification measurement (the blue and green dots in Figs. 4.3A and B) such that both incoming and outgoing wavefronts are unbiased by attenuation, scattering or sources, and then a final measurement of amplification direction and magnitude is made. All measurements at a given location are discarded if the mean chi-squared misfit measured at each of 18 different 20 degree azimuthal bins (shown in Fig S3.1) is greater than 0.1 (see Supporting Information), which was most often the case only at the edges of USArray. Areas with a high uncertainty within the interior of the array are also excluded, but these are generally small and effectively smoothed over in the process of fitting amplification measurements. Fig. 4.4 shows the lateral pattern of these best-fitting magnitudes and directions for 24-second Rayleigh waves.

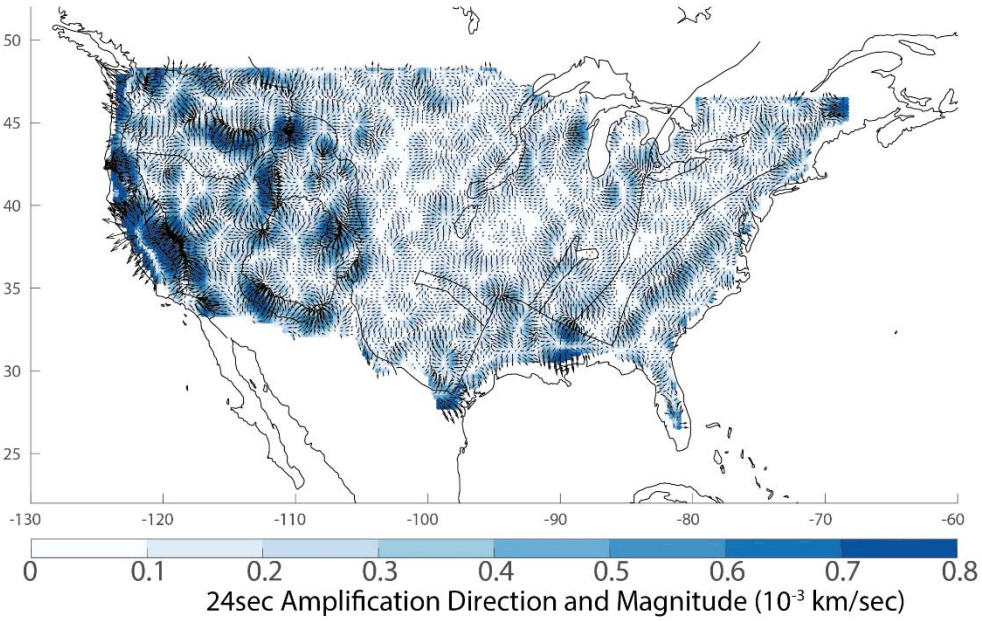

Figure 4.4: Map view of all 1-psi magnitudes and directions for 24-second Rayleigh waves. Stronger colors indicate a stronger gradient in observed amplitudes, which is expected to correlate with boundaries of geologic provinces.

Given maps like Fig. 4.4 at each discrete period, we can finally describe the observed amplification term, β. The vector field of maximum amplification magnitude and direction is attributed to the $2\nabla\beta \cdot \nabla\tau / \beta$ term in Eq. 4.2., and following *Lin et al.* [2012a], the best-fitting scalar amplification map, β, is determined through a linearized fit to the vector field. Unlike the work of *Lin et al.* [2012a], no successive iterations of the entire method is performed; one such iteration was tested but the change was negligible enough and the computational cost high enough that it was considered unnecessary. Finally, although most of this processing is performed on a regular grid of 0.2 degrees, we note that the actual resolution of attenuation and amplification depends on the original station spacing, and so features of all maps are smooth on the order of 100 km.

4.4 Results and Discussion

4.4.1.1 Amplification Maps

Final observed surface-wave amplification (β) maps are presented in Fig. 4.5, at periods of 8, 12, 16, 24 and 32 seconds. For each map, the reference value for β (i.e. β =1) is arbitrary and is taken simply as the point representing an average. Any map could be re-normalized and its colorbar shifted arbitrarily. As mentioned previously, this amplification is most appropriate for wavefront tracking approaches [e.g., *Lin et al.*, 2012a; *Bao et al.*, 2016], but maps of amplification β corrected for phase velocity may be most appropriate for direct amplitude observations [e.g., *Eddy and Ekström*, 2014], and these alternative site amplification factors based on Eq. 4.5 are presented in supplementary Figure S4.2.

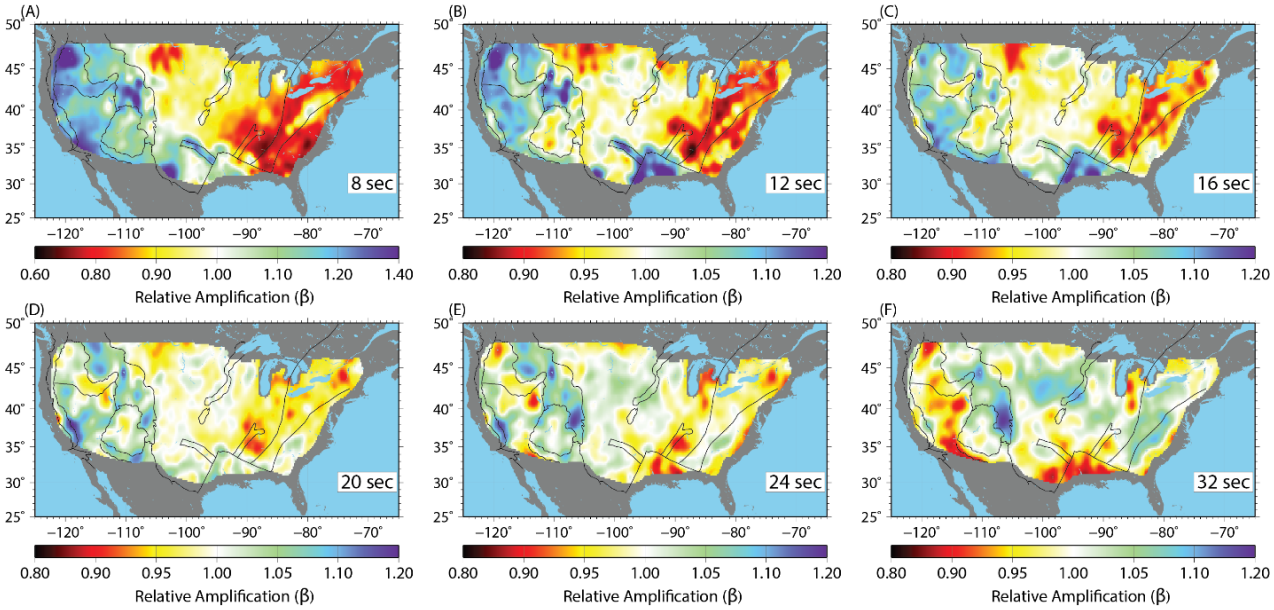

Figure 4.5: Amplification measurements (β) at a range of periods: 8, 12, 16, 20, 24 and 32 seconds (A-F). We note that all maps are plotted with a non-linear colorscale to emphasize differences closer to 1. Only the 8-second subpanel (A) is plotted with a different scale than the others.

As expected, the maps show significant correlation with known tectonic provinces such as the Snake River Plain, Colorado Plateau, Oklahoma Aulacogen and others (see tectonic province labels in Fig. 4.3c). Higher amplification is observed at almost all periods at the Yellowstone Hotspot, which is known to be warm and therefore have slower seismic waves [e.g., *Huang et al.,* 2015; *Seats & Lawrence,* 2014], resulting in amplification. At shorter periods (i.e., 8 and 12 seconds, Figs. 4.5a and 4.5b), the maps indicate strongest amplification in regions with known slow seismic velocities, primarily controlled by the presence of sediments such as in the Columbia Basin or in the Gulf of Mexico [e.g., *Mooney and Kaban*, 2010]. Indeed, to first order these maps are expected to correlate with seismic velocity; surface waves entering a low-velocity sedimentary basin will be slowed and amplified. In contrast, the older and faster stable craton in the eastern US, including the Trans-Hudson, Grenville and Appalachian Provinces, are associated with lower amplification, which is most obvious again at shorter periods (i.e., Figs. 4.5a and 4.5b).

There is a reversal of some of the dominant lateral features as observations are extended to longer period. While the shorter period observations mentioned above were sensitive to the top 10 km of crustal material, 32-second Rayleigh waves start to be sensitive to upper mantle material (Fig. 4.6e). Crust in regions such as the sedimentary basins in the Gulf of Mexico or regions thinned by tectonic activity such as the Basin-and-Range Province are significantly thinner, and so are the first to see higher mantle velocities and the correspondingly lower amplification. In contrast, areas with the thickest known crust, such as the Southern Rockies, remain as a region of high surface-wave amplification.

Figure 4.6 shows depth sensitivity kernels for various surface-wave observables, for an average representative 1D velocity profile for the continental U.S. from the tomography of *Schmandt et al.* [2015] (which will be further compared later), calculated by iteratively perturbing shear wave velocity, P wave velocity and density, and recording the resulting change in semi-analytic predictions (using Computer Programs in Seismology [i.e., *Herrmann*, 2013]). Standard relations from *Brocher* [2005] are used to infer Vp and density from the Vs profile shown. The amplification sensitivity kernels indicate that they are sensitive to a shallower region and with opposite sign for some depths as compared to phase or group velocity, and so care should be taken if these maps are to be compared to surface-wave velocity observations of other studies.

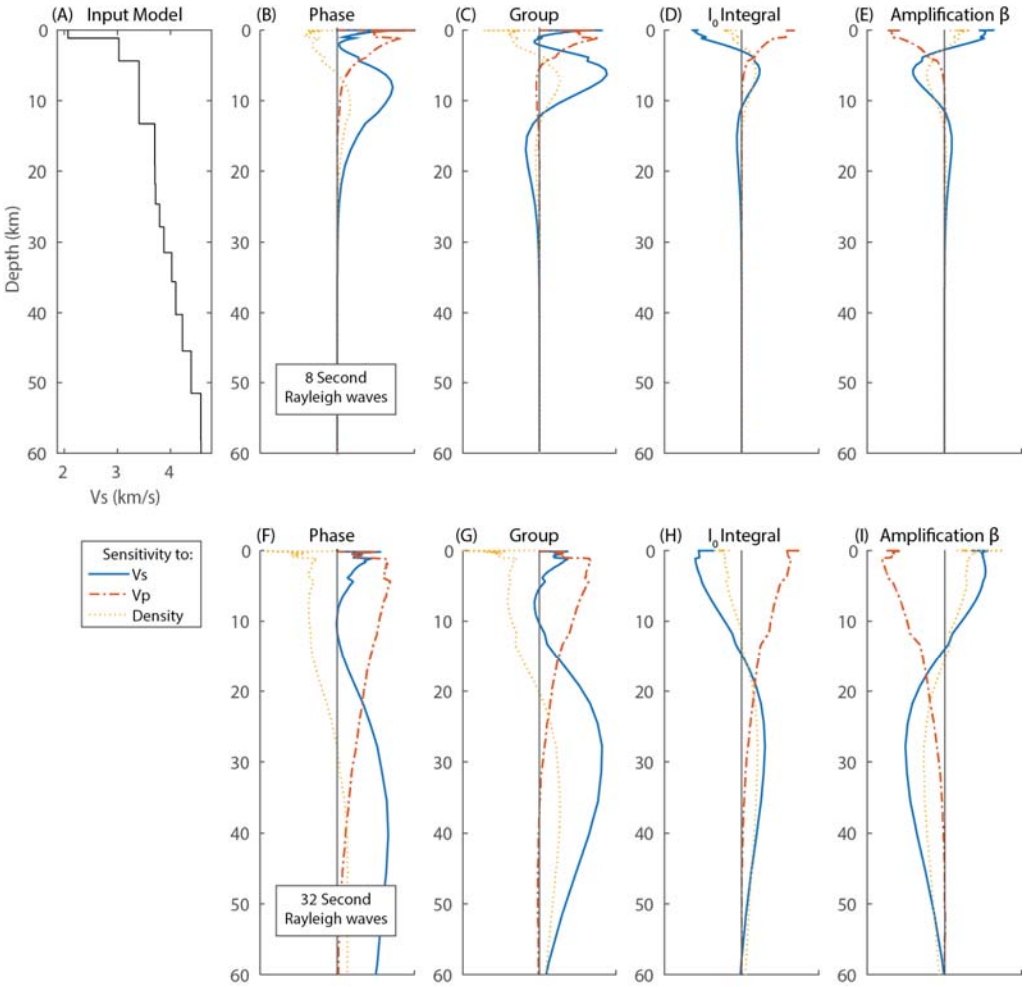

Figure 4.6: Sensitivity kernels for a representative 1D velocity profile (A) at 8 and 32 seconds. In each subpanel (B-I) sensitivity to Vs (solid blue line), Vp (red dashed line) and density (yellow dotted line) are indicated separately. The observed amplification sensitivity kernel is calculated using the phase velocity, group velocity and I_0 energy integral kernels, following Equation 4.3.

4.4.1.2 Amplification comparison to other models

We can compare the features of these maps to 3D models. *Schmandt et al.* [2015] has produced one such 3D model using a variety of observations, from both earthquake and ambient noise dispersion, H/V curves, and teleseismic receiver functions. At each point a 1D shear-wave velocity profile is considered, Vp and density are estimated based on standard

relations [i.e., *Brocher*, 2005], and β semi-analytically estimated using Eq. 4.3. Again the reference site is arbitrary and β =1 is defined as the whole-array average.

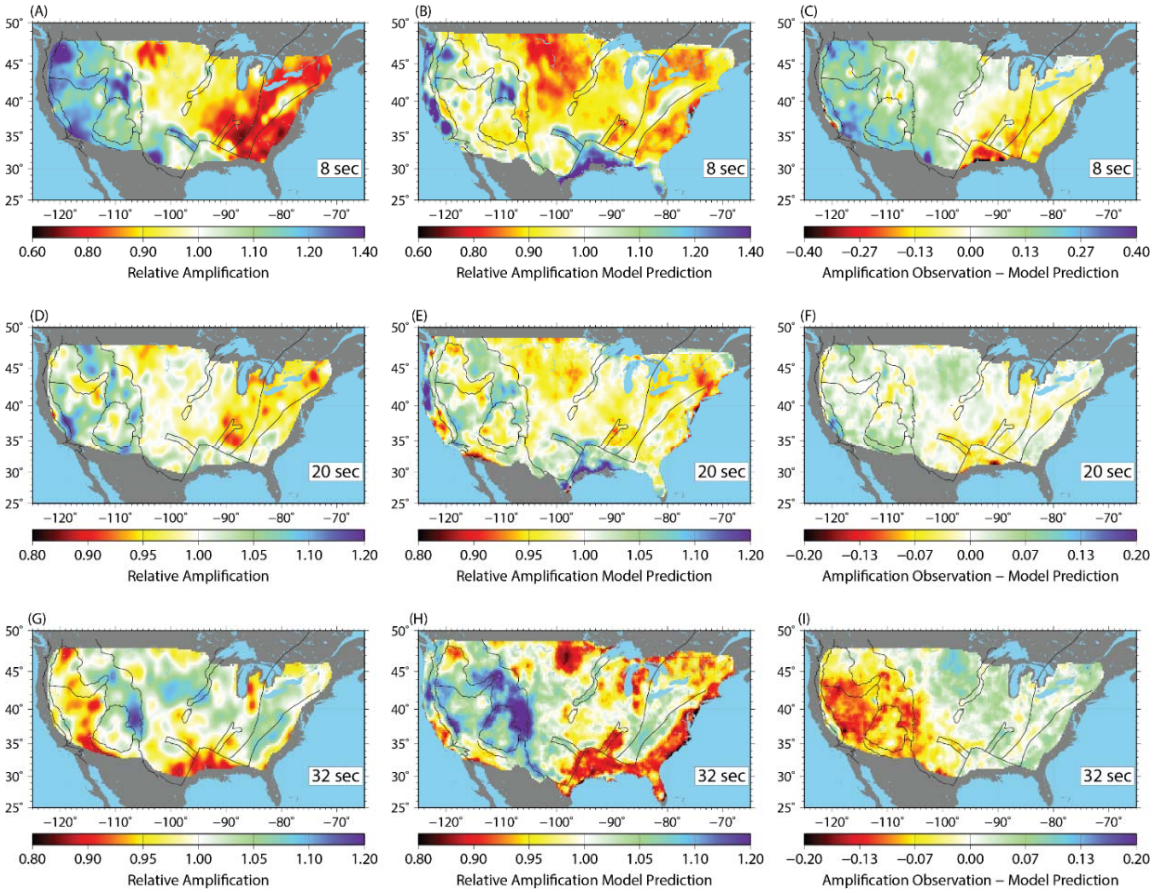

Figure 4.7: Comparison of our observations (A, D, G) to semi-analytic model predictions (B, E, H) and the difference of the two (C, F, I) for three different periods (8 s, 20 s, and 32 s, respectively).

In Fig. 4.7, our observed amplifications at 8, 20 and 32 seconds are presented again next to the theoretical model predictions using the model of *Schmandt et al.* [2015], as well as the difference between the two. Most of the dominant lateral features are present in both maps, as well as the overall magnitude of amplification response (i.e., plus or minus 20% in many regions). However, the difference maps indicate that there remain a number of regions with differences. The most severe of these differences is observed at 32 seconds, where it appears

that the model predicts significantly stronger amplifications in the western US (indicated by a negative residual in Fig. 4.7I.). This discrepancy could indicate an issue with the velocity and density model used. Though we cannot comment on the validity of the velocity model itself or the need for improvements, we note that our model predictions rely on standard relations between Vs and Vp, as well as Vs and density described by *Brocher* [2005]. These relations represent averages, and were likely not intended to unilaterally represent the various rheologies found throughout the continental U.S. Considering it is the 32 second maps which are most sensitive to mantle materials, and that mantle materials are likely not well represented by the same Vp, Vs and density relations used for the crust, we expect this is the primary reason for discrepancies between the model and our observations. Inaccuracies in the assumed Vs-Vp-density scalings may also explain differences in the shorter-period (8-s) map (Fig. 4.7C), in that prominent features here relate more to surface geology and shallow sedimentary basins such as in the Gulf Coast. Testing alternative relations, or even constraining and improving such relations, may be an opportunity of future work with these datasets.

As a different test, we can compare our noise-derived amplification observations to the earthquake-derived observations of *Lin et al.* [2012a] (Fig. 4.8). Again, Lin's previous work was focused on longer period measurements but at least measurements of 24 seconds and 32 seconds overlap. Here, we re-measured an average, reference point of amplification for the western US and rescale the relative amplifications shown in Figs. 4.8A, B, D and E for a clearer comparison once values are compared in Figs. 4.8C and F. In general, we find very good agreement, with any substantial differences only near the edges of our domain. Notably, the strong discrepancy that was present between observation and model at 32 seconds (Fig. 4.7I) throughout the western US is not as strong of an issue here. These similarities confirm that the ambient noise measurements do not provide different or biased information than would be inferred from earthquake wavefronts. However, it should be noted that the earthquake-based observations use similar processing and gradient measurements (i.e., Eq. 4.2) so any systematic biases in the method would appear in both maps.

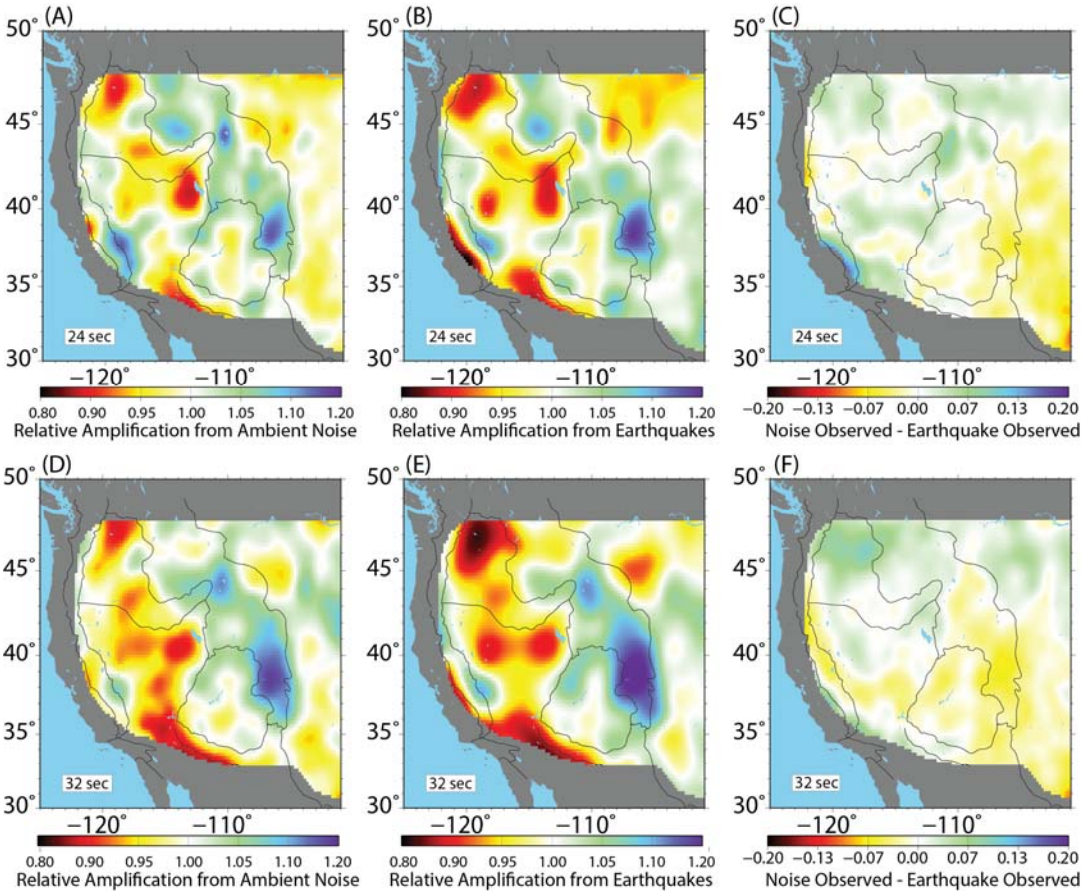

Figure 4.8: Our noise-derived observations of amplification (A and D), the earthquake-derived observations replotted from Lin [2012a](B and E), and the difference between the two (C and F) at 24 and 32 seconds. Relative amplifications in panels A, B, D and E have all been arbitrarily rescaled by the average value for this region of the western US.

We can also compare our observations to those of *Eddy and Ekström* [2014], who use earthquakes to observe amplitude ratios at adjacent stations. While their measurements focus on mostly longer periods (35 seconds to 125 seconds), their 35-second observations may be expected to correlate with our 32-second noise observations. Again, because their method relies on direct observation of surface wave amplitudes without a focusing and defocusing correction, a site amplification term defined as in Eq. 4.5 without phase velocity terms is most appropriate for comparison (see Fig. S3.2). Indeed, many lateral features are consistent,

with low amplification of ~0.9 in the Texas Gulf, and northern Basin and Range provinces, as well as high amplification of ~1.1 in the southern Rockies for both studies. The largest discrepancy is observed in the central northernmost part of the array at around -105W, 48N, where the 35-second map of *Eddy and Ekström* [2014] shows strong amplifications above 1.15 while our observations show little or no structure in this region.

4.4.2.1 Attenuation Maps

We also examine the level of intrinsic attenuation, indicated by a persistent loss of energy at a given location regardless of propagation direction (see Eq. 4.2). This is measured by a negative static offset of the 1-psi sine curve for outgoing waves. This static offset is attributed to the $-2\alpha/c$ term in Eq. 4.2, and again α can be related to a quality factor Q by $\alpha = \pi f/(CQ)$. As in the work of *Bao et al.* [2016] we find it necessary to smooth the maps of α using a Gaussian filter of roughly 100 km. Even though we could constrain site-specific phase and group velocities from our measurements, we use a constant phase and group velocity appropriate to the period (as determined by the representative profile in Fig. 4.6) so our observations are not complicated by different patterns of spatial variability in velocity structures. In any case, the attenuation we observe varies by nearly two orders of magnitude (plotted logarithmically in Fig. 4.8), and so including a slightly different phase or group velocity will not change the salient features in any significant way. The phase velocities used as a representative average are 2.99, 3.14, 3.27, 3.39, 3.50 and 3.67 km/s for each of the 6 periods, respectively, and group velocities are 2.67, 2.79, 2.85, 2.90, 2.97 and 3.19 km/s, respectively. Also, we remind the reader that these measurements are for Rayleigh-wave attenuation and may differ from observations of P, S or the commonly observed Lg phase, but relations for different Q observables have been discussed by *Mitchell et al.* [1976] and others.

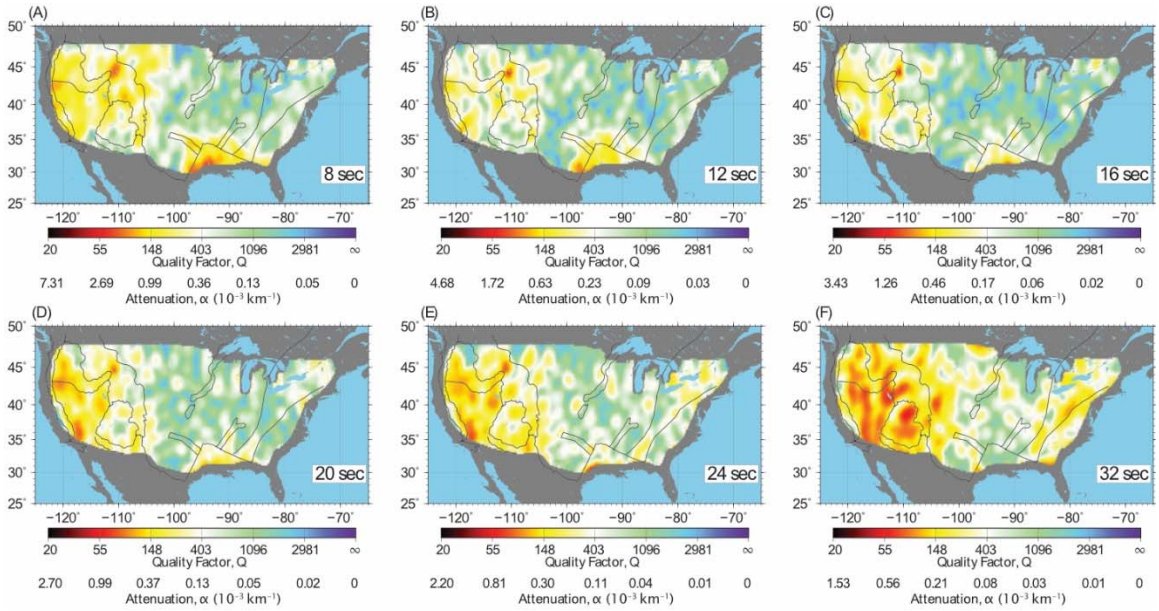

Figure 4.9: Attenuation observations at 6 different periods, again 8, 12, 16, 20, 24 and 32 seconds. In each plot a logarithmically spaced Q factor is indicated on the colorscale, though we also show the corresponding conversion to attenuation coefficient, α.

We observe that attenuation is somewhat high at the shortest period, 8 seconds (Fig. 4.9a), which is expected considering this is most sensitive to shallow crustal sedimentary basins. Even small scale features associated with sediment fill after rifting in the Oklahoma Aulacogen, mid-continental rift and Rio Grande rift can be observed (see tectonic province labels in Fig. 4.3c). At intermediate periods (i.e., 12-16 seconds, Figs. 4.9b and 4.9d) attenuation reaches its lowest values (highest Q) in most of the continental U.S., representative of deeper crustal material. At our longest periods (i.e., up to 32 seconds, Fig. 4.9f), attenuation increases again significantly, particularly in the western US, such as in the Basin and Range province, since these periods are now sensitive to upper mantle material. High attenuation in the Colorado Plateau and southern Rockies is unexpected, however, considering the crust should be quite thick in this region.

Throughout all periods, the Yellowstone Hotspot is prevalent as a region of high attenuation, relating to high temperatures in the magma chamber at depth (Huang et al., 2015). The high

attenuation at Yellowstone is also indicative that the methodology generally works as expected. A significant static offset in the 1-psi fits (as in Fig. 4.3a) is responsible for this reported attenuation; low velocities are expected and the corresponding high amplifications are observed, but these other factors do not cause the azimuthally-independent decrease in amplitude that we attribute to attenuation. As discussed by *Lin et al.* [2012a] and *Bao et al.* [2016] however, the focusing and defocusing effect as captured by $\nabla^2\tau$ may not be adequate on small spatial scales, and care must be taken when interpreting these results.

4.4.2.2 Attenuation Comparisons

Our maps can be compared to the earthquake-based attenuation maps of *Lin et al.* [2012a] and *Bao et al.* [2016]. The 30-second attenuation map of *Lin et al.* [2012a] shows similar large-scale structure to ours at 32 seconds, the Basin and Range province and the southern Rockies being the most prominent features. However, *Lin et al.* [2012a] smoothed their attenuation maps with a Gaussian filter of 4 degrees, much smoother than ours, and so further fine-scale comparisons are difficult. *Bao et al* [2016] present attenuation maps at periods down to 40 seconds, again using a similar wavefront tracking approach, though applied to earthquake observations. Our observations at 32 seconds correlate well in regards to dominant lateral features and values, such as the strong difference between the western and central US. More specific similarities also exist, such as the slightly higher attenuation on the eastern seaboard east of the Grenville Province, the well defined delineations of the Basin and Range Province and the Colorado Plateau, and even a small patch of higher attenuation east of the southern Rockies. Some differences exist, notably in that our observations indicate high attenuation in the Colorado Plateau not present in the maps of *Bao et al* [2016].

Our attenuation maps also correlate well with expectations based on temperature observations. For example, the SMU Geothermal Lab Heat Flow Map *[Blackwell et al.,* 2011] based on numerous well-log and geothermal power plant measurements indicate higher temperatures in the southern Rockies, Basin-and-Range Province, Yellowstone Magma Chamber and other places which agree with our attenuation maps at various periods,

but especially in the range of 16 to 24 seconds. This is not surprising, considering these periods are most sensitive to the greater bulk of the crust; shorter periods may be strongly controlled by shallow compositional differences (i.e., sedimentary basins) and longer periods will begin to be affected by mantle materials.

Our maps also correlate to some extent with those of *Lawrence and Prieto* [2011]. Their maps use a different method which has been much debated in the literature (as described in the introduction), yet we see a correlation with features in the western US, as well as an overall trend of attenuation strength as a function of period. For example, the lateral patterns of high attenuation near the Yellowstone Hotspot, low attenuation near the boundary of the Colorado Plateau, and some high attenuation in the Mojave Desert on the southeast edge of the Sierra Nevada Range are all consistent between both methods at 24 seconds. However, the strength of attenuation reported is very different, with values of attenuation coefficient near $\alpha = 3 \cdot 10^{-3}$ km^{-1} near Yellowstone and the Mojave Desert at 24 seconds, compared with our values of near $\alpha = 0.4 \cdot 10^{-3}$ km^{-1} at those same locations. Some other differences remain as well, such as northeast of the Basin-and-Range Province for which we observe high attenuation, but the Lawrence and Prieto observations show none (at 24 s). Our maps are, admittedly, presented with lower resolution than the Lawrence and Prieto results, but for various methodological reasons we are more confident in the wavefront tracking observations. The maps from Lawrence and Prieto, for example, use different assumptions about the background noise model (as mentioned in the introduction), and do not account for focusing and defocusing of energy or local amplification as our wavefront tracking approach does. Thus, although the method of Lawrence and Prieto may lead to some reasonable lateral patterns of attenuation structure, their methods and assumptions may introduce significant bias in their quantitative results.

4.4.3 Conclusions

This paper demonstrates that tracking the amplitudes of wavefronts derived from ambient noise correlations yields expected and consistent measurements. As long as one is careful with the processing and stacking of ambient noise correlations, the evolution of a wavefield derived from an ambient noise virtual source behaves just as for earthquake sources, even when true Green's functions are not obtained. Demonstration of this functionality from USArray data, which is well understood tectonically and previously studied using earthquake-based measurements, paves the way for similar array-based approaches to continue in the future at other scales and periods, as was used on a city-scale dense array in Long Beach, CA [*Bowden et al., 2016]*.

The surface-wave amplification and attenuation maps derived here complement the longer period maps from *Lin et al.* [2012a], *Eddy and Ekström* [2014] and *Bao et al.* [2016], with observations extending down to 8-second period, and providing an additional observable for the shallower regions of the crust. The maps show reasonable correlation with known tectonic and velocity structure, and any subtle differences may be used in the future to better constrain velocity structure, Vp/Vs or density relations. In the future, joint inversions should also be possible, using these measurements to complement existing observations of phase velocity, group velocity, H/V ratios, receiver functions and others.

Finally, the surface-wave attenuation maps presented here provide some of the highest resolution and most complete coverage of the crust in the continental US. They correlate well with known surface temperature anomalies and may be used in the future to constrain such properties as fluid content or temperature at depth. Alternatively, they provide empirical observations that may be directly used in hazard studies or other types of waveform estimation where surface waves are important.

4.5 Acknowledgments and Data

Data from USArray was downloaded from the IRIS Data Management Center at http://www.iris. edu/hq/. The velocity model of *Schmandt et al.* [2015] was downloaded from IRIS at http://ds.iris.edu/ds/products/emc-us-crustvs-2015/. Amplification and attenuation maps are included as Supporting Information, and other results are available upon request to dbowden@caltech.edu. This work was supported by EAR-1453263 and EAR-1252191. F.-C.L. was supported by NSF grant CyberSEES-1442665 and the King Abdullah University of Science and Technology (KAUST) under award OCRF-2014-CRG3-2300.

4.6 References

Bao, X., C. A. Dalton, G. Jin, J. B. Gaherty, and Y. Shen (2016), Imaging Rayleigh wave attenuation with USArray, *Geophys. J. Int., 206*(1), 241–259, doi:10.1093/gji/ggw151.

Bensen, G. D., M. H. Ritzwoller, M. P. Barmin, a. L. Levshin, F. Lin, M. P. Moschetti, N. M. Shapiro, and Y. Yang (2007), Processing seismic ambient noise data to obtain reliable broad-band surface wave dispersion measurements, *Geophys. J. Int., 169*(3), 1239–1260, doi:10.1111/j.1365-246X.2007.03374.x.

Blackwell, D., M. Richards, Z. Frone, A. Ruzo, R. Dingwall, and M. Williams (2011), Temperature-At-Depth Maps For the Conterminous US and Geothermal Resource Estimat, *GRC Trans., 35*(GRC1029452).

Bowden, D. C., and V. C. Tsai (2017), Earthquake ground motion amplification for surface waves, *Geophys. Res. Lett., 43*, 1–8, doi:10.1002/2016GL071885.

Bowden, D. C., V. C. Tsai, and F. C. Lin (2015), Site amplification, attenuation, and scattering from noise correlation amplitudes across a dense array in Long Beach, CA, *Geophys. Res. Lett., 42*, doi:10.1002/2014GL062662.

Brocher, T. M. (2005), Empirical relations between elastic wavespeeds and density in the Earth's crust, *Bull. Seismol. Soc. Am., 95*(6), 2081–2092, doi:10.1785/0120050077.

Campillo, M., and A. Paul (2003), Long-range correlations in the diffuse seismic coda., *Science, 299*(5606), 547–9, doi:10.1126/science.1078551.

Cupillard, P., and Y. Capdeville (2010), On the amplitude of surface waves obtained by noise correlation and the capability to recover the attenuation: A numerical approach, *Geophys. J. Int., 181*(3), 1687–1700, doi:10.1111/j.1365-246X.2010.04586.x.

Dalton, C. A., and G. Ekström (2006a), Constraints on global maps of phase velocity from surface-wave amplitudes, *Geophys. J. Int., 167*(2), 820–826, doi:10.1111/j.1365-246X.2006.03142.x.

Dalton, C. A., and G. Ekström (2006b), Global models of surface wave attenuation, *J. Geophys. Res. Solid Earth, 111*(5), 1–19, doi:10.1029/2005JB003997.

Denolle, M. A., E. M. Dunham, G. A. Prieto, and G. C. Beroza (2014), Strong ground motion prediction using virtual earthquakes., *Science, 343*(6169), 399–403, doi:10.1126/science.1245678.

Eddy, C. L., and G. Ekström (2014), Local amplification of Rayleigh waves in the continental United States observed on the USArray, *Earth Planet. Sci. Lett., 402*(C), 50–57, doi:10.1016/j.epsl.2014.01.013.

Ekström, G. (2014), Love and Rayleigh phase-velocity maps, 5-40 s, of the western and central USA from USArray data, *Earth Planet. Sci. Lett., 402*(C), 42–49, doi:10.1016/j.epsl.2013.11.022.

Ermert, L., A. Villaseñor, and A. Fichtner (2016), Cross-correlation imaging of ambient noise sources, *Geophys. J. Int., 204*(1), 347–364, doi:10.1093/gji/ggv460.

Ferreira, A. M. G., and J. H. Woodhouse (2007), Source, path and receiver effects on seismic surface waves, *Geophys. J. Int., 168*(1), 109–132, doi:10.1111/j.1365-246X.2006.03092.x.

Fichtner, A., L. Stehly, L. Ermert, and C. Boehm (2016), Generalised interferometry - I. Theory for inter-station correlations, *Geophys. J. Int.,* ggw420, doi:10.1093/gji/ggw420.

Herrmann, R. B. (2013), Computer Programs in Seismology: An Evolving Tool for Instruction and Research, *Seismol. Res. Lett., 84*(6), 1081–1088, doi:10.1785/0220110096.

Huang, H., F. Lin, B. Schmandt, J. Farrell, R. B. Smith, and V. C. Tsai (2015), The Yellowstone magmatic system from the mantle plume to the upper crust, *Science* (80)., 348(6236), 773–776.

Jin, G., and J. B. Gaherty (2015), Surface wave phase-velocity tomography based on multichannel cross-correlation, *Geophys. J. Int., 201*(3), 1383–1398, doi:10.1093/gji/ggv079.

Karato, S. (1993), Importance of Anelasticity in the Interpretation of Seismic Tomography, *Geophys. Res. Lett., 20*(15), 1623–1626.

Kumar, P., R. Kind, X. Yuan, and J. Mechie (2012), USArray Receiver Function Images of the Lithosphere-Asthenosphere Boundary, *Seismol. Res. Lett., 83*(3), 486–491, doi:10.1785/gssrl.83.3.486.

Lawrence, J. F., and G. a. Prieto (2011), Attenuation tomography of the western United States from ambient seismic noise, *J. Geophys. Res., 116*(B6), B06302, doi:10.1029/2010JB007836.

Lawrence, J. F., M. Denolle, K. J. Seats, and G. a. Prieto (2013), A numeric evaluation of attenuation from ambient noise correlation functions, *J. Geophys. Res. Solid Earth, 118*(12), 6134–6145, doi:10.1002/2012JB009513.

Levshin, A. L., and M. H. Ritzwoller (2001), Automated Detection, Extraction, and Measurement of Regional Surface Waves, edited by A. L. Levshin and M. H. Ritzwoller, *Pure Appl. Geophys., 158*(8), 1531–1545, doi:10.1007/978-3-0348-8264-4_11.

Liang, C. (2013), Wave Gadiometry applied to near surface, in *First Near Surface Geophysics Asia Pacific Conference*, pp. 160–163.

Lin, F.-C., and M. H. Ritzwoller (2011), Helmholtz surface wave tomography for isotropic and azimuthally anisotropic structure, *Geophys. J. Int., 186*(3), 1104–1120, doi:10.1111/j.1365-246X.2011.05070.x.

Lin, F.-C., M. H. Ritzwoller, and R. Snieder (2009), Eikonal tomography: surface wave tomography by phase front tracking across a regional broad-band seismic array, *Geophys. J. Int., 177*(3), 1091–1110, doi:10.1111/j.1365-246X.2009.04105.x.

Lin, F.-C., V. C. Tsai, and M. H. Ritzwoller (2012a), The local amplification of surface waves: A new observable to constrain elastic velocities, density, and anelastic attenuation, *J. Geophys. Res., 117*(B6), B06302, doi:10.1029/2012JB009208.

Lin, F.-C., D. Li, R. W. Clayton, and D. Hollis (2013), High-resolution 3D shallow crustal structure in Long Beach, California: Application of ambient noise tomography on a dense seismic array, *Geophysics, 78*(4), Q45–Q56, doi:10.1190/geo2012-0453.1.

Lin, F. C., B. Schmandt, and V. C. Tsai (2012b), Joint inversion of Rayleigh wave phase velocity and ellipticity using USArray: Constraining velocity and density structure in the upper crust, *Geophys. Res. Lett., 39*(12), 1–7, doi:10.1029/2012GL052196.

Lin, F. C., V. C. Tsai, and B. Schmandt (2014), 3-D crustal structure of the western United States: Application of Rayleigh-wave ellipticity extracted from noise cross-correlations, *Geophys. J. Int., 198*(2), 656–670, doi:10.1093/gji/ggu160.

Liu, X., Y. Ben-zion, and D. Zigone (2015), Extracting seismic attenuation coefficients from cross-correlations of ambient noise at linear triplets of stations, *Geophys. J. Int., 203*, 1149–1163, doi:10.1093/gji/ggv357.

Longuet-Higgins, M. S. (1950), A Theory of the Origin of Microseisms, *Philos. Trans. R. Soc. A Math. Phys. Eng. Sci., 243*(857), 1–35, doi:10.1098/rsta.1950.0012.

Ma, Y., and R. W. Clayton (2014), The crust and uppermost mantle structure of Southern Peru from ambient noise and earthquake surface wave analysis, *Earth Planet. Sci. Lett., 395*, 61–70, doi:10.1016/j.epsl.2014.03.013.

Menon, R., P. Gerstoft, and W. S. Hodgkiss (2014), Journal of Geophysical Research : Solid Earth On the apparent attenuation in the spatial coherence estimated from seismic arrays, *J. Geophys. Res. Solid Earth, 119*, 3115–3132, doi:10.1002/2013JB010835.

Mitchell, B. J. (1995), Anelastic structure and evolution of the continental crust and upper mantle from seismic surface wave attenuation, *Rev. Geophys., 33*(95), 441–462, doi:10.1029/95RG02074.

Mitchell, B. J., L. W. B. Leite, Y. K. Yu, and R. B. Herrmann (1976), Attenuation of Love and Rayleigh Waves Across the Pacific at Periods Between 15 and 110 Seconds, *Bull. Seismol. Soc. Am., 66*(4), 1189–1202.

Mooney, W. D., and M. K. Kaban (2010), The North American upper mantle: Density, composition, and evolution, *J. Geophys. Res. Solid Earth, 115*(12), 1–24, doi:10.1029/2010JB000866.

De Noyer, J. (1961), The Effect of Variations in Layer Thickness on Love Waves, *Bull. Seism. Soc. Am., 51*(2), 227–235.

Porritt, R. W., R. M. Allen, and F. F. Pollitz (2014), Seismic imaging east of the Rocky Mountains with USArray, *Earth Planet. Sci. Lett., 402*(C), 16–25, doi:10.1016/j.epsl.2013.10.034.

Priestley, K., and D. McKenzie (2006), The thermal structure of the lithosphere from shear wave velocities, *Earth Planet. Sci. Lett., 244*(1–2), 285–301, doi:10.1016/j.epsl.2006.01.008.

Prieto, G. a., J. F. Lawrence, and G. C. Beroza (2009), Anelastic Earth structure from the coherency of the ambient seismic field, *J. Geophys. Res., 114*(B7), B07303, doi:10.1029/2008JB006067.

Prieto, G. A., M. Denolle, J. F. Lawrence, and G. C. Beroza (2011a), On amplitude information carried by the ambient seismic field, *Comptes Rendus - Geosci., 343*(8–9), 600–614, doi:10.1016/j.crte.2011.03.006.

Prieto, G. A., M. Denolle, J. F. Lawrence, and G. C. Beroza (2011b), On amplitude information carried by the ambient seismic field, *Comptes Rendus Geosci., 343*(8–9), 600–614, doi:10.1016/j.crte.2011.03.006.

Schmandt, B., and F. Lin (2014), P and S wave tomography of the mantle beneath the United States, *Geophys. Res. Lett.,* 6342–6349, doi:10.1002/2014GL061231.

Schmandt, B., F. C. Lin, and K. E. Karlstrom (2015), Distinct crustal isostasy trends east and west of the Rocky Mountain Front, *Geophys. Res. Lett., 42*(23), 10290–10298, doi:10.1002/2015GL066593.

Seats, K. J., & Lawrence, J. F. (2014). The seismic structure beneath the Yellowstone Volcano Field from ambient seismic noise. *Geophys. Res. Lett.*, *41*, 8277–8282. https://doi.org/10.1002/2014GL061913

Shen, W., M. H. Ritzwoller, and V. Schulte-Pelkum (2013), A 3-D model of the crust and uppermost mantle beneath the Central and Western US by joint inversion of receiver functions and surface wave dispersion, *J. Geophys. Res. Solid Earth, 118*(1), 262–276, doi:10.1029/2012JB009602.

Snieder, R. (2004), Extracting the Green's function from the correlation of coda waves: A derivation based on stationary phase, *Phys. Rev. E, 69*(4), 46610, doi:10.1103/PhysRevE.69.046610.

Tromp, J., and F. A. Dahlen (1992), Variational principles for surface wave propagation on a laterally heterogeneous Earth-11. Frequency-domain JWKB theory, *Geophys. J. Int., 109*, 599–619.

Tsai, V. C. (2010), The relationship between noise correlation and the Green's function in the presence of degeneracy and the absence of equipartition, *Geophys. J. Int., 182*(3), 1509–1514, doi:10.1111/j.1365-246X.2010.04693.x.

Tsai, V. C. (2011), Understanding the amplitudes of noise correlation measurements, *J. Geophys. Res., 116*(B9), B09311, doi:10.1029/2011JB008483.

Tsai, V. C., D. C. Bowden, and H. Kanamori (2017), Explaining extreme ground motion in Osaka basin during the 2011 Tohoku earthquake, *Geophys. Res. Lett., 44*, 7239–7244, doi:10.1002/ 2017GL074120.

Viens, L., K. Koketsu, H. Miyake, S. Sakai, and S. Nakagawa (2016), Basin-scale Green's functions from the ambient seismic field recorded by MeSO-net stations, *J. Geophys. Res. Solid Earth, 121*, 2507–2520, doi:10.1002/2016JB012796.

Viens, L., M. Denolle, H. Miyake, S. Sakai, and S. Nakagawa (2017), Retrieving impulse response function amplitudes from the ambient seismic field, *Geophys. J. Int., 210*, 210–222, doi:10.1093/gji/ggx155.

Weaver, R. L. (2011a), On the amplitudes of correlations and the inference of attenuations, specific intensities and site factors from ambient noise, *Comptes Rendus - Geosci., 343*(8–9), 615–622, doi:10.1016/j.crte.2011.07.001.

Weaver, R. L. (2011b), On the retrieval of attenuation from the azimuthally averaged coherency of a diffuse field, *Comptes Rendus Geosci., 343*, 615–622.

Wessel, P., W. H. F. Smith, R. Scharroo, J. Luis, and F. Wobbe (2013), Generic Mapping Tools: Improved Version Released, *Eos (Washington. DC)., 94*(45), 409–410, doi:10.1002/2013EO450001.

Yang, Y., and D. W. Forsyth (2008), Attenuation in the upper mantle beneath Southern California: Physical state of the lithosphere and asthenosphere, J. *Geophys. Res. Solid Earth, 113*(3), 1–12, doi:10.1029/2007JB005118.

Chapter 5

EARTHQUAKE GROUND MOTION AMPLIFICATION FOR SURFACE WAVES

Bowden, D. C., & Tsai, V. C. (2017). Earthquake ground motion amplification for surface waves. *Geophys. Res. Lett.*, *43*, 1–8. https://doi.org/10.1002/2016GL071885

5.1 Abstract

Surface waves from earthquakes are known to cause strong damage, especially for larger structures such as skyscrapers and bridges. However, common practice in characterizing seismic hazard at a specific site considers the effect of near-surface geology on only vertically propagating body waves. Here we show that surface waves have a unique and different frequency-dependent response to known geologic structure, and that this amplification can be analytically calculated in a manner similar to current hazards practices. Applying this framework to amplification in the Los Angeles Basin, we find that peak ground accelerations for certain large regional earthquakes are under-predicted if surface waves are not properly accounted for, and that the frequency of strongest ground motion amplification can be significantly different. Including surface-wave amplification in hazards calculations is therefore essential for accurate predictions of strong ground motion for future San Andreas Fault ruptures.

5.2 Introduction

A significant portion of the variability in earthquake ground motions is caused by local geological conditions immediately beneath a given site. It is well known, for example, that shallow sediments or soils can give rise to amplification and resonances as seismic waves propagate near vertically up to the surface [e.g., *Borcherdt and Gibbs,* 1976], notably occurring when wavelengths are four times the depth of the near-surface low-velocity layer. For this reason, it has become standard practice in earthquake engineering to use the local one-dimensional (1D) shallow velocity structure at a site (or a proxy for it, e.g., *Wills et al.,*

[2000]; *Wald and Allen,* [2007]) to calculate the amount of local amplification that results for each site, as compared to a reference 'hard rock' site [e.g., *Dobry et al.,* 1976; *Kramer,* 1996; *Kawase,* 2003]. Even when the actual 1D geologic profile is not known, this description of vertical resonances underlies the interpretation of numerous empirical and observational approaches (e.g., single-site horizontal-to-vertical spectral ratio to determine peak resonance). While it is acknowledged that this description of vertically-incident shear waves does not capture the full variability of 3D wave propagation effects [e.g., *Olsen and Schuster,* 1995; *Field et al.,* 2000; *Graves et al.,* 2011], the 1D site term defined this way supplies a simple, consistent framework that can be practically implemented by engineers, providing the foundation for earthquake building codes and classifications [e.g., *Abrahamson and Shedlock,* 1997; *Dobry et al.,* 2000].

Here we show that site characterization calculations can be improved by accounting for surface-wave amplification in addition to the standard amplification of vertically propagating shear waves. It has long been recognized that surface waves propagate and amplify differently due to crustal heterogeneities [e.g., *Drake,* 1980; *Bard and Bouchon,* 1980; *Sánchez-Sesma,* 1987, *Kawase and Aki,* 1989; *Joyner,* 2000]. However, their amplification has often been ignored in site specific estimates, partly due to the assumption that this amplification is challenging to model (e.g., requiring full-wavefield simulations) and that surface waves are most significant at periods not important for ordinary buildings [e.g., *Joyner,* 2000]. Contrary to both of these expectations, we show that application of analytic theory developed originally for long-period surface waves can be readily applied to the shorter period ground motions important for earthquake hazards. While fully estimating the expected shaking from future events remains a complex problem, the definition of a site-amplification term can be extended to include surface waves separately from that of vertically-incident shear waves.

5.3 Analytic Description

From long-period, global or tectonic-scale seismology studies [i.e., *Tromp and Dahlen,* 1992], it is known that conservation of energy flux requires that the relative surface-wave amplitudes between two sites satisfies

$$\frac{\boldsymbol{A_n}}{\boldsymbol{A_n}^{\boldsymbol{R}}} = \frac{\boldsymbol{u_n(0)}}{\boldsymbol{u_n}^{\boldsymbol{R}}\boldsymbol{(0)}}\left(\frac{\boldsymbol{UI_0}}{\boldsymbol{U^R I_0}^{\boldsymbol{R}}}\right)^{-\frac{\boldsymbol{1}}{\boldsymbol{2}}} \qquad \text{Eq. 5.1}$$

where $u_n(0)$ is the displacement eigenfunction measured at the surface (depth = 0) corresponding to the type of wave measured by A_n (where n = 1, 2 or 3 for radial, vertical and tangential component of motion, respectively),U is group velocity, I_0 is an integral over the eigenfunctions and density, and superscript R refers to measurements at a reference site. Specifically, the term $1/(UI_0)$ describes a wave action potential [*Tromp and Dahlen,* 1992] and also appears in the standard formulation of surface-wave Green's functions [e.g., *Aki and Richards,* 2002], and is simply applied here in a hazards context. The I_0 integrals referred to in Eq. 5.1 are usually used to describe the kinetic energy of surface waves, used in the Lagrangian formulation to determine group and phase velocities. These integrals are defined differently for Rayleigh and Love waves as

$$\text{Rayleigh:}\quad \boldsymbol{I_0} = \int_{\boldsymbol{0}}^{\boldsymbol{\infty}} \boldsymbol{\rho(z)(u_1(z)^2 + u_2(z)^2)dz} \qquad \text{Eq. 5.2}$$

$$\text{Love:}\quad \boldsymbol{I_0} = \int_{\boldsymbol{0}}^{\boldsymbol{\infty}} \boldsymbol{\rho(z)u_3(z)^2 dz} \qquad \text{Eq. 5.3}$$

where ρ is density and z is depth. We note that the Rayleigh-wave eigenfunctions are usually normalized such that the vertical component of motion, u_2, is one at the surface. In this case, the u_n/u_n^R term in Eq. 5.1 is simply one for vertical amplification at the surface, and for horizontal amplification, u_1 is the horizontal-to-vertical (H/V) ratio. Love waves are usually similarly normalized such that the term, u_3, is one at the surface. While the literature originally defining these amplitude relations considered surface-wave-potential amplitudes [*Tromp and Dahlen,* 1992], we are interested in displacements, and so we describe

displacement amplitudes by multiplying the potentials by the corresponding eigenfunction to specify the component of motion considered.

The expression A_n/A_n^R in Eq. 5.1 defines a frequency-dependent transfer function by which observations of ground motion at a reference site can be transformed to any other site, each described by a 1D profile. Although this relation has typically been applied to only very long-period surface waves (e.g., greater than 24 seconds by *Lin et al.,* [2012]), the same physics applies to high-frequency surface waves as long as the velocity structure varies smoothly enough laterally [*Tromp and Dahlen,* 1992]. This description of relative local site amplification does not and should not include terms for path effects; anything that might affect the amplitudes due to the path of a ray such as focusing, attenuation, lateral basin resonance [e.g., *Bard and Bouchon,* 1985] or a conversion of wavetypes at sharp boundaries [e.g., *Liu and Heaton,* 1984; *Field,* 1996] is not described here, nor is this formulation concerned with the excitation of surface waves. Although the original formulation deals with conservation of energy traveling along a particular ray, in a site response context it can be applied to represent the transfer function between any two 1D profiles, with the result describing the additional local amplification that would result by replacing the reference structure by the given site structure at any point. This is analogous to how a 1D velocity profile is often used to calculate the standard vertically-incident shear-wave transfer function for engineering applications. For both types of waves, the locally 1D assumption is still a simplification of reality [*Thomson et al.,* 2009], but results in a useful, first-order quantification of how much ground motions are affected by local geology.

It may also be noted that Rayleigh waves can alternately be described as a superposition of P and SV waves, and similarly Love waves can be described as trapped SH waves propagating and reflecting at a critical incidence angle. However, the near-horizontal incidence angle will also strongly affect the amplification strength and frequency [*Haskell,* 1960]. While other authors have noted that resonant shear waves may not be perfectly

vertical and thus show some polarization [e.g., *Boore et al.,* 2006], there is still a significant difference between such cases and fully developed surface waves.

5.4 Simple Basin Example

Fig. 5.1 shows a comparison of site response terms calculated for both vertically-incident shear waves and surface waves in a simple sedimentary basin of 500-m depth, compared to a reference homogeneous half space. The site response term for vertically-incident shear waves are semi-analytically estimated using a Thomson-Haskell propagator matrix approach [*Haskell,* 1953], although for this simple example a straightforward analytic solution also exists (for which the peak resonant frequency is $V_{s1}/4H$). Surface-wave eigenfunctions are also semi-analytically estimated using Computer Programs in Seismology [*Herrmann,* 2013]. The medium for both wave types is purely elastic and without attenuation. Certainly, varying rates of attenuation and geometric spreading will play a significant role in the relative strengths of these wave types, but these are not part of the site amplification transfer function presented here.

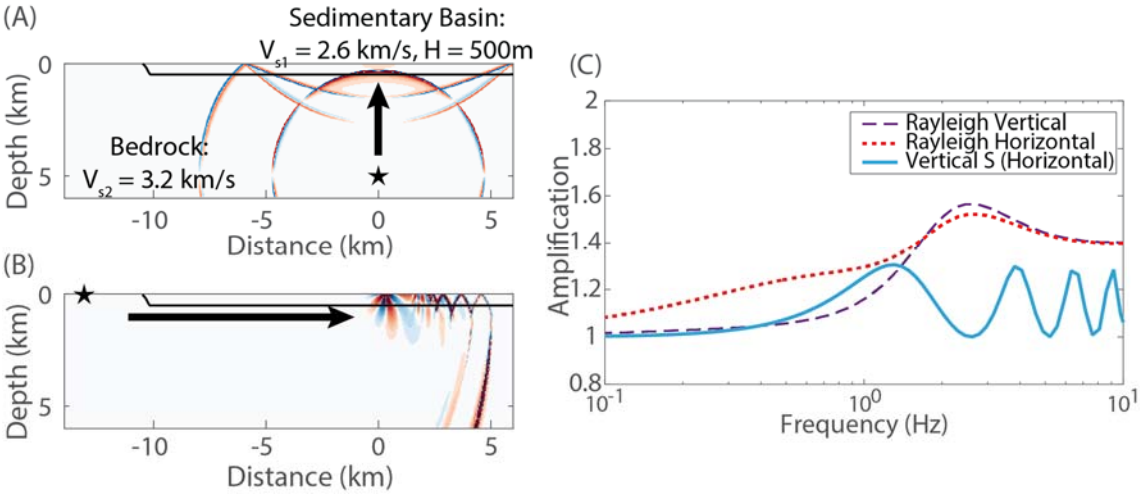

Figure 5.1: Comparison of amplification terms in a sedimentary basin, for (A) a vertically-incident shear wave or (B) a laterally propagating Rayleigh wave. The spectral amplification patterns (C) indicate that the two wave types interact with the low-velocity sedimentary layer in different ways. For this example, the shear-wave velocity is set as 2.6 km/s in the basin and 3.2 km/s outside the basin. Note that for a more severe velocity contrast, all wave types would be more significantly amplified, but the comparison would be qualitatively similar.

Although both wave types are amplified, there is a significant quantitative difference for the surface waves entering this basin compared to the shear waves. For this idealized model, surface-wave amplification is roughly 50% stronger than and with a peak frequency twice that of the vertically-incident shear wave (see Fig. 5.1c). Furthermore, although surface waves are often ignored at higher frequencies, it is these higher frequencies for which surface waves are most amplified. While other authors have observed the changing frequency content and amplitudes of surface wave arrivals [e.g., *Pinnegar,* 2006], it is not generally considered that an entirely separate and unique transfer function can be used to describe the surface-wave system.

We note that the difference between the wave-types' amplification spectra is persistent for other models. Even for a variety of tested basin depths, impedance contrasts and even for more realistic geologic profiles [e.g., *Boore and Joyner,* 1997], the differences in amplification remain persistent (see Fig. S5.1). Lastly, we note that these transfer functions are confirmed through 2D finite difference simulations [*Li et al.,* 2014], with only minor differences caused by path effects such as scattering and a conversion of wave types at the edge of the sedimentary basin.

5.5 Application to a Southern California Velocity Model

This straightforward calculation of site terms can be implemented for any velocity model from which 1D profiles can be extracted, including in southern California, where recent developments of the Southern California Earthquake Center's Community Velocity Model (SCEC CVM-S4.26) [*Lee et. al,* 2014] facilitates this re-examination of seismic hazard. Efforts to account for surface waves are especially important for southern California, where wavefronts from a future large earthquake on the San Andreas Fault system [*Graves et al.,* 2011] will enter the Los Angeles Basin laterally rather than from below (see Fig. 5.1a). Fig. 5.2 demonstrates the spatial variability of site terms at 0.4 Hz for each of a vertically-incident shear wave, Rayleigh wave (horizontal component) and Love wave, all relative to the hard-rock site at station PASC in Pasadena, and based only on 1D profiles at each point. As

expected, the depth of the Los Angeles sedimentary basin plays a significant role [e.g., *Hruby and Beresnev,* 2003; *Day et al.,* 2008]: the deepest region of the sedimentary basin causes surface waves to be strongly and consistently amplified, while vertically-incident shear waves do not all exhibit resonance given the variable basin shape. For example, the center of the basin near station WTT is too deep for resonance of vertically-incident shear wave at this period.

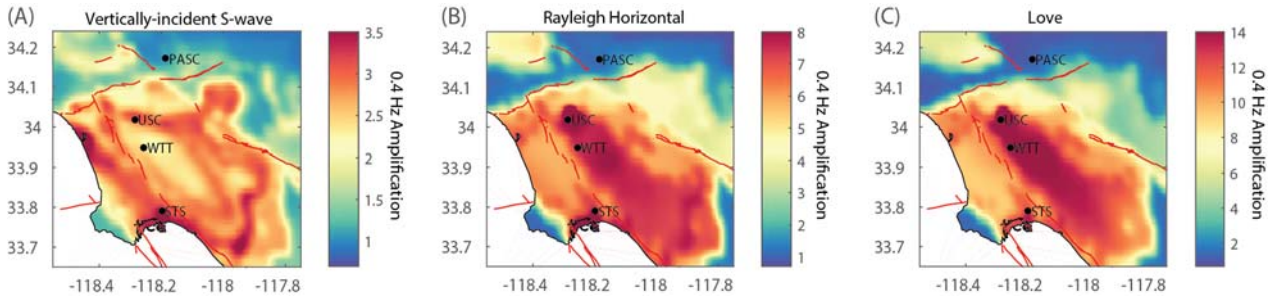

Figure 5.2: Maps of relative amplification for southern California, describing 1D amplification factors relative to the hard rock site, PASC, at 0.4 Hz for (A) vertically-incident shear waves, (B) horizontal-component Rayleigh waves, and (C) Love waves. Faults from the U.S. Geological Survey and California Geological Survey (2006) are shown by red lines.

The Love-wave amplification predictions of Fig. 5.2 are considerably higher than for the other wave types. This is partly because the geologic structure at our reference site, PASC, allows for little Love wave energy. On one hand, this may give a startling impression regarding the severity of Love waves in this basin, but it also serves to illustrate that if a hard-rock reference station (like PASC) is used for any type of ground motion prediction or hazard estimate, Love waves will be significantly under-predicted from the analysis. The choice of a different reference bedrock site will affect the intensity of amplifications reported in these maps, though the dominant lateral features will remain.

Observations of ground motions confirm these differences in relative amplification. Specifically, we consider ground motions of the El Mayor Cucapah Earthquake, Mw7.2,

which occurred SE of the Los Angeles Basin in 2010. Four stations are indicated in Fig. 5.2, each a comparable distance and azimuth from the event such that attenuation and geometric spreading can be assumed comparable. Fig. 5.3A-C shows the raw acceleration records, and we observe that the peak ground acceleration (PGA) relative to the hard-rock site, PASC, is different when we consider shear-wave arrivals separately from surface waves. While distinguishing surface waves from various body wave phases may often be difficult in practice (particularly for higher frequency waves), we emphasize that PGA is often higher in the surface-wave window compared to the body-wave window (including for six of the nine basin ground motion records shown in Fig. 5.3), despite the significant attenuation of high-frequency surface waves at this distance.

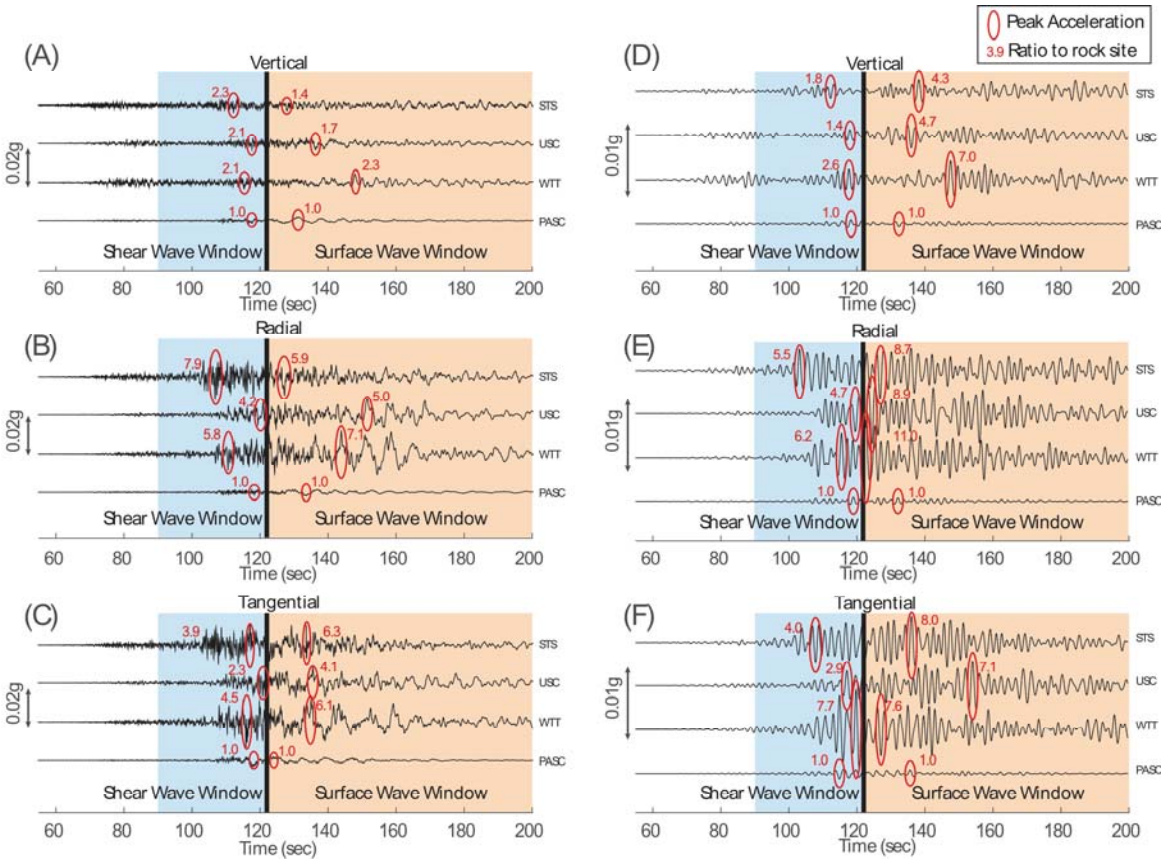

Figure 5.3: Acceleration waveforms comparing shear and surface waves, from the El Mayor-Cucapah earthquake, M7.2, with its epicenter roughly 130 km to the SE of

the Los Angeles Basin. Panels A-C are unfiltered accelerations for vertical, radial and tangential components, respectively. Panels D-F are filtered at 0.3-0.7 Hz. In each panel, Peak Ground Acceleration (PGA) is identified for shear waves and surface waves separately, and the ratio of this PGA to the hard rock site, PASC, is indicated.

When comparing filtered waveforms (Fig. 5.3D-F), these differences are even more severe. At frequencies of 0.3-0.7 Hz, surface waves are amplified 2-3 times more strongly than shear waves, relative to the hard-rock site, again commensurate with predictions from the SCEC CVM in Fig. 5.2. Our division between shear-wave arrivals and surface-wave arrivals is based only on visual inspection of the hard-rock site waveform, and some of the PGA peaks may be ambiguous or close to the boundary. As such, a more rigorous approach describing arrival energy with time could be applied or developed in the future [e.g., *Saikia et al.,* 1994]. The predictions shown in Fig. 5.2 do not account for path effects or other 3D surface-wave phenomena, such as lateral basin resonance or conversion of wavetypes at sharp boundaries, yet the application of the appropriate 1D site terms alone explains the most significant features of the waveforms, thus demonstrating the usefulness of the simplified 1D amplification approach.

5.6 Discussion and Conclusions

In this work, we have shown that the nature of wave propagation results in different amounts of amplification by local geological structure for surface waves as compared to body waves. Moreover, a simple analytic theory can be applied to 1D velocity structures to predict the amount of surface-wave amplification separately from the body-wave amplification that is more commonly computed. The differences in site-amplification spectra shown here indicate that if surface waves are to be included in any kind of hazard analysis, the analysis should include a frequency-dependent site response that is appropriate for surface waves. While some ground motion prediction equations (GMPEs) include terms for the presence of basins or long-period signals [e.g., *Novikova and Trifunac,* 1994; *Campbel and Borzognia,* 2013], and therefore may implicitly account for surface wave site response if the historical data contained these signals, application of the analytic theory used and described in this paper

can explicitly account for surface waves independently of body waves, and thus allow for the design of a more flexible and complete hazards model. Differences in source and path effects such as attenuation [e.g., *Mitchell,* 1973] and geometric spreading would also need to be accounted for, and this complexity suggests the importance of either simulations (e.g., *Graves et al.,* 2010] or empirical observations [e.g., *Denolle et al.,* 2014], which describe the full waveform. Nonetheless, describing a site amplification term appropriate to each wave type represents a first step towards such an improved hazards model.

Independent of these considerations above, the differences in amplification spectra have implications for a broad range of hazard estimation techniques and the resulting interpretation. For example, if spectral ratios between two sites are measured, the existence of surface-wave signals will fundamentally change the measurement [e.g., *Field,* 1996]. Conversely, if empirical records from a hard rock site are modified for use in structural response simulations at a sedimentary basin site, the later arrivals in the waveforms may be significantly misrepresented if only the standard, vertically-incident shear wave site term is applied. Cases where surface waves ultimately contribute to the highest levels of ground motion may explain some of the epistemic variability observed in strong motion catalogs, since correlations with local geology or other proxies do not have the same relationship between surface waves and body waves. For all of these reasons, scientists and engineers need to be aware that a single definition of "site amplification" may be insufficient to describe both surface waves and body waves, in regards to both frequency and amplitude.

5.7 Acknowledgments and Data

The velocity model used for southern California is the SCEC CVM-S4.26, accessed from https://scec.usc.edu/scecpedia, on Feb 25, 2016, as part of the Unified Community Velocity Model package version 15.10.0. Seismograms are provided by the Caltech/USGS Southern California Seismic Network at http://scedc.caltech.edu. Surface wave eigenfunctions are generated through R. Herrmann's Computer Programs in Seismology (available at http://www.eas.slu.edu/eqc/eqccps.html). Vertical transfer functions were validated against

C. Mueller's NRATTLE script, provided as part of the SMSIM package by D. Boore (available at http://pubs.er.usgs.gov/publication/ofr00509).

The authors thank Jian Shi, Fan-Chi Lin, Rob Clayton and Raul Castro for helpful discussion. We also thank Francisco Sánchez-Sesma and one anonymous reviewer for helpful feedback in preparation of the manuscript. This work was supported by EAR-1252191, EAR-1453263 and SCEC-15035.

5.8 References

Abrahamson, N. A., and K. M. Shedlock (1997), Overview, *Seismol. Res. Lett.*, *68*(1), 9–23.

Aki, K., and P. G. Richards (2002), *Quantitative seismology*, University Science Books.

Bard, P.-Y., and M. Bouchon (1985), The Two-Dimensional Resonance of Sediment-Filled Valleys, *Bull. Seismol. Soc. Am.*, *75*(2), 519–541.

Bard, P.-Y., and M. Bouchon (1980), The seismic response of sediment-filled valleys. Part 2. The case of incident P and SV waves, *Bull. Seismol. Soc. Am.*, *70*(5), 1921–1941.

Boore, D. M. (2006), Orientation-Independent Measures of Ground Motion, *Bull. Seismol. Soc. Am.*, *96*(4A), 1502–1511, doi:10.1785/0120050209.

Boore, D. M., and W. B. Joyner (1997), Site amplifications for generic rock sites, *Bull. Seismol. Soc. Am.*, *87*(2), 327–341.

Borcherdt, R. D., and J. F. Gibbs (1976), Effects of local geological conditions in the San Francisco bay region on ground motions and the intensities of the 1906 earthquake, *Bull. Seism. Soc. Am.*, *66*(2), 467–500.

Campbell, K. W., and Y. Bozorgnia (2013), NGA-West2 Campbell-Bozorgnia ground motion model for the horizontal components of PGA, PGV, and 5% damped elastic pseudo-acceleration response spectra for periods ranging from 0.01 to 10 sec, PEER Report 2013/06.

Day, S. M., R. Graves, J. Bielak, D. Dreger, S. Larsen, K. B. Olsen, A. Pitarka, and L. Ramirez-Guzman (2008), Model for basin effects on long-period response spectra in southern California, *Earthq.* Spectra, *24*(1), 257–277, doi:10.1193/1.2857545.

Denolle, M. A., H. Miyake, S. Nakagawa, N. Hirata, and G. C. Beroza (2014), Long-period seismic amplification in the Kanto Basin from the ambient seismic field, *Geophys. Res. Lett.*, *41*, 2319–2325, doi:10.1002/2014GL059425.

Dobry, R., R. D. Borcherdt, C. B. Crouse, I. M. Idriss, W. B. Joyner, G. R. Martin, M. S. Power, E. E. Rinne, and R. B. Seed (2000), New site coefficients and site classification system used in recent building code provisions, *Earthq. Spectra*, *16*(1), 41–67.

Dobry, R., I. Oweis, and A. Urzua (1976), Simplified procedures for estimating the fundamental period of a soil profile, *Bull. Seism. Soc. Am.*, *66*(4), 1293–1321.

Drake, L. A. (1980), Love and Rayleigh Waves in an Irregular Soil Layer, *Bull. Seismol. Soc. Am.*, *70*(2), 571–582.

Field, E. H. (1996), Spectral amplification in a sediment-filled valley exhibiting clear basin-edge-induced waves, *Bull. Seismol. Soc. Am.*, *86*(4), 991–1005, doi:10.1130/0091-7613(2000)28<315:MWEFFA>2.0.CO;2.

Field, E. H. and the SCEC Phase III Working Group (2000), Accounting for site effects in probabilistic seismic hazard analyses of southern California: Overview of the SCEC Phase III report, *Bull. Seismol. Soc. Am.*, *90*(6B), S1–S31, doi:10.1785/0120000512.

Graves, R., T. H. Jordan, S. Callaghan, E. Deelman, E. Field, G. Juve, C. Kesselman, P. Maechling, G. Mehta, K. Milner, D. Okaya, P. Small, K. Vahi (2010), CyberShake: A Physics-Based Seismic Hazard Model for Southern California, *Pure Appl. Geophys.*, *168*(3–4), 367–381, doi:10.1007/s00024-010-0161-6.

Graves, R. W., B. T. Aagaard, and K. W. Hudnut (2011), The ShakeOut earthquake source and ground motion simulations, *Earthq. Spectra*, *27*(2), 273–291, doi:10.1193/1.3570677.

Haskell, N. A. (1953), The dispersion of surface waves on multilayered media, *Bull. Seismol. Soc. Am.*, *43*(1), 17–34.

Haskell, N. A. (1960), Crustal Reflection of Plane SH Waves, *J. Geophys. Res.*, *65*(12), 4147–4150.

Herrmann, R. B. (2013), Computer Programs in Seismology: An Evolving Tool for Instruction and Research, *Seismol. Res. Lett.*, *84*(6), 1081–1088, doi:10.1785/0220110096.

Hruby, C. E., and I. A. Beresnev (2003), Empirical corrections for Basin effects in stochastic ground-motion prediction, based on the Los Angeles basin analysis, *Bull. Seismol. Soc. Am.*, *93*(4), 1679–1690, doi:10.1785/0120020121.

Joyner, W. B. (2000), Strong motion from surface waves in deep sedimentary basins, *Bull. Seismol. Soc. Am.*, *90*(6 SUPPL.), 95–112, doi:10.1785/0120000505.

Kawase, H. (2003), Site Effects on Strong Ground Motions. *International Handbook of Earthquake & Engineering Seismology*, 81, 1013.

Kawase, H., and K. Aki (1989), A study on the response of a soft basin for incident S, P, and Rayleigh waves with special reference to the long duration observed in Mexico City, *Bull. Seismol. Soc. Am.*, *79*(5), 1361–1382.

Kramer, S. L. (1996), *Geotechnical earthquake engineering*, Pearson Education India.

Kwok, A. O., and J. P. Stewart (2006), Evaluation of the effectiveness of theoretical 1D amplification factors for earthquake ground-motion prediction, *Bull. Seismol. Soc. Am.*, *96*(4 A), 1422–1436, doi:10.1785/0120040196.

Lee, E., P. Chen, T. H. Jordan, P. B. Maechling, M. a M. Denolle, and G. C. Beroza (2014), Full-3-D tomography for crustal structure in Southern California based on the scattering-integral and the adjoint-wavefield methods, *J. Geophys. Res. Solid Earth*, *119*, 6421–6451, doi:10.1002/2014JB011346.

Li, D., D. Helmberger, R. W. Clayton, and D. Sun (2014), Global synthetic seismograms using a 2-D finite-difference method, *Geophys. J. Int.*, *197*(2), 1166–1183, doi:10.1093/gji/ggu050.

Lin, F.-C., V. C. Tsai, and M. H. Ritzwoller (2012), The local amplification of surface waves: A new observable to constrain elastic velocities, density, and anelastic attenuation, *J. Geophys. Res.*, *117*(B6), B06302, doi:10.1029/2012JB009208.

Liu, H.-L., and T. Heaton (1984), Array analysis of the ground velocities and accelerations from the 1971 San Fernando, California, earthquake, *Bull. Seismol. Soc. Am.*, *74*(5), 1951–1968.

Mitchell, B. J. (1973), Surface-wave attenuation and crustal anelasticity in central north america, *Bull. Seismol. Soc. Am.*, *63*(3), 1057–1071.

Novikova, E. I., and M. D. Trifunac (1994), Duration of strong ground motion in terms of earthquake magnitude, epicentral distance, site conditions and site geometry, *Earthq. Eng. Struct. Dyn.*, *23*(November 1993), 1023–1043.

Olsen, K. B., and G. T. Schuster (1995), Causes of low-frequency ground motion amplification in the Salt Lake Basin: the case of the vertically incident P wave, *Geophys. J. Int.*, *122*(3), 1045–1061, doi:10.1111/j.1365-246X.1995.tb06854.x.

Pinnegar, C. R. (2006), Polarization analysis and polarization filtering of three-component signals with the time-frequency S transform, *Geophys. J. Int.*, *165*, 596–606, doi:10.1111/j.1365-246X.2006.02937.x.

Saikia, C. K., D. S. Dreger, and D. V Helmberger (1994), Modeling of Energy Amplification Recorded within Greater Los Angeles Using Irregular Structure, *Bull. Seism. Soc. Am.*, *84*(1), 47–61.

Sánchez-Sesma, F. J. (1987), Site effects on strong ground motion, *Soil Dyn. Earthq. Eng.*, *6*(2), 124–132.

Thompson, E. M., L. G. Baise, R. E. Kayen, and B. B. Guzina (2009), Impediments to predicting site response: Seismic property estimation and modeling

simplifications, *Bull. Seismol. Soc. Am.*, *99*(5), 2927–2949, doi:10.1785/0120080224.

Tromp, J., and F. A. Dahlen (1992), Variational principles for surface wave propagation on a laterally heterogeneous Earth-11. Frequency-domain JWKB theory, *Geophys. J. Int.*, *109*, 599–619.

U.S. Geological Survey and California Geological Survey (2006), Quaternary fault and fold database for the United States, from USGS web site: http//earthquakes.usgs.gov/regional/qfaults/

Wald, D. J., and T. I. Allen (2007), Topographic slope as a proxy for seismic site conditions and amplification, *Bull. Seismol. Soc. Am.*, *97*(5), 1379–1395, doi:10.1785/0120060267.

Wills, C. J., M. Petersen, W. A. Bryant, M. Reichle, G. J. Saucedo, S. Tan, G. Taylor, and J. Treiman (2000), A Site-Conditions Map for California Based on Geology and Shear-Wave Velocity, *Bull. Seismol. Soc. Am.*, *90*(6B), S187–S208.

Conclusion

This thesis explored several different applications possible through the observation of surface waves. Chapter 2 demonstrated the (now) relatively standard use of ambient noise cross correlation functions (NCFs) to build a 3D velocity model offshore southern California, though some additional signal processing techniques were needed given the use of both on-land and ocean-bottom seismometers. That work relied purely on travel-time measurements, and so any amount of signal processing was allowed to strengthen signal-to-noise in the NCFs. The resulting velocity model was used to better understand the tectonic and geologic history of the Continental Borderland region offshore southern California.

Chapters 3 and 4 described the application of a wavefront tracking technique to recover site amplification, attenuation and sources or scattering, using ambient noise on two very different scales. The dense Long Beach Array in southern California yielded observations in the range 0.67 to 2 Hz, while the USArray yielded observations between 8 and 32 second periods. The wavefront tracking technique, combined with rigorous signal processing to preserve relative amplitudes, was able to circumvent a longstanding issue with ambient noise amplitudes; because the method only measures changes to a wavefront as it passes over an array, the initial strength and direction of ambient noise is no longer important.

Chapter 5 explored the interpretation of surface-wave amplification as it relates to seismic hazard. It was pointed out that should surface-waves contribute to the strong shaking relevant for the design of buildings and infrastructure, a different definition of site response should be considered than what is currently used in engineering practice. This new definition for surface waves relies purely on 1D velocity and density profiles, and arguments of conservation of energy to estimate the relative change in amplitude. The fact that the theory uses only 1D profiles may be seen as a limitation and simplification of otherwise complex 3D wave phenomena, but in fact we believe it is a strength that it can be easily adapted in the

current earthquake-engineering workflows that also rely on purely 1D models. The fact that 1D models alone can explain significant features and differences in observed amplification indicates an opportunity to improve future seismic hazard estimates, especially in deeper sedimentary basins.

Supplementary Materials

S1: Supplement for Chapter 2

This material was also originally published as a supplement for the same paper as Chapter 2:

Bowden, D. C., Kohler, M. D., Tsai, V. C., & Weeraratne, D. S. (2016). Offshore Southern California lithospheric velocity structure from noise cross-correlation functions. *Journal of Geophysical Research: Solid Earth. https://doi.org/10.1002/*2016JB012919

Figs. S1.1-S1.3 show raypaths and resulting 2D inversions at different periods: 12 s, 20 s and 40 s respectively, similar to what is shown in Figs. 2.6 and 2.7 in the main text. Text S1.1 describes two additional tests for model recovery and resolution. Data used for the tests is entirely synthetic, but raypaths used and the range of expected values are designed to closely match the actual experiment. Fig. S1.4 goes with Text S1, showing one of the synthetic models used. Finally, Fig. S1.5 shows the range of input starting models used and 3 examples of 1D depth profiles, with error bars indicating variability caused by choice of starting model.

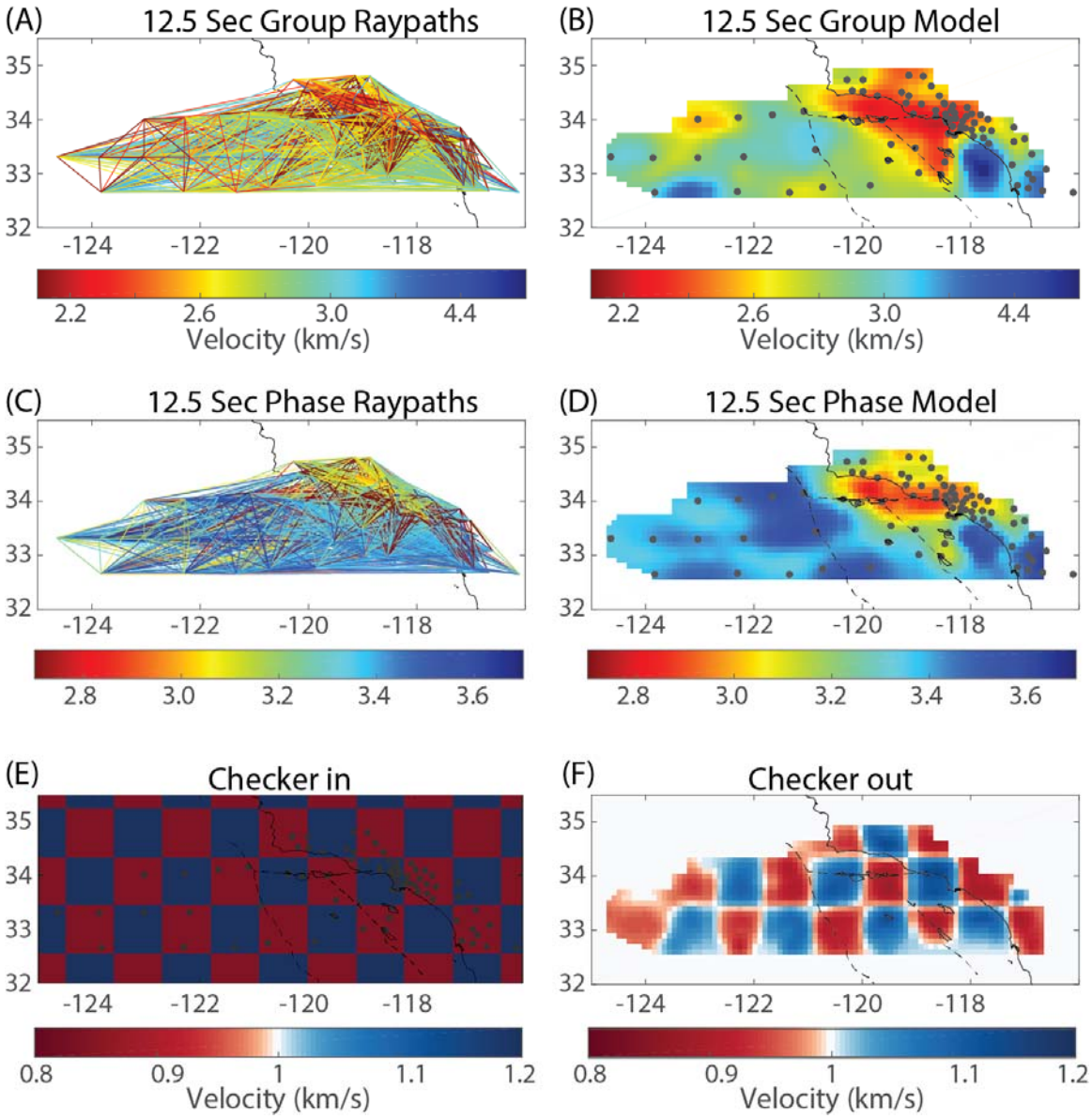

Figure S1.1: Similar to Figure 2.6 in the main text, but at 12.5 second periods. Input rays for group velocity (A) is inverted onto a regular 2D grid, (B). Similarly, input rays for phase velocity (C) is inverted onto (D). Panel (E) depicts a checkerboard input test and (F) the recovered model.

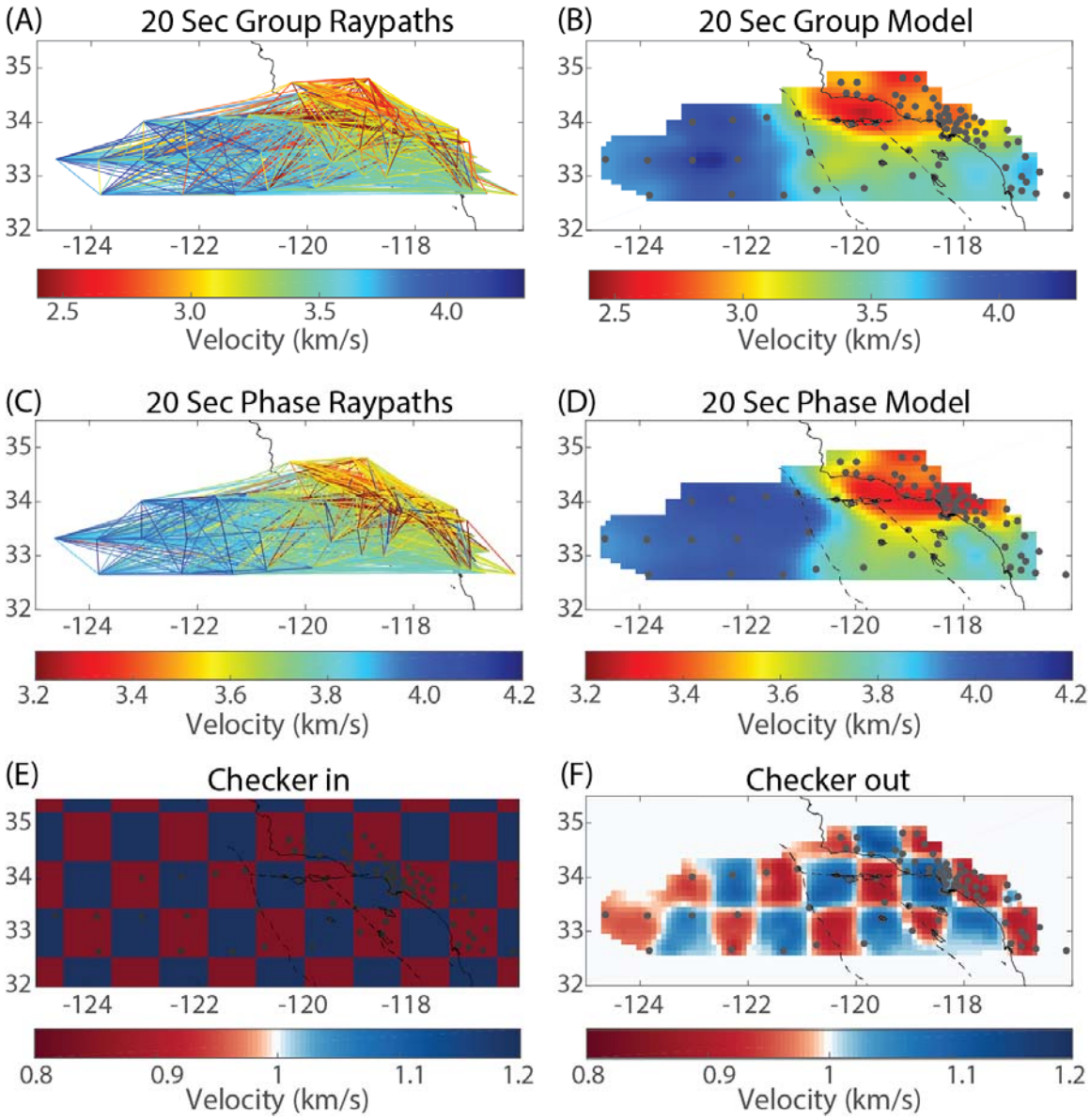

Figure S1.2: Similar to Figure 2.6 in the main text, but at 20 second periods. Input rays for group velocity (A) is inverted onto a regular 2D grid, (B). Similarly, input rays for phase velocity (C) is inverted onto (D). Panel (E) depicts a checkerboard input test and (F) the recovered model.

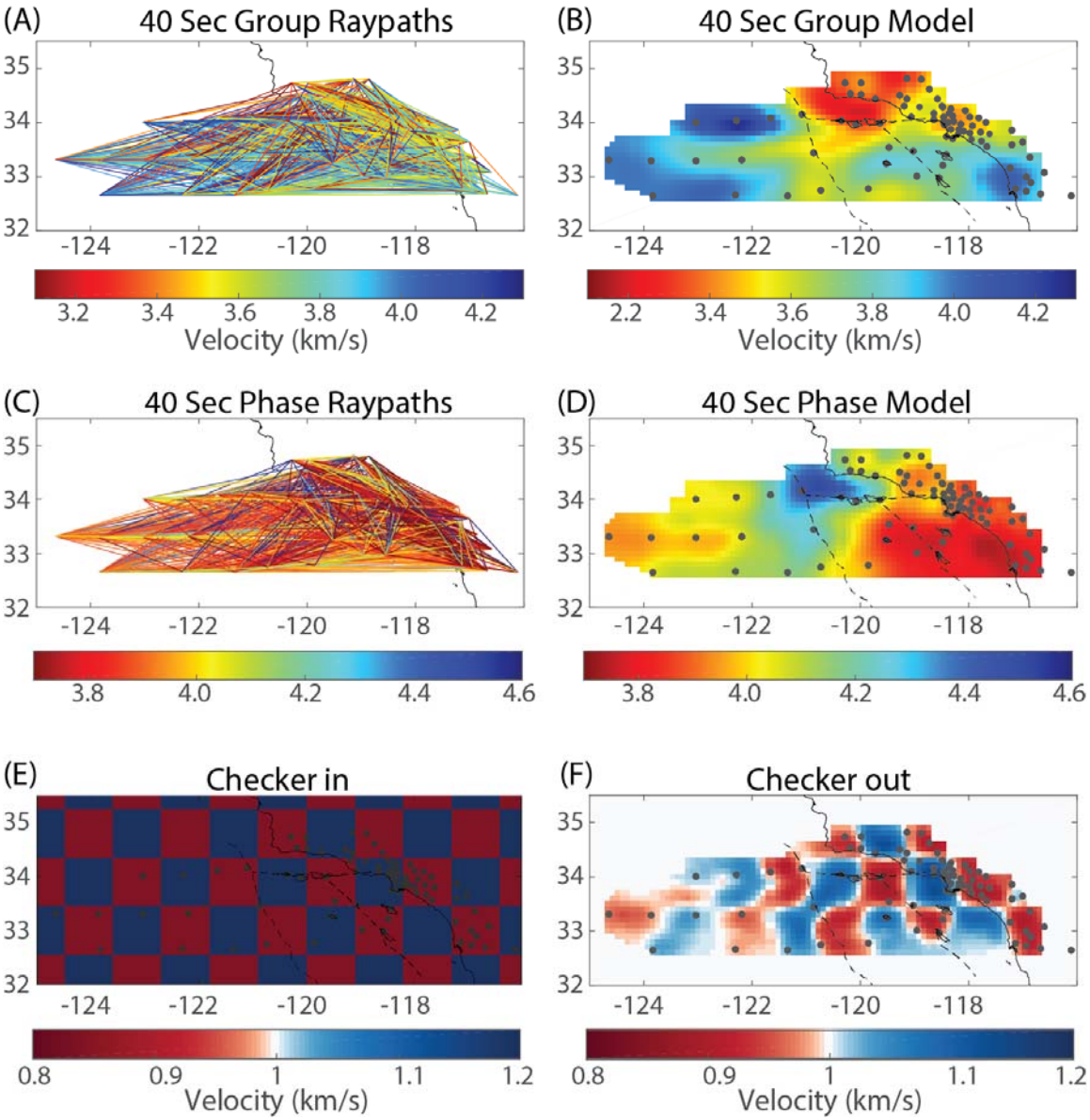

Figure S1.3: Similar to Figure 2.6 in the main text, but at 40 second periods. Input rays for group velocity (A) is inverted onto a regular 2D grid, (B). Similarly, input rays for phase velocity (C) is inverted onto (D). Panel (E) depicts a checkerboard input test and (F) the recovered model.

Two additional tests were performed to assess model inversion reliability. The first is similar to a standard checkerboard test, but with the only input feature being a sharp boundary at the Patton Escarpment with fast velocities to the west and slow velocities to the east, as shown

in Fig. S1.4a. The raypaths corresponding to 8.5 s period are inverted with the same regularization and processing for a new 2D model, presented in Fig. S1.4b. The recovered model matches the location of the Patton Escarpment well, with minimal loss of amplitudes immediately adjacent on either side.

The second test demonstrates the improvement of our 3D model over a relatively simple starting model, also aimed at testing the strong bathymetric boundary of the Patton Escarpment. The starting model includes a 1D profile based on an oceanic PREM [*Dziewonski and Anderson,* 1981] west of the Patton Escarpment, and a southern California averaged model [*Kohler et al.,* 2003] in the Borderland and on-land, with a smoothed transition between the two, and all grid points using an appropriate water depth. This synthetic model approximates the entire continental shelf and transition to oceanic abyssal plain in a way that accounts for the absence of a more complete model. This simple model predicts dispersion curves with an average absolute value of misfit of 0.37 km/s compared to our measured dispersion data, while our final inverted model fits the data twice as well with an average misfit of only 0.17 km/s.

The steep change in bathymetry and structure undoubtedly affected the ability to measure clean noise correlation functions (NCFs); reflections or other spurious signals in the NCFs which cross the boundary or coastline made it difficult for an automated program to pick dispersion data, requiring judicious manual review. However, we are confident that any other effects of the sharp bathymetric boundary on the inversion itself are minimal.

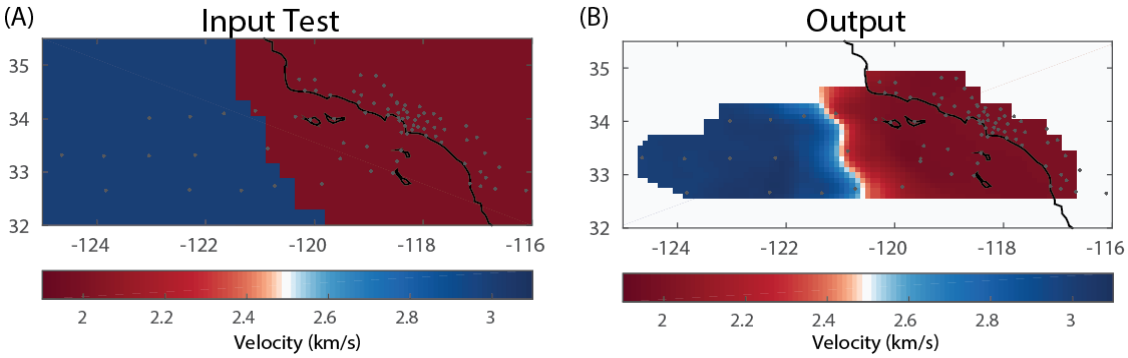

Figure S1.4: The input checkerboard (A) for the first test, designed to test recovery specifically along the Patton Escarpment, and the recovered model (B).

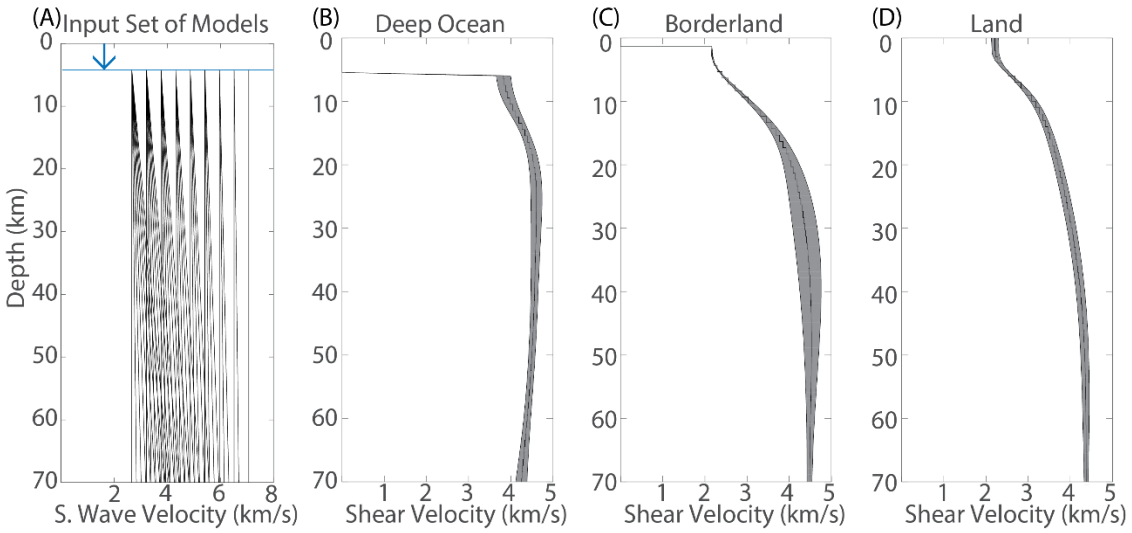

Figure S1.5: Panel (A) shows the range of starting models used for 1-D depth inversions. The only variable at each location is a fixed water depth prescribed by bathymetry at each grid point. Panels B-D are representative 1D profiles from the three primary tectonic regions, with error bars representing the variability from choice of starting model. Shaded grey regions indicate 1 standard deviation of variability from the range of input models, and the fact that all standard deviations are fairly small indicates we have converged to a fairly robust model at all depths.

S2: On the Wavefront Tracking Used in Chapters 3 and 4

Chapters 3 and 4 rely on the wavefront tracking approach outlined by *Lin et al.* [2012]. However, neither chapter fully explains the derivation of the equation used, and even in the original work by *Lin et al.* [2012] steps are abbreviated. A full derivation is presented here.

Tanimoto [1990] and *Tromp and Dahlen* [1992] describe that surface waves can be approximated by a 2D potential, χ_{2D}, as a function of space on the surface of the earth, *r*, and time, *t*:

$$\chi_{2D}(r,t) = \frac{A(r)}{\beta(r)} e^{i\omega(t-\tau(r))} \quad S2.1$$

where $A(r)$ and $\tau(r)$ describes the wave's observed amplitude and travel time, respectively, and $\beta(r)$ describes a local site amplification factor. This surface-wave potential satisfies the homogeneous damped wave equation:

$$\frac{\partial^2 \chi_{2D}(r,t)}{\partial t^2} = -2\gamma(r)\frac{\partial \chi_{2D}(r,t)}{\partial t} + c(r)^2 \nabla^2 \chi_{2D}(r,t) \quad S2.2$$

where $c(r)$ is local phase velocity and $\gamma(r)$ is a damping constant that can be related to the local seismic quality factor, Q, through:

$$\gamma = \frac{ck}{2UQ} \quad S2.3$$

where c is the surface-wave phase velocity, k is wavenumber and U is group velocity, following *Ben-Menahem and Singh* [1981] and *Tromp and Dahlen* [1992]. This can instead also be written in terms of a local attenuation factor, α(r), to match *Prieto et al.* [2009] and *Lin et al.* [2012]:

$$\gamma = \frac{c\pi f}{UQ} = c\alpha \quad S2.4$$

Eq. S2 becomes the following, which matches Equation 1 of *Lin et al.* [2012] :

$$\frac{1}{c(r)^2}\frac{\partial^2 \chi_{2D}(r,t)}{\partial t^2} = \frac{-2\alpha(r)}{c(r)}\frac{\partial \chi_{2D}(r,t)}{\partial t} + \nabla^2 \chi_{2D}(r,t) \quad S2.5$$

From here, the 2D potential in Eq. S1 is substituted into Eq. S5:

$$\frac{1}{c(r)^2}\frac{\partial^2}{\partial t^2}\left(\frac{A(r)}{\beta(r)}e^{i\omega(t-\tau(r))}\right) \qquad S2.6$$
$$= \frac{-2\alpha(r)}{c(r)}\frac{\partial}{\partial t}\left(\frac{A(r)}{\beta(r)}e^{i\omega(t-\tau(r))}\right) + \nabla^2\left(\frac{A(r)}{\beta(r)}e^{i\omega(t-\tau(r))}\right)$$

$$\frac{1}{c(r)^2}\frac{A(r)}{\beta(r)}(i\omega)^2 e^{i\omega(t-\tau(r))}$$
$$= \frac{-2\alpha(r)}{c(r)}\frac{A(r)}{\beta(r)}i\omega\, e^{i\omega(t-\tau(r))} \qquad S2.7$$
$$+ \nabla\left(\nabla\left(\frac{A(r)}{\beta(r)}\right)e^{i\omega(t-\tau(r))} - \frac{A(r)}{\beta(r)}i\omega\nabla\tau(r)e^{i\omega(t-\tau(r))}\right)$$

$$\frac{1}{c(r)^2}\frac{A(r)}{\beta(r)}(i\omega)^2 e^{i\omega(t-\tau(r))}$$
$$= \frac{-2\alpha(r)}{c(r)}\frac{A(r)}{\beta(r)}i\omega\, e^{i\omega(t-\tau(r))} + \nabla^2\left(\frac{A(r)}{\beta(r)}\right)e^{i\omega(t-\tau(r))} \qquad S2.8$$
$$- \nabla\left(\frac{A(r)}{\beta(r)}\right)i\omega\nabla\tau(r)\, e^{i\omega(t-\tau(r))} - \nabla\left(\frac{A(r)}{\beta(r)}\right)i\omega\nabla\tau(r)\, e^{i\omega(t-\tau(r))}$$
$$- \frac{A(r)}{\beta(r)}i\omega\nabla^2\tau(r)e^{i\omega(t-\tau(r))} + \frac{A(r)}{\beta(r)}(i\omega)^2\nabla\tau(r)\cdot\nabla\tau(r)e^{i\omega(t-\tau(r))}$$

The exponential drops from all terms and we can treat the real and imaginary components separately. At this point, also, the spatial dependence is omitted for brevity. The real parts are:

$$\frac{-1}{c^2}\frac{A}{\beta}\omega^2 = \nabla^2(A/\beta) - A/\beta\,\omega^2\nabla\tau\cdot\nabla\tau \qquad S2.9$$

$$\frac{1}{c^2} = -\frac{\nabla^2(A/\beta)}{\omega^2(A/\beta)} + \nabla\tau\cdot\nabla\tau \qquad S2.10$$

which is often referred to as the full Helmholtz equation, which reduces to an Eikonal equation in the high-frequency limit ($\omega \gg 1$). The imaginary components of Eq S8 lead to what is often referred to as a transport equation:

$$\frac{2\alpha}{c}\frac{A}{\beta}\omega = 2\nabla(A/\beta)\cdot\nabla\tau\;\omega - \;A/\beta\;\nabla^2\tau\;\omega \qquad S2.11$$

$$\frac{2\alpha}{c} = \frac{2\nabla(A/\beta)\cdot\nabla\tau}{A/\beta} - \;\nabla^2\tau \qquad S2.12$$

$$\frac{2\alpha}{c} = -\frac{2\nabla \mathrm{A}\cdot\nabla\tau}{A} + \;\frac{2\nabla\beta\cdot\nabla\tau}{\beta} - \;\nabla^2\tau \qquad S2.13$$

Re-arranging gives the same form of the equation used in *Lin et al.* [2012], where the right-hand side contains only observables of the wavefield (A, τ):

$$\frac{2\nabla\beta\cdot\nabla\tau}{\beta} - \frac{2\alpha}{c} = \frac{2\nabla \mathrm{A}\cdot\nabla\tau}{A} + \nabla^2\tau \qquad S2.14$$

The only remaining difference between Eq. S14 and what is used in Chapters 3 and 4 is the presence of a sources term, *S(r)*, on the left hand side, which is required since ambient noise sources or scattered noise energy within the array may change wavefront's amplitude as it propagates. This source description was not needed for the work of *Lin et al.* [2012] because a single earthquake source was used for each observation.

Ben-Menahem, A., and S. J. Singh (1981), *Seismic waves and sources*, Springer Science & Business Media.

Lin, F.-C., V. C. Tsai, and M. H. Ritzwoller (2012), The local amplification of surface waves: A new observable to constrain elastic velocities, density, and anelastic attenuation, *J. Geophys. Res.*, 117(B6), B06302, doi:10.1029/2012JB009208.

Prieto, G. a., J. F. Lawrence, and G. C. Beroza (2009), Anelastic Earth structure from the coherency of the ambient seismic field, *J. Geophys. Res.*, 114(B7), B07303, doi:10.1029/2008JB006067.

Tanimoto, T. (1990), Modelling curved surface wave paths: membrane surface wave synthetics, *Geophys. J. Int.*, 103, 89–100.

Tromp, J., and F. A. Dahlen (1992), Variational principles for surface wave propagation on a laterally heterogeneous Earth-11. Frequency-domain JWKB theory, *Geophys. J. Int.*, 109, 599–619.

S3: On the Difference Between Causal and Acausal Ambient Noise Signals

Chapters 3 and 4 distinguish between attenuation and noise sources or scatterers by exploiting a difference between causal and acausal signals from noise cross-correlations. This is also referred to as the outgoing and incoming wavefield, respectively, when cross-correlations are collected using a single station as a virtual source. This is explained briefly in both chapters, but a more complete explanation with illustrations is provided here.

Chapters 3 and 4, as well as the previous supplement S2, described that an additional source term, *S(r)*, should be introduced to the wavefront tracking approach when ambient noise is used. This term may refer to new sources of ambient noise energy within the array, or to small heterogeneities that act as scatterers to redistribute waves propagating from other directions. As the entire technique assumes purely a single mode of 2D surface waves, the scattering referred to here does not account for any energy radiated away in the form of P or S converted phases. Between new ambient noise sources or scattered energy, the two possibilities cannot be distinguished from this method alone, though in Chapter 3 the measurements are interpreted as scatterers since the spatial distribution correlates with geologic contrasts, and because new sources of noise energy are not expected at these frequencies in the region.

A potential issue lies in that both attenuation and these source/scatterer contributions will act to lower or raise the amplitudes of a seismic wave as it passes, regardless of direction of propagation, making it difficult to distinguish between the two. Fortunately, there is a difference between the source regions which may contribute to the ambient noise cross correlation. The causal, positive-lag, outgoing wavefield is sensitive to sources only on the virtual-source side of the two stations. Figure S3.1 shows one station used a virtual source and an example of two other adjacent stations in the array, with hyperboles roughly indicating the region for which ambient noise sources will most strongly contribute to surface wave observations. In the case of causal, outgoing signals the two source contribution regions are roughly identical, so it is assumed that energy new from noise sources or scatterers will be

consistent for both measurements; any change in amplitude is associated with attenuation only. For the acausal, negative lag, incoming wavefield the source regions move along with the propagating wave. In this case, new energy from sources or scatterers will be collected as the wavefront passes.

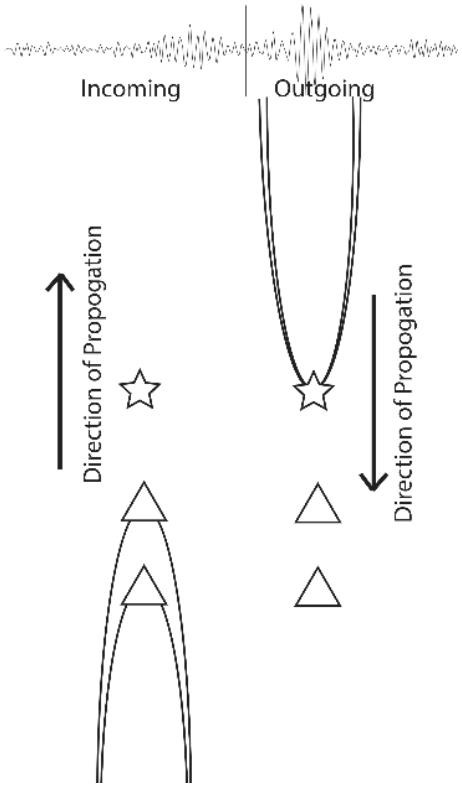

Figure S3.1: Illustration of source regions contributing to incoming (left) and outgoing (right) wavefronts. The star indicates the virtual source and triangles indicate two other stations in the array. Only the incoming wavefront will catch new or scattered energy as the wavefront propagates.

It is explained Chapters 3 and 4 that the incoming and outgoing wavefields are treated independently for precisely this reason. It is also explained that the observations of a wavefront's corrected amplitude are fit using a 1-psi curve (a sine curve with one period in 360 degrees, with variable phase and a variable static offset). Again, the amplitude and phase of the sinusoid are associated with the term $(2\nabla\beta \cdot \nabla\tau)/\beta$, while the static offset of the mean

is associated with the terms $(S - 2\alpha/c)$. Figure 3.2 indicates how the incoming and outgoing measurements are interpreted: the outgoing measurements have signals consistently decreased according to attenuation while the incoming measurments may be both increased and decreased by either effect. In this illustration, attenuation acts to increase the signals amplitude because we consider the incoming wave to be propagating backwards, or in a reverse time sense, though a different sign convention may be chosen.

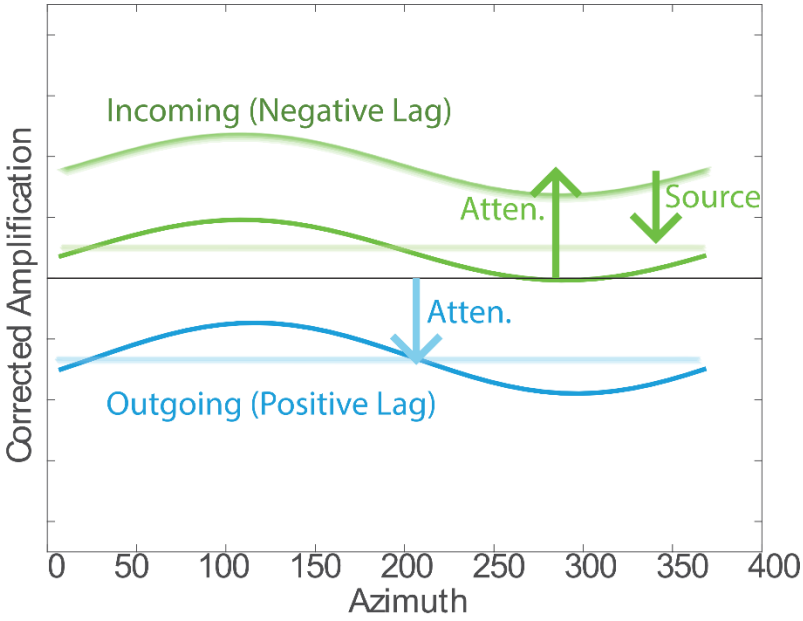

Figure S3.2: Interpretation of the 1-Psi sinusoids fit from Corrected Amplification observations (RHS of Eq. 3.1 and 4.2).

S4: Supplement for Chapter 4

This material was also originally published as a supplement for the same paper as Chapter 4:

Bowden, D. C., Tsai, V. C., & Lin, F.-C. (2017). Amplification and Attenuation across USArray using Ambient Noise Wavefront Tracking. *Journal of Geophysical Research: Solid Earth*, (2012), 1–16. https://doi.org/10.1002/2017JB014804

Figure S4.1 shows the mean chi-squared misfit (also referred to as an average weighted least-squares misfit) of the 1-psi curve-fitting procedure applied to corrected amplification observations at each of 18 different azimuthal bins. Specifically, for d_i representing the mean of a given 20-degree bin, $g_i(m)$ representing the predicted fit of the 1-psi sinusoid and σ representing the standard deviation of that bin's observations:

$$misfit = \sum_{i=1}^{18} \left(\frac{d_i - g_i(m)}{\sigma} \right)^2 \Big/ 18 \qquad S4.1$$

Places where this misfit was larger than 0.1 are discarded before performing a final fit for amplification or attenuation. The higher misfits around the edges of the array, where azimuthal coverage was sparse, are higher, which is why the edges of the array are trimmed in most figures of the main text.

As discussed in the main article, the observed amplification from Eq. 4.2, β, depends on phase velocity, group velocity and an integral over eigenfunctions $\boldsymbol{I_0}$. The phase velocity term is important because the wavefront tracking approach accounts for a shift in wavelength in addition to wavefront focusing and defocusing, and is required for the surface wave potential to satisfy the wave equation. This will not be observed, however, in a direct amplitude comparison such as in the work of Eddy and Ekstrom [2014], or when predicting amplification based on 1D profiles for hazard purposes (i.e., Bowden and Tsai [2017]). In the main text, Eq. 4.3 defines a site-amplification ratio more appropriate for these cases. Figure S4.1 corrects our observed amplification (β) for phase velocity, to match Eq. 4.3 and is more appropriate for direct amplitude observations. Specifically, we calculate $A_n/A_n^R =$

$\beta\sqrt{c/c_R}$, where phase velocity c is estimated from $1/\nabla\tau$ in the wavefront tracking observations.

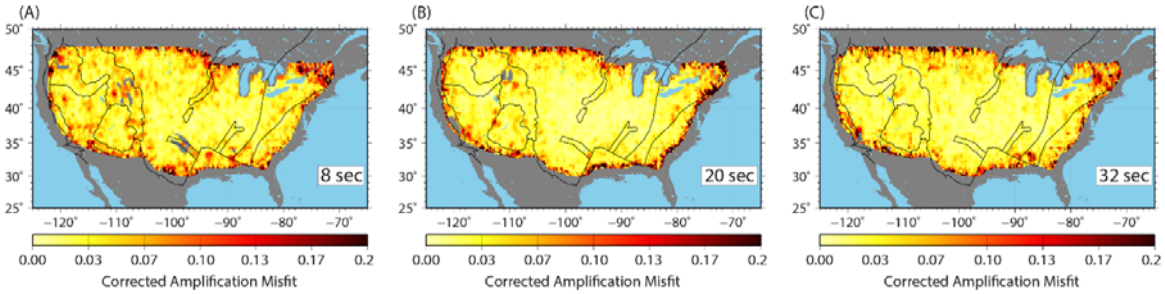

Figure S4.1: Mean chi-squared misfit of the 1-psi curve fitting applied to corrected amplifications at 18 different azimuthal bins at 8, 20 and 32 seconds (A-C).

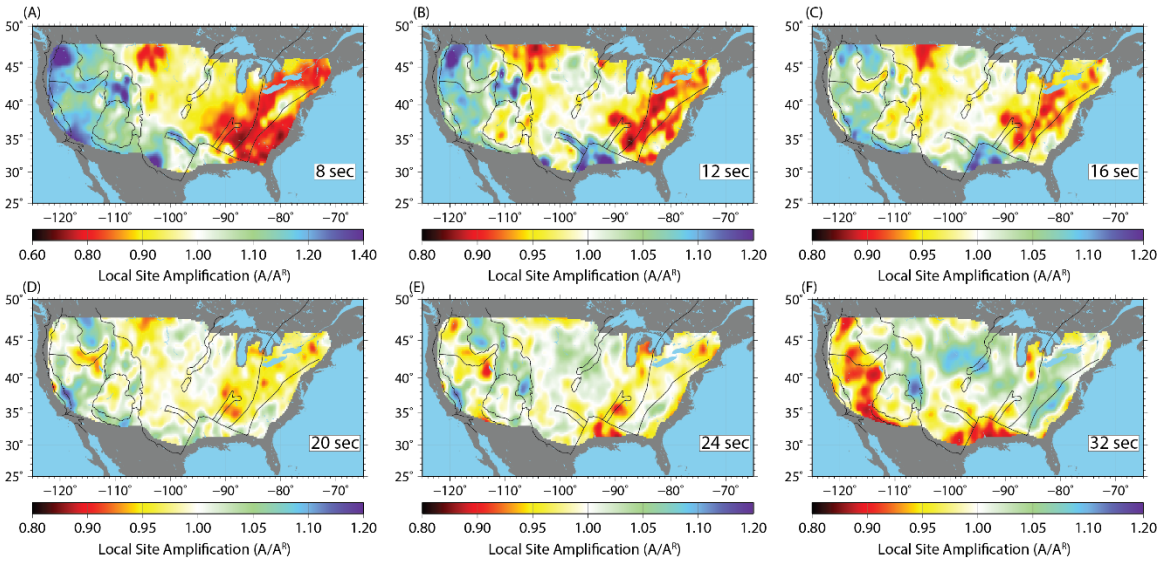

Figure S4.2: Amplification measurements, corrected for phase velocity, at a range of periods: 8, 12, 16, 20, 24 and 32 seconds (A-F). This is to provide amplitude ratios ($\boldsymbol{A_n/A_n{}^R}$ from Eq. 4.3) more appropriate for direct observations of amplitudes. We note that all maps are plotted with a non-linear colorscale to emphasize differences closer to 1. Only the 8-second subpanel (A) is plotted with a different scale than the others.

S5: Supplement for Chapter 5

This material was also originally published as a supplement for the same paper as Chapter 5:

Bowden, D. C., & Tsai, V. C. (2017). Earthquake ground motion amplification for surface waves. *Geophys. Res. Lett.*, *43*, 1–8. https://doi.org/10.1002/2016GL071885

We show here an alternative to the layer-over-halfspace model used in Fig. 5.1 of the main text, using the "very-hard rock site" from (Boore & Joyner, 1997). The reference model is perturbed to resemble a sedimentary layer by subtracting 1,000 m/s at depths shallower than 100m.

Compared to Fig. 5.1 of the main text, the frequencies of peak amplification occur uniformly higher because of the shallower basin, and the amplification is uniformly stronger because of the stronger impedance contrast. However, the general shape and relation between the curves is quite consistent. For example, the peak frequency of Rayleigh-wave amplification is roughly twice that of the vertically-incident shear-wave fundamental resonance for both cases. Also, because Love waves can exist in the reference profile (they do not exist in a halfspace), a Love wave amplification curve can now be added to the description.

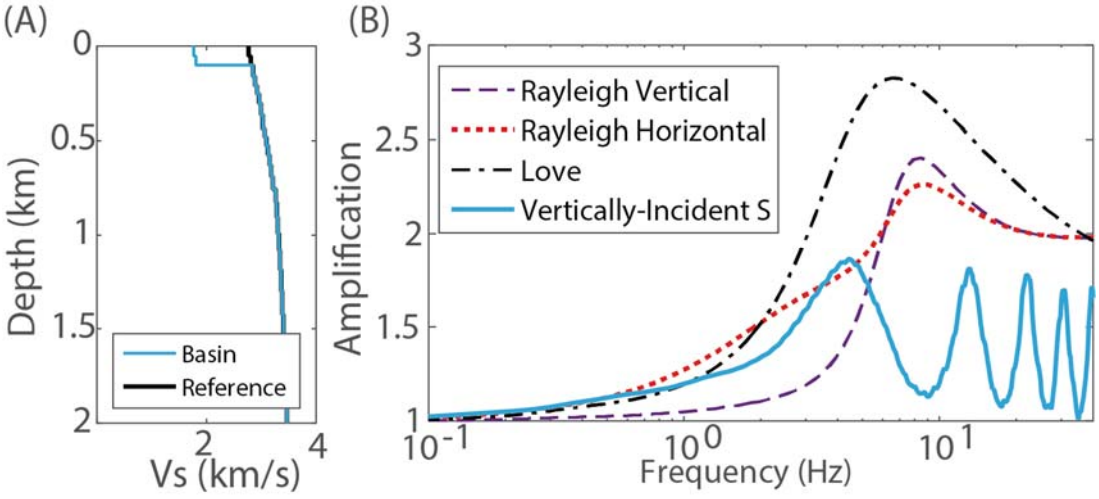

Figure S5.1: (A) Profiles for the Boore and Joyner (1997) very-hard rock site used as reference (black) and a basin profile (blue) with perturbation at 100m depth. (B) The resulting transfer functions for each wave type.